

Physics and Dynamics of Current Sheets in
Pulsed Plasma Thrusters

FINAL REPORT
to the US Air Force Office of Scientific Research

GRANT NUMBER: F49620-01-1-0052

Start date:08/01/00

End date:10/31/01

PI: Prof. Edgar Choueiri

Graduate Students: Thomas Markusic, John Berkery
and James Cooley

Electric Propulsion and Plasma Dynamics Lab (EPPDyL)
Applied Physics Group

MAE Dept., Princeton University

Princeton NJ 08544

Phone: (609) 258 5220 Fax: (609) 258 6875

E-mail: choueiri@princeton.edu

REPORT DOCUMENTATION PAGE			Form Approved OMB No. 074-0188	
Public reporting burden for this collection of information is estimated to average 1 hour per response, including the time for reviewing instructions, searching existing data sources, gathering and maintaining the data needed, and completing and reviewing this collection of information. Send comments regarding this burden estimate or any other aspect of this collection of information, including suggestions for reducing this burden to Washington Headquarters Services, Directorate for Information Operations and Reports, 1215 Jefferson Davis Highway, Suite 1204, Arlington, VA 22202-4302, and to the Office of Management and Budget, Paperwork Reduction Project (0704-0188), Washington, DC 20503				
1. AGENCY USE ONLY (Leave blank)		2. REPORT DATE August 6, 2002		3. REPORT TYPE AND DATES COVERED Final Technical Report 08/01/00 to 10/31/01
4. TITLE AND SUBTITLE Physics and Dynamics of Current Sheets in Pulsed Plasma Thrusters			5. FUNDING NUMBERS AFOSR Grant #F49620-01-1-0052	
6. AUTHOR(S) Professor Edgar Choueiri				
7. PERFORMING ORGANIZATION NAME(S) AND ADDRESS(ES) Princeton University Dept. Mechanical & Aerospace Engrg. Olden St. Princeton, NJ 08544			8. PERFORMING ORGANIZATION REPORT NUMBER	
9. SPONSORING / MONITORING AGENCY NAME(S) AND ADDRESS(ES) AFOSR/NA 801 North Randolph St. Room 732 Arlington, VA 22203-1977			10. SPONSORING / MONITORING AGENCY REPORT NUMBER	
11. SUPPLEMENTARY NOTES				
12a. DISTRIBUTION / AVAILABILITY STATEMENT Approved for public release; distribution is unlimited.			12b. DISTRIBUTION CODE	
13. ABSTRACT (<i>Maximum 200 Words</i>) In this final report we present the results of our AFOSR-sponsored studies of the physics and dynamics of current sheets in electromagnetic, pulsed, plasma thrusters (PPTs). The research project focused on the fundamental aspects of the physics and dynamics that are most relevant to improving the performance of PPTs. In particular, we focused on the problems of current sheet canting and current sheet initiation, both of which can lead to adverse effects on the mass utilization and propulsive efficiencies of PPTs operating in the electromagnetic mode.				
14. SUBJECT TERMS Pulsed Plasma Thrusters			15. NUMBER OF PAGES 101	
			16. PRICE CODE	
17. SECURITY CLASSIFICATION OF REPORT Unclassified	18. SECURITY CLASSIFICATION OF THIS PAGE Unclassified	19. SECURITY CLASSIFICATION OF ABSTRACT Unclassified	20. LIMITATION OF ABSTRACT UL	

Contents

1	Current Sheet Canting	4
1.1	Introduction	4
1.1.1	The pulsed plasma thruster	5
1.1.2	History of the Pulsed Plasma Thruster	5
1.1.3	Definition of the Problem	7
1.1.4	Importance of the Problem	7
1.2	Review of the Problem	9
1.3	Experimental Apparatus	10
1.3.1	General experimental layout	10
1.3.2	Accelerator	10
1.3.3	Pulse forming networks	12
1.3.4	Vacuum facility	14
1.3.5	Data Acquisition Equipment and Noise Suppression	15
1.4	Diagnostics	15
1.5	Circuit current measurement	16
1.6	Voltage measurement	16
1.6.1	High-speed photography	17
1.6.2	Schlieren imaging	18
1.6.3	Magnetic field probes	21
1.6.4	Laser interferometry	22
1.6.5	Emission spectroscopy	26
1.7	Experimental Results	29
1.8	Circuit Current and Voltage Measurements	29
1.8.1	Circuit Current	29
1.8.2	Terminal voltage measurements	32
1.9	High-speed photography	34
1.9.1	Evolution of the discharge	35
1.9.2	Speed and canting-angle measurements	38
1.9.3	Discussion	39
1.10	Schlieren imaging	40
1.10.1	Schlieren photography configuration	40
1.10.2	Shadowgraph configuration	40
1.10.3	Modified shadowgraph configurations	40
1.10.4	Discussion	41

1.11	Magnetic field probes	42
1.11.1	Database of canting angles	42
1.11.2	Evolution of the canting angle	43
1.11.3	Discussion	44
1.12	Laser interferometry	47
1.12.1	Discussion	49
1.13	Emission spectroscopy	50
1.13.1	Survey of spectral lines	50
1.13.2	Time-resolved spectra and temperature determination	51
1.14	Summary of experimental results	52
1.15	Analysis and Modelling	53
1.15.1	Further analysis of the experimental data	54
1.15.2	Modelling	56
1.15.3	Correlations with earlier research	74
1.15.4	Concluding remarks on the analysis	75
1.16	Conclusions	77
1.16.1	Summary of findings	77
1.16.2	Directions for Future Work	78
2	Current Sheet Photo-Initiation	80
2.1	Introduction	80
2.2	Experimental Setup	81
2.3	Experimental Methods and Results	82
2.3.1	Effect of Outgassing on Laser Pulse Energy Requirement	82
2.3.2	Mass Spectrometry	83
2.4	Theory	84
2.4.1	Discharge Initiation Mechanisms	84
2.4.2	Effects of Laser Radiation on the Surface	85
2.5	Discussion	91
2.6	Conclusions	92
3	How to build a Better Thruster	93
3.1	Insight from the current sheet canting study	93
3.2	Insight from the photo-initiation study	94

SYNOPSIS

In this final report we present the results of our AFOSR-sponsored studies of the physics and dynamics of current sheets in electromagnetic pulsed plasma thrusters (PPTs). The research project focused on the fundamental aspects of the physics and dynamics that are most relevant to improving the performance of PPTs. In particular we focused on the problems of current sheet canting and current sheet initiation, both of which can lead to adverse effects on the mass utilization and propulsive efficiencies of PPTs operating in the electromagnetic mode.

In Chapter 1 we report the final results of our extensive experimental and theoretical study on current sheet canting. The phenomenon of current sheet canting in pulsed electromagnetic accelerators is the departure of the plasma sheet that carries the current from a plane that is perpendicular to the electrodes to one that is skewed, or tipped. Current sheet canting is a ubiquitous problem in electromagnetic PPTs and results in a degradation of their propulsive efficiency. An experimental study in which photographic, magnetic, and laser-interferometric measurements of the canting angle of the current sheet in an experimental accelerator were made. The goal was to identify the mechanism(s) underlying the effect. The results of the experiments using advanced diagnostics and eight different propellants (hydrogen, deuterium, helium, neon, argon, krypton, xenon, and methane) were combined with a theoretical model and led to a detailed explanation of current sheet canting. In the resulting picture, canting is due to a depletion of plasma near the anode, which results from axial density gradient induced diamagnetic drift. Rapid penetration of the magnetic field through this region ensues, due to Hall effect, leading to a canted current front ahead of the initial current conduction channel. The acquired fundamental understanding allowed the development of design prescriptions to reduce canting and abate its detrimental effects. These are discussed in the final chapter.

In Chapter 2 we report on the recent results from our exploration of current sheet initiation in PPTs. In particular we explore the physics of photo-induced and surface-assisted discharge initiation which holds the promise for providing azimuthally uniform and erosion-free discharge initiation in PPTs.

Specifically we demonstrate that a discharge can be initiated in a PPT at an undervoltage by shining an IR laser pulse on the thruster's backplate. The technique has the potential for achieving uniform and erosion-free discharge initiation. Three candidate mechanisms are investigated: thermionic emission, cathode vaporization, and gas desorption. Mass spectroscopic measurements and theoretical calculations implicate water desorption from the backplate as the likely explanation for the observed effects. It is then shown that while thermionic emission was not operative in the experiments, it can be used as the basis of the design of a discharge initiator.

We finally conclude in Chapter 3 with a discussion of how the insight gained from our fundamental study can be used to design better thrusters.

Chapter 1

Current Sheet Canting

1

1.1 Introduction

Pulsed electromagnetic accelerators are devices which use intense bursts of electrical current ($\mathcal{O}(10^4 - 10^6)$ A) to create high speed ($\mathcal{O}(10^3 - 10^5)$ m/s) jets of plasma. They find application as plasma sources in many basic plasma science experiments[2] as well as in a specific genre of electric space propulsion device called the pulsed plasma thruster (PPT)[3]. The present work is motivated by the desire to improve the performance of pulsed electromagnetic accelerators in the context of plasma propulsion.

Understanding the performance of PPTs requires a detailed knowledge of the physics of the current conduction channel (the so-called current sheet) within the gas. When one begins to study the physics of current sheets, it becomes readily apparent that there are a multitude of interesting physical phenomena at play. Since current sheets are transient, inherently unstable structures, any rigorous theoretical treatment of current sheet physics would involve a complete, time-dependent, magnetoplasmadynamic model coupled with sheath and electrical circuit models. Similarly, experimental measurements of current sheet properties requires the use of specialized instruments capable of resolving rapidly evolving plasma structures. With these realities in mind, attempting to completely understand the physics of current sheets in a single study appears to be a rather daunting task. Rather than seeking a paragon, a more manageable approach is to develop simplified theoretical models and specialized experimental tools which expose a particular facet of current sheet behavior, and later assemble a more panoramic view of the overall physics through a succession of studies. This is the spirit of the present work, which focuses on understanding the spatial configuration of the current sheet in an experimental accelerator (the accelerator used was of the *gas-fed* variety, where electromagnetic acceleration

¹The material in this chapter is from the recent PhD thesis of T.E. Markusic[1].

is the dominant mode of acceleration; the results of this study may not be directly relevant to the *ablative* thrusters, where electrothermal acceleration may be significant[4]). More specifically, experimental measurements were obtained which show that current sheets tilt (or cant) relative to the electrodes as they propagate. The degree of canting was measured under a variety of experimental conditions and theoretical models were employed to explain the observed behavior. The sections which follow more completely define the background, scope, and general relevance of this study.

1.1.1 The pulsed plasma thruster

The motivation of this study is to gain a better understanding of the acceleration mechanism in pulsed plasma thrusters. Let us first, then, place the present problem in context by defining the general operation of a PPT. Figure 1.1 shows the basic components of a PPT. The schematic shows a rectangular, parallel plate geometry, for illustrative purposes. PPTs come in many other geometries (e.g., coaxial, linear pinch, etc.); however, the discussion which follows for the rectangular geometry describes the general operation of any PPT operating in the electromagnetic acceleration mode. The plasma discharge in a PPT progresses as follows. First, the volume between two electrodes, separated at the breech by an insulator, is filled with a working gas. High voltage (typically 1-15 kV) is then applied between the electrodes (typically a capacitor bank is connected to the electrodes with a high speed switch such as an ignitron). The gas between the electrodes then breaks down and current begins to flow. The initial current distribution is in the form of a planar current sheet along the face of the insulator at the breech. The current sheet forms at the breech because it is the path of least impedance available to the circuit; in a circuit with rapidly rising current, the inductive voltage drop, $V_L = L_o dI/dt$ (where, L_o is the initial inductance and I is the total circuit current (typically 10-100 kA)), dominates the impedance of the system and, hence, the circuit seeks the path of least initial inductance, which is at the breech. As the current rises, a transverse magnetic self-field (\mathbf{B}) forms behind current sheet; this magnetic field interacts with the current sheet to create an axially directed electromagnetic self-force, $\mathbf{F} = \int \mathbf{j} \times \mathbf{B} d^3x$. This force causes the current sheet to accelerate axially, away from the breech – sweeping up gas along the way (the current sheet is often referred to, figuratively, as an electromagnetic “snowplow”). At the end of the electrodes, the gas entrained in the current sheet is ejected (typically with a speed of 10-100 km/s) and thrust is derived (typically a 0.1-1 mN-s impulse bit).

1.1.2 History of the Pulsed Plasma Thruster

PPTs have the potential for fulfilling the attitude control requirements on a satellite at greatly reduced mass and cost. They are also being considered for constellation maintenance for missions such as interferometric imaging of the Earth from space or deep space from an Earth orbit (c.f., Polzin *et al*[5]). The

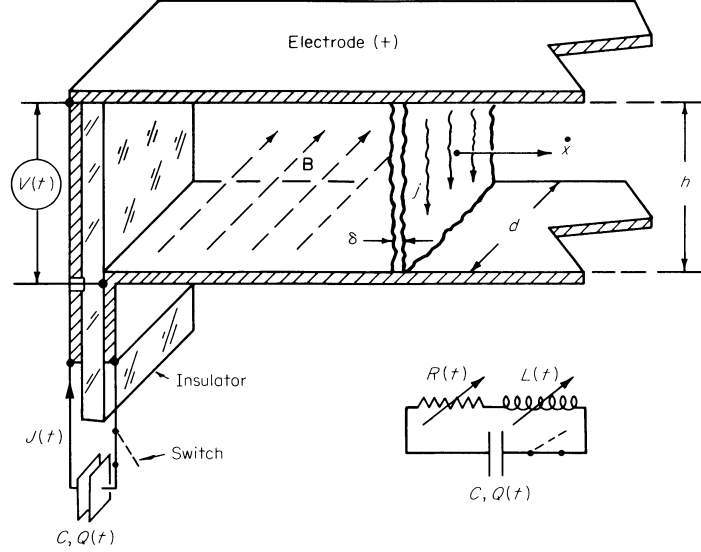


Figure 1.1: Schematic of pulsed plasma thruster components and circuit model[3].

benefits of PPTs are their simplicity, very small impulse bits for precise control of satellite motion, reliability, and high specific impulse. Two classifications of PPTs exist, corresponding to the form of propellant used: gas-fed (GFPPT) or ablative propellant (APPT). The gas-fed variety has the advantages of a “clean” exhaust plume and high specific impulse. The ablative version of the PPT uses a solid propellant, such as Teflon, to provide other advantages such as compactness and overall ease of system integration; however, plume contamination and lower specific impulse may limit the application of APPTs for some missions.

From about 1960 to 1968 PPT research focused on the gas-fed variant (GFPPT). The GFPPT was envisioned as a potential “primary” propulsion system, where the GFPPT would process large amounts of power (>100 kW) and provide enough average thrust (>1 N) to perform large Δv maneuvers, such as interplanetary missions. By the late sixties it was realized that a steady-flow electromagnetic accelerator, the MPD thruster[6], was better suited for this type of mission. A “secondary” propulsion niche, i.e., small Δv attitude control maneuvers, still existed for the GFPPT. However, at about the same time, the ablative variety of PPT (APPT) was gaining favor, mainly due to its mechanical simplicity. The GFPPT requires the storage of gaseous propellant under high pressure and a fast-acting valve to meter puffs of propellant into the discharge chamber. Further, the propellant feed system in the GFPPT is required to operate in a leak-free manner for many ($> 10^6$) shots. A qualified system capable of performing this demanding task was not available at the time and, hence,

only APPTs were flown[7].

This state of affairs remained until the mid-90's, when the negative issues related to propellant feeding in the GFPPT were ameliorated by the availability of flight-qualified valves and the development of high-speed solid-state electrical switching technology. The former development addressed the reliability issue, while the latter showed promise for substantially increasing the propellant utilization efficiency. These technologies were implemented in the thrusters of Ziemer *et al.*[8, 9, 10]. Still, with the addition of these new technologies, PPTs remain one of the least efficient electric propulsion systems ($\eta_t \sim 10\%$). However, the possibility of large incremental gains in performance make PPTs one of the most interesting devices, from a research perspective.

With the renewed interest in GFPPTs it is fitting and natural that there is a revitalized interest in understanding the physical principles which underlie PPT operation, in order to improve their performance. Careful review of the work of earlier researchers[11] shows that our understanding of the acceleration mechanism in PPTs is deficient in several areas. This study aims to help clear up one such area of ambiguity – current sheet canting.

1.1.3 Definition of the Problem

The phenomenon of current sheet canting is the departure of the current sheet from perpendicular attachment to the electrodes to a skewed, or tipped, attachment. It is best illustrated by an example. Figure 1.2 shows the evolution of two discharges near the breech of a rectangular-geometry pulsed electromagnetic accelerator; outlines of the electrodes (the cathode is the bottom electrode) have been added for clarity. Ideally, we would like the current sheet to initiate at the breech, perpendicular to the electrodes, and remain so as it propagates axially (as illustrated on the left-hand side of the figure). In contrast, the right-hand side of the figure shows the experimentally observed evolution of a discharge[12]. As expected, the current sheet is seen to initiate at the breech; however, as time progresses, the current sheet is seen to severely tilt, or cant, as it propagates.

The photographs shown in Fig. 1.2 were some of the earliest observations in an experiment designed to understand the basic macroscopic stability of current sheets under a variety of experimental conditions. The observed severity of the current sheet canting warranted further investigation and, hence, provided the topic for this study.

1.1.4 Importance of the Problem

Since the overall goal is to improve PPT performance, it is first important to identify why understanding current sheet canting will help us to build better thrusters. While direct measurements of the impact of canting on overall thruster performance remain to be carried out, we can make arguments which suggest that it may have adverse implications.

Canting creates off-axis components of thrust, which constitute a profile loss. Consider the $t = 8 \mu s$ photograph on the right-hand side of Fig. 1.2.

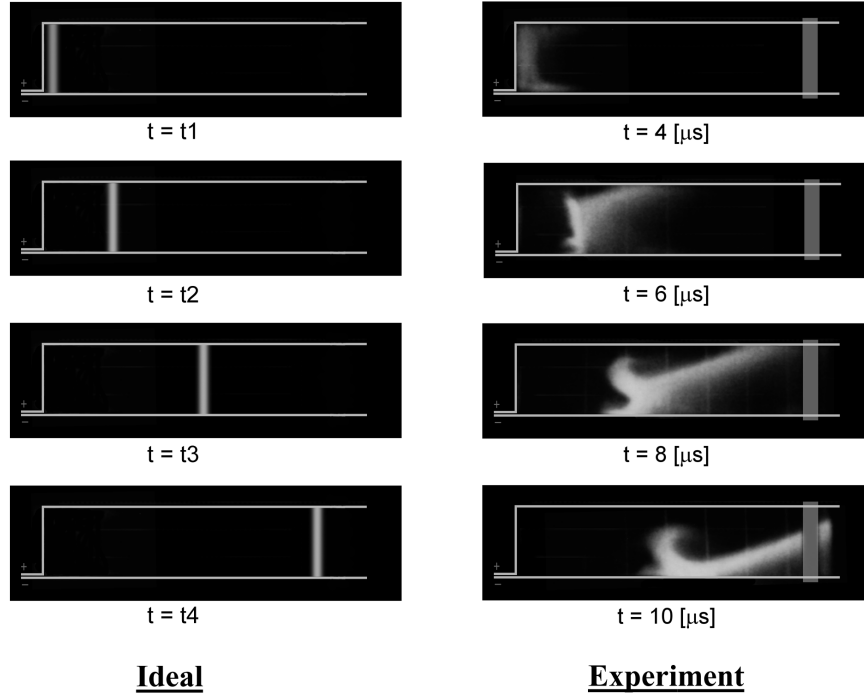


Figure 1.2: Comparison of ideal and experimentally observed current sheet propagation. In the ideal case, it is implied that time $t_1 < t_2 < t_3 < t_4$. The experimental photographs are from an argon (100 mTorr, uniform fill) discharge with peak current about 60 kA. Outlines of the electrodes have been added for clarity; the vertical rectangular element on the right-hand side of the pictures is a structural element that obstructed optical access.

Assuming that the magnetic field is uniform behind the current sheet, the force on the top electrode (which is found by integrating the magnetic pressure on the electrode surface) will be greater than on the bottom electrode, because the top electrode has more surface area exposed to the magnetic field. This transverse force imbalance may result in an undesirable torque on a spacecraft which uses a PPT. Also, considering the work done by the current sheet, it is clear that a canted current sheet will apply a force to the propellant transverse to the thrust axis and thus expend energy which is not converted into useful thrust.

In addition to causing an off-axis component of thrust, current sheet canting may undermine the effective sweeping up of propellant as the current sheet propagates. The effect of canting may be to force the plasma entrained by the current sheet into the cathode where it stagnates and is then left behind. Indeed, canted current sheets may act, undesirably, like *real* snowplows – never accumulating but, rather, throwing their load to the side as they pass by.

Again, while direct studies of performance degradation due to current sheet

canting are needed, the potentially adverse effects envisaged above provide reasonable justification for pursuing a detailed study of the phenomenon. By developing an understanding of the physical processes which drive current sheet canting, we can develop prescriptions for how to reduce the effect, and ultimately provide guidance for the design of better pulsed plasma thrusters.

1.2 Review of the Problem

A detailed review of past research on the subject of pulsed electromagnetic accelerators was presented in Ref. [1]. The scope of that review was limited to articles in which current sheet canting was either observed or commented upon. The information which is available indicates that the phenomenon was ubiquitous – occurring in a variety of different electrode geometries and experimental conditions. However, detailed treatment of the subject is limited, with most references to the phenomenon being anecdotal in nature – with the exception of work carried out by researchers at Avco-Everett Research Laboratory during the mid-sixties.

The review in Ref. [1] was arranged by research group (chronologically). Within each section, the major findings of each group were first summarized. These findings were then critiqued and contrasted with the findings of other research groups. In this report we present only the following summary of that review. The details can be found in that reference.

- Current sheets are always observed to cant with nitrogen and argon propellant – irrespective of geometry (rectangular, coaxial, z-pinch, inverse z-pinch, and parallel rod), gas pressure, or current level.
- Current sheet canting always occurs in an orientation such that the anode current attachment leads the cathode current attachment.
- Uncanted hydrogen and deuterium current sheets have been observed but only with specially prepared electrodes.
- Ion current conduction is believed to play an important role in establishing the overall current pattern.
- Current sheets appear to exhibit invariant features (e. g. anode foot, cathode hook, and canting) over a wide range of geometries, propellant species, gas pressures, and current levels.
- Conflicting experimental results exist with regard to the influence of polarity in coaxial accelerators, but variations in the construction (e.g., slotted electrodes) may account for the different observations.

The conclusions enumerated above show that current sheet canting has been observed in many studies. However, there was no unanimity of opinion as to its origin. Furthermore, no study has accurately quantified canting angles. The

present study attempts to address these deficiencies through targeted experiments and theoretical analysis. To isolate the current sheet canting effect we have followed the lead of Lovberg in using a rectangular geometry accelerator. This geometry eliminates the radial field variation found in the coaxial geometry, provides ease of diagnostic access, and is amenable to analytical studies. One significant difference in the present study is the use of a pulse forming network; almost all of the experimental results described in our review used sinusoidal waveforms. In doing so, the intent was to eliminate any phenomena that result from current transients and also make the analytical studies more tractable.

1.3 Experimental Apparatus

This section describes the components of the CSCX (Current Sheet Canting Experiment) experimental apparatus. The design rationale and performance of the accelerator, pulse forming networks, vacuum facility, and data acquisition equipment are described in detail.

1.3.1 General experimental layout

The basic components of the CSCX experimental apparatus are the accelerator, pulse forming network, vacuum facility, and data acquisition equipment. The general layout of these components is illustrated in Fig. 1.3.

Tables inside the vacuum chamber support the accelerator and provide mounting surfaces for optics and diagnostic probes. A $4' \times 6'$ optics table, positioned next to the tank, was used to lay out optical diagnostics. Glass windows on the sides of the vacuum chamber provided optical access to the accelerator discharge. Two Faraday cages were used to house the data acquisition equipment.

The overriding design rationale was to create an accelerator configuration which provided convenient access to optical and probe diagnostics. Furthermore, it was desired that the configuration would be amenable to analytic modelling (e.g., one-dimensional electromagnetic fields, constant current, etc.). Details about each of the major components of the apparatus are given in the remaining subsections.

1.3.2 Accelerator

The CSCX Accelerator is a parallel-plate pulsed plasma accelerator with glass sidewalls (a schematic illustration with relevant dimensions is shown in Fig. 1.4). The dimensions of the discharge chamber were chosen to be similar to those found to “work” by earlier researchers (see, for example, Eckbreth[13]). The electrodes are made of copper and the sidewalls are made of Pyrex. The sidewalls reduce the region accessible to the discharge to 10 cm (width), whereas the electrodes themselves are 15 cm wide. The motivation for using Pyrex sidewalls is several-fold: first, they provide an excellent optical view of the discharge, second, they isolate the current sheet to a well-defined spatial region, third,

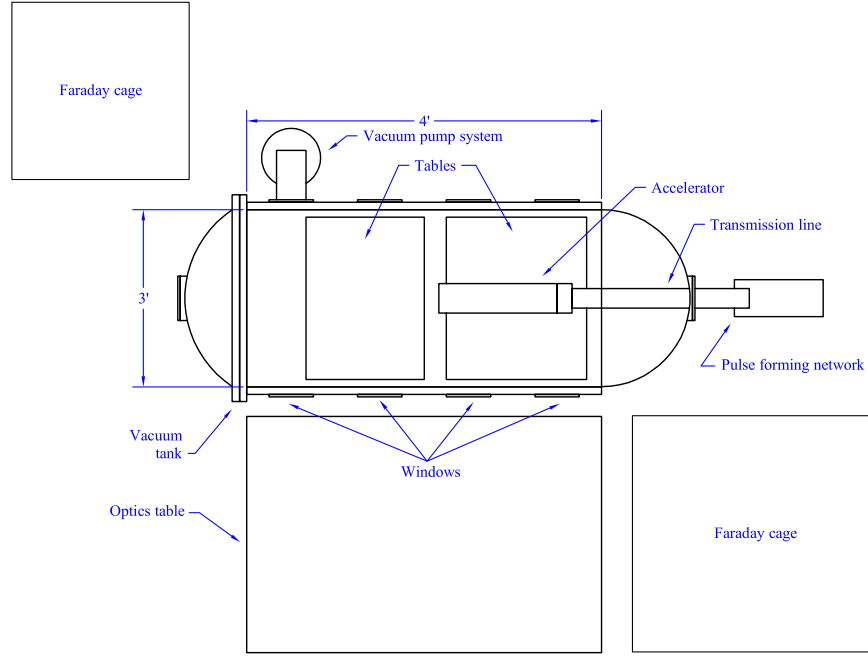


Figure 1.3: Top-view schematic of the general experimental layout.

they isolate the discharge from electric field singularities which are associated with the sharp edges of the electrodes, and last, they isolate the discharge from the rapidly fringing magnetic field at the edges of the electrodes. The two latter benefits tend to make the discharge environment more conducive to the formation of spatially uniform current sheets.

Propellant loading was accomplished using the ambient fill technique. After the vacuum tank was pumped down to its base pressure (1×10^{-5} Torr), the entire tank was brought to the desired operating pressure with the chosen propellant (hydrogen, deuterium, helium, neon, argon, krypton, xenon, and methane were used in the present study). This resulted in a uniform gas distribution within the accelerator prior to discharge initiation. Approximately ten pulses at full capacitor bank voltage were executed before taking data in an attempt to remove adsorbed gases from the electrodes. It is uncertain whether or not this preparation technique was sufficient to remove contaminants from the electrodes.

In general, the accelerator performed very well; current sheets were generated in the expected manner (i.e., formation at the breech and propagation to the exit) and the experiments were very repeatable. High speed photographs (see subsection 1.9) taken of different discharges (with the same initial conditions and same camera time delay) were practically indistinguishable.

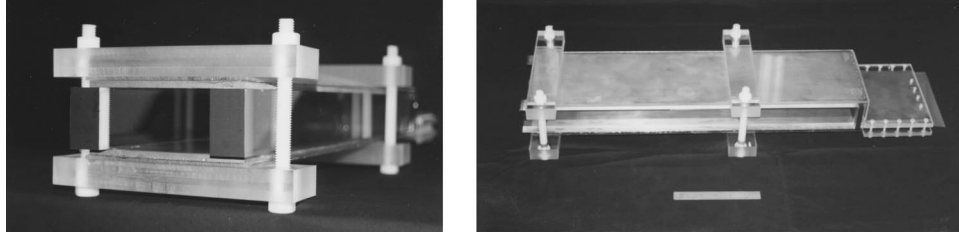
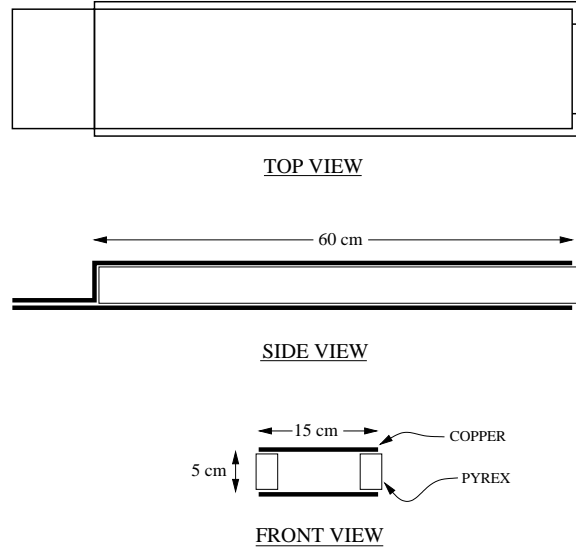


Figure 1.4: Schematic and photographs of the CSCX accelerator.

1.3.3 Pulse forming networks

The accelerator was powered by a pulse forming network (PFN). Two different PFNs were used in the experiments; this was necessitated by a failure of two of the capacitors in the original capacitor bank. This subsection describes the basic design of the two PFNs; details about the designs (e.g., calculation of component values, numerical circuit simulations, etc.) are given in the appendix of Ref. [1].

The values of the electrical components at each stage of the PFNs were chosen to give a nearly flat current profile with a pulse width that corresponds to the time it takes the current sheet to traverse the length of the accelerator. Assuming a sheet propagation speed of $2\text{--}3\text{ cm}/\mu\text{s}$ (which is typical of gas-fed pulsed plasma accelerators found in the literature), a pulse width of approximately $20\text{--}30\text{ }\mu\text{s}$ is required to allow the current sheet to traverse the (60 cm) length of the electrodes. With a given set of capacitors, electrical design of each

PFN entailed determining the proper stage inductance to give the desired pulse length.

As described in Ref. [1], it is desirable for the current rise rate (dI/dt) to be as large as possible. Since $dI/dt \propto V_o/L_o$ (L_o is the initial, or parasitic, inductance, V_o is the initial capacitor bank voltage), special care was taken to configure the conductors which connect the PFN to the accelerator in a low inductance geometry.

The final designs of PFN I and II are described below. Detailed electrical, electromagnetic, and mechanical design notes are given in the appendix of Ref. [1] along with a complete electrical schematic of the CSCX power supply.

PFN I

Eight capacitors from the LES 8/9 series of ablative PPTs[14] were available to be used for PFN I. These cylindrical capacitors have a capacitance of about $18 \mu\text{F}$ and are rated at 3 kV. In the experimental configuration, each stage of PFN I was composed of an $18 \mu\text{F}$ capacitor in series with a 60 nH inductor. The bank voltage was generally set to 5 kV, yielding a total discharge energy of about 2 kJ. The PFN was switched into the accelerator using an ignitron. The peak current was approximately 60 kA (with 5 kV bank voltage), with an initial rise rate on the order of 10^{10} A/s. The duration of each pulse was about $20 \mu\text{s}$, which was followed by one cycle of damped ringing. The experimentally measured current waveform closely followed the design waveform, up to the point of voltage reversal. Examples, and more detailed analysis, of these waveforms are given in Section 1.7.

PFN I experienced a catastrophic short-circuit which destroyed two of its capacitors, after having successfully generated about three thousand pulses over a period of about two years. The failure was most likely due to continually charging the capacitors above their rated voltage.

PFN II

PFN II was designed to replace PFN I. Custom-made capacitors were obtained from Maxwell Technologies, Inc.. These rectangular capacitors have a capacitance of $10 \mu\text{F}$ and are rated at 10 kV. Higher voltage capacitors (compared with PFN I) were chosen in order to generate higher dI/dt and peak currents – which leads to better defined current sheets. Dual-ended capacitors were selected for ease of mechanical assembly. PFN II used ten stages; each stage was composed of a $10 \mu\text{F}$ capacitor in series with a 100 nH inductor. The bank voltage was generally set to 10 kV, yielding a total discharge energy of 5 kJ. The PFN was switched into the accelerator using an ignitron. The peak current was approximately 75 kA, with an initial rise rate on the order of 10^{11} A/s. The duration of each pulse was about $20 \mu\text{s}$, which was followed by one cycle of damped ringing. The experimentally measured current waveform followed the design waveform, up to the point of voltage reversal. Examples, and more detailed analysis, of these waveforms are given in Section 1.7.

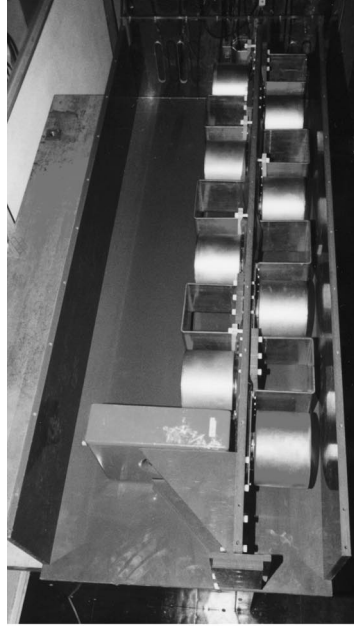
PFN IPFN II

Figure 1.5: Photographs of complete PFN assemblies.

1.3.4 Vacuum facility

The vacuum facility used in this experiment (see figure 1.3) is described in detail by Jahn [15]. The vacuum vessel is a 3' diameter, 6' long cylindrical tank made entirely of Plexiglass (which has been shown to eliminate the electromagnetic interactions sometimes found in metallic vessels), with glass optical access windows. Gases are introduced into the tank using a regulated feed-through. The tank uses a diffusion pump with a freon-cooled trap to achieve a base pressure of 1×10^{-5} Torr. Sub-milliTorr pressures were measured with a CVC cold cathode gauge. All pressures above one milliTorr were monitored using a MKS Baratron vacuum gauge; this gauge gave a gas-species-independent reading which allowed an accurate measurement of the initial propellant pressure in the accelerator.

1.3.5 Data Acquisition Equipment and Noise Suppression

The data recording equipment used in the experiments consisted of a digital oscilloscope, a high-speed film camera, two CCD cameras, and a personal computer. The oscilloscope, a Tektronix TDS 460A, is capable of sampling signals at up to 200 MHz – much faster than any time-varying phenomena which were observed in the present work. A Dell XP200 computer was used to record oscilloscope waveforms, via a GPIB connection and Labview software. The oscilloscope and computer were housed in a Faraday cage to suppress RF noise pickup. Specifications for the cameras are given in Section 1.4.

Pulsed power experiments can suffer from undesirable electromagnetic coupling of the various experimental and diagnostic equipment components. These interactions can introduce noise, cause components to trigger out of the desired sequence, or even destroy some sensitive electronic equipment. To avoid these negative effects, in addition to the use of Faraday cages, two measures were taken: a single point ground and optical isolation of all trigger circuits.

In order to maintain a constant potential reference (ground) in the lab space, almost all of the lab floor was covered with copper sheet (200 square feet). A large diameter copper ground wire (size 00), which is connected to a large copper plate buried outside the building, was connected to this sheet. All equipment (charging circuitry, Faraday cage, oscilloscope, etc.) used this copper sheet as their ground reference. This helped to eliminate ground-loops, which can cause high voltage transients in equipment when the accelerator is fired.

Many of the diagnostic experiments relied on the accurate sequential triggering of several components of the experiment. For example, the schlieren photography experiment required that the camera, accelerator, oscilloscope, and laser to be triggered in the given order and with specific time delays between each trigger. It was observed that because all of the components were connected, RF noise, reflections, etc., created in one device could travel through interconnecting BNC cables and cause another device to trigger prematurely. To eliminate this effect, an optical isolation scheme was implemented. A six channel box in which the input and output signals are optically coupled via optocouplers and TTL line drivers was constructed. This box only allows signals to travel from the input BNC to the output BNC. Spurious signals that enter from the output side are not communicated back through the input; thus, cross-talk between the components is eliminated. The electronic details of this box are given in the Appendix of Ref. [1].

1.4 Diagnostics

This section gives detailed descriptions of the diagnostics which were applied to obtain both qualitative and quantitative information about the current sheet plasma in the CSCX accelerator. Details regarding calibration of the diagnostic devices are given in the appendix of Ref. [1].

1.5 Circuit current measurement

The total current delivered to the CSCX accelerator was measured using a commercial current transformer. Both PFN I and II used a Pearson Model 301X current transformer located between the final capacitor/inductor stage and the accelerator (see figure 1.5.) No calibration procedure was carried out to verify that the published characteristics were accurate; however, the simplicity and ruggedness of the device make it unlikely for it to fall out of calibration. The published specifications for the current monitor are given in the appendix of Ref. [1]. The output of the transformer (with two calibrated 50Ω 10X attenuators in series) was recorded using a Tektronix model TDS-460A digital oscilloscope.

1.6 Voltage measurement

The terminal or “muzzle” voltage in a pulsed electromagnetic accelerator represents the contribution of the plasma resistive voltage drop and the sheath potential; since little to no magnetic flux exists in front of the current sheet, a terminal voltage probe does not detect the (very large) inductive voltage drop that occurs behind the current sheet. Therefore, by measuring the terminal voltage drop, a rough estimate of the plasma resistivity can be calculated[16].

The development of a specialized voltage probe was necessitated by the wide range of voltages to which the probe is exposed. Just before the discharge initiation, the probe is exposed to the full bank voltage (~ 10 kV). As the current sheet propagates the probe sees only the resistive and sheath voltage drop (~ 100 V). Finally, when the current sheet reaches the end of the electrodes, the probe measures both the resistive and inductive voltage drop (~ 1 kV). Furthermore, because of the highly transient nature of the discharge, both accelerator electrodes may float up to high voltage relative to the ground potential. This latter situation poses a serious threat to any data acquisition equipment (e.g., an oscilloscope) connected to the voltage probe. Two measures were taken to enable an accurate and safe measurement of the terminal voltage in the present study: a differential high voltage probe was constructed, and a battery powered, floating oscilloscope was used to record the probe output. A differential voltage probe measures the potential difference between two electrodes directly without reference to an external reference potential, that is, it is insensitive to the electrodes instantaneous potential relative to the ground potential.

The voltage probe used in the present study was a differential probe with 100:1 attenuation and both DC and AC compensation elements. The construction details and the calibration procedure are given in the appendix of Ref. [1]. The output of the probe was recorded on a Tektronix model 3032 battery powered digital oscilloscope.

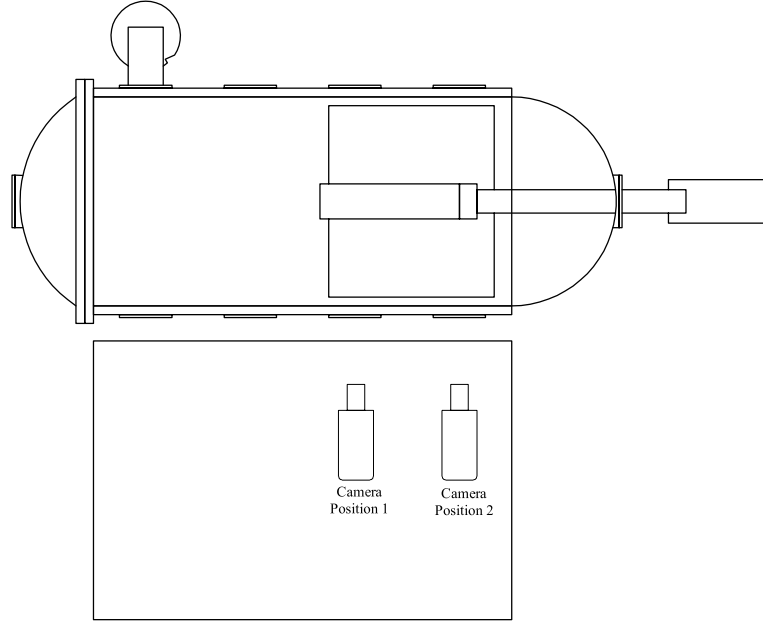


Figure 1.6: Schematic of high speed photography experimental layout.

1.6.1 High-speed photography

The camera used in this study, a Hadland Photonics Imacon 792LC, is capable of taking pictures at a rate of up to 20 MHz and provides up to sixteen images printed on Polaroid film. In the experiments presented here, the framing rate was set to 500 kHz; the exposure time for each image was 400 ns. This camera was useful for creating movies which show how the discharge evolves spatially during the entire pulse.

The layout of the photography experiment is shown in Fig. 1.6. The camera was placed at one of two positions. Position 1 was used to photograph the breech section of the accelerator; position 2 was used to photograph the mid-section. In order to more easily visualize the spatial position of the current sheets and to estimate the size and orientation of current sheet features, a black screen with white gridding (1 cm spacing) was placed on the outside of one side of the accelerator. The propagation speed of the current sheet was estimated by comparing successive frames in a single shot (with known inter-frame time delay). The canting angle was estimated graphically, using the photographs, by drawing two lines, one parallel to the cathode and one parallel to the luminous front, and measuring the angle between them.

1.6.2 Schlieren imaging

Since the photographs obtained in the present study relied on monitoring optical emission, they may not necessarily show the position of the current sheet. A more direct method is to visualize the current sheet through light refraction as it passes through its steep electron gradients.

The term “schlieren techniques” refers to the broad class of optical diagnostics which exploit the fact that light from a source external to a test object (a flowing gas, for example), when made to pass through it, will be refracted by any density gradients which exist in the flow. After passing through the flow, with appropriate optical arrangements, the refracted and un-refracted light can be separated to yield an image with dark and light areas which correspond to disturbed (i.e., areas where density gradients exist) and undisturbed regions of the flow, respectively. So, in the case of visualizing current sheets, the high electron density gradient associated with a thin, propagating current sheet should produce an image with high contrast in the areas which correspond to the spatial extent of the sheet. It was hoped that visualization of the current sheet using schlieren techniques would give better spatial and temporal resolution of the position of the current sheet, since these techniques rely upon directly imaging electron density gradients. This would allow for more accurate calculation of properties such as canting angle and sheet sweeping speed.

Schlieren techniques have been used by earlier researchers to visualize current sheets. Notably, both Lovberg *et al.*[17] and MacLelland *et al.*[18] used schlieren photography with parallel plate accelerators similar to the device used in the present work. We have implemented a wide variety of optical arrangements, which are described below, in an attempt to obtain similar results.

Light source

Pulsed Nd:YAG lasers were used in all of the schlieren experiments. The first, a Continuum Minilite II, was capable of generating a 5 ns burst of radiation (532 nm, 25 mJ). The second, a Continuum NY61-20, was rated at up to 100 mJ at 532 nm. In both cases, the output energy was not measured, so it is uncertain if the lasers were operating at their peak capability.

Camera

The camera used to acquire images was a Kodak DCS 460 digital camera. This camera has a mechanical shutter and a six million pixel color CCD array. A 532 nm laser line filter was placed over the camera lens in order to discriminate laser light from the accelerator plasma emission. Acquired images were downloaded directly to the data acquisition computer.

Schlieren optical arrangements

Schlieren techniques are well developed and have been used to visualize many different types of flows. The basic principles of the method can be found in the

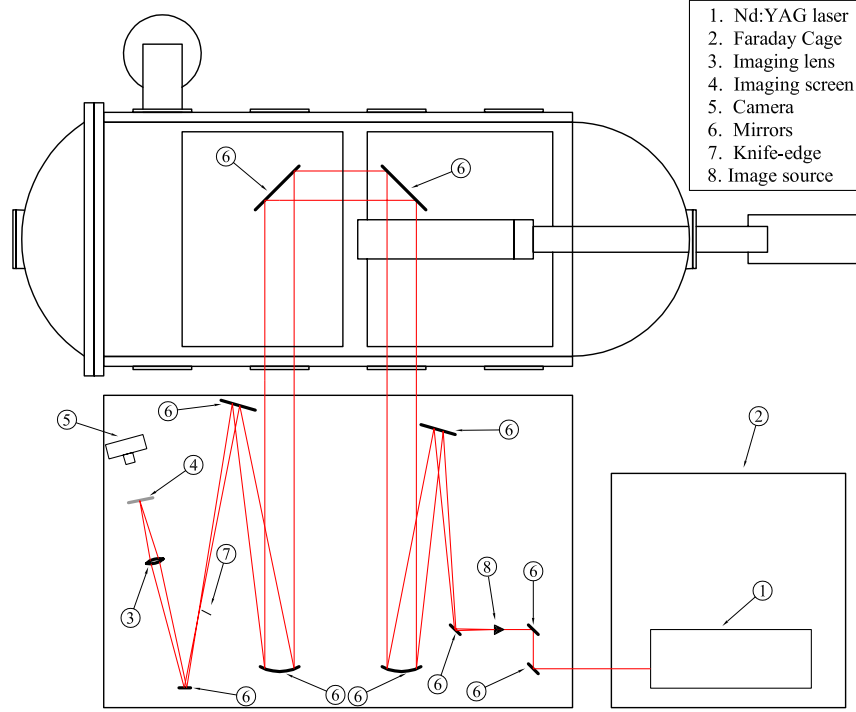


Figure 1.7: Schematic of schlieren photography optical arrangement.

standard references[19]. Four optical arrangements were used in the present experiments – the conventional schlieren and three variations of the shadowgraph configuration.

Conventional schlieren layout The most complicated of the optical arrangements used was the schlieren photography arrangement. Figure 1.7 shows the schlieren photography experimental configuration used in the present study.

Schlieren photography involves imaging a light source through a system of optical elements. The criteria for a useful schlieren photography light source are that it have a *finite size* and that it *radiates isotropically*. A laser, which has a very small cross-section and is highly collimated, violates both of the criteria. In order to use our lasers as a light source, the beams were expanded with a microscope objective and diffused through a masked opal glass slit (2 mm x 10 mm). Six inch diameter mirrors were used for both the collimating and focussing lenses. A razor was used as a knife edge and the centerline of the accelerator electrodes was imaged onto a ground glass screen using a 3" lens.

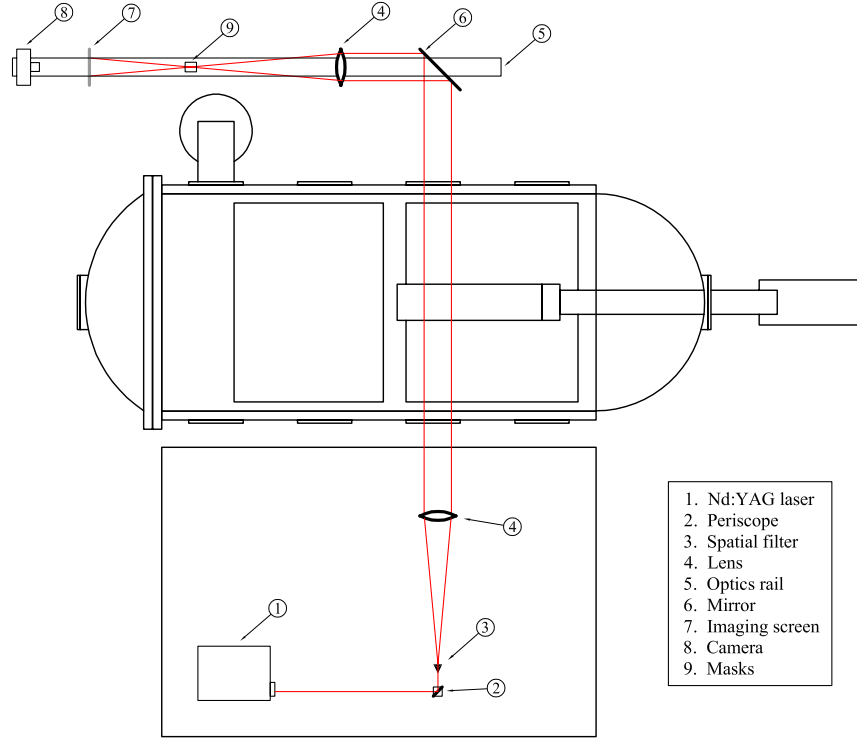


Figure 1.8: Schematic of shadowgraph optical arrangement.

Shadowgraph configuration The shadowgraph configuration is the simplest of the optical arrangements used. The source and collection optics for this configuration are shown in figure 1.8. Unlike in the schlieren photography arrangement, in the shadowgraph configuration it is desirable to have the smallest source size possible; in our experiments the laser was passed through a spatial filter with a $25\ \mu\text{m}$ pinhole to provide a small source as well as to expand the beam to the desired diameter (~ 4 in.). Six-inch diameter lenses were used for both the collimating and focusing lenses. The collection optics consisted of only a focusing lens and a ground glass plate.

Modified Shadowgraph Configurations In the modified shadowgraph scheme the source optics are the same as in the standard shadowgraph configuration. The difference lies in the collection optics, which use masks at the focal plane of the focusing lens to intercept (or pass) refracted rays. The masks allow the modified shadowgraph technique to have (theoretically) near-infinite contrast. Two different types of masks were used in the present study: a pinhole aperture and a “dot” mask (see Fig. 1.9). The pinhole aperture allows all of the unrefracted light to pass, resulting in a shadowgraph image with an illuminated

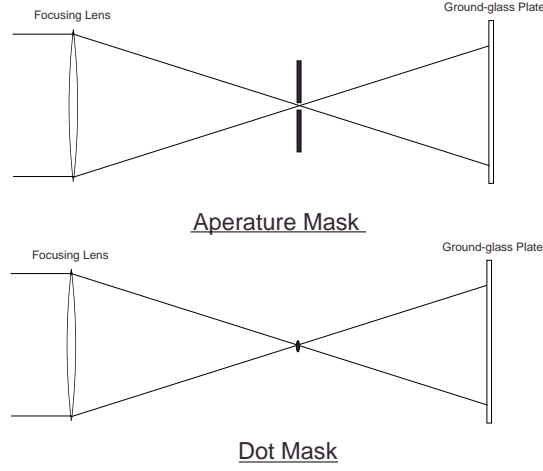


Figure 1.9: Schematic of modified shadowgraph collection optics.

background and dark striations, while the dot mask produces the opposite effect – illuminated striations on a dark background.

Experimental timing

The component trigger timing requirements in the schlieren photography experiments were especially stringent because the timing of three instruments had to be carefully coordinated. A Stanford Research digital delay generator (model DG535) and the optically isolated trigger box (see subsection 1.3.5) were used to: 1) open the shutter on the camera, 2) fire the accelerator, and 3) fire the laser when the current sheet had reached the imaging location. The accelerator current waveform and laser q-switch timing signal were monitored on an oscilloscope to assure that the laser was firing at the desired time in the current pulse.

1.6.3 Magnetic field probes

Magnetic field probes were used to determine the current sheet canting angle by monitoring the response of two probes at different spatial locations and inferring the spatial configuration of the current sheet through a time-of-flight analysis.

The magnetic field probes used in this study were magnetic induction coils, commonly referred to as B-dot probes. These probes are simply linear coils of wire that generate an emf proportional to the time variation of the magnetic flux through the coil. So, experimentally, we determine the local magnetic field by evaluating the expression

$$B(t') = \int_0^{t'} c(\omega) V(t) dt \quad , \quad (1.1)$$

where V is the measured probe voltage and $c(\omega)$ is a (frequency-dependent) parameter determined through calibration.

Two sets of B-dot probes were used in the present study. Probe set I was acquired from an earlier experiment[20] (the details of the probe set I construction are shown in Fig. 1.10a). Construction of probe set II was necessitated by the destruction of one of the probe set I probes, which resulted from spurious arcing from the main discharge to the probes shielding (the details of the probe set II construction are shown in Fig. 1.10b). The probes were calibrated by placing them in the uniform-field region of a Helmholtz coil; pulses of known current and frequency were driven through the Helmholtz coil and the probe response was recorded (see the appendix of Ref. [1]). The probes' frequency response is expected to be linear in dB/dt (i.e., $c(\omega) = c$, a constant) through $\omega \leq 100$ MHz, due to the probes' low inductance; however, we verified the linearity only up to approximately 2 MHz, which was sufficient for our purposes. No analog integration was used; instead, the probe voltage was measured directly and integrated numerically to determine $B(t')$.

The probes were used in two different configurations, as illustrated in Fig. 1.10b and Fig. 1.10c. In configuration 1, the probes were placed inside the accelerator in the same horizontal plane (separated by approximately 2.5 cm), and separated axially by approximately $\Delta x_1 = 20$ cm. During a discharge the two probe responses were simultaneously monitored. By dividing the known axial probe separation by the difference in the arrival time of the current sheet to each probe (Δt_1), the average current sheet propagation speed ($v = \Delta x_1 / \Delta t_1$) was determined. In configuration 2 the probes were placed at the same axial position, but vertically displaced by approximately $\Delta y = 3$ cm. By measuring the time delay between the arrival times of the current sheet to each probe (Δt_2), and multiplying by the previously determined value of v , we can determine the axial displacement of the current channel ($\Delta x = v \Delta t_2$) and, hence, the current sheet canting angle ($\tan \theta = \Delta x / \Delta y$) relative to the electrode normal.

Probe set I was used in fixed locations near the axial center of the accelerator. Probe set II was used to map the axial evolution of the magnetic field. The probes were mounted on an electrically actuated translation stage which allowed their position to be continuously adjusted from the breech to the exhaust.

1.6.4 Laser interferometry

A two-chord heterodyne laser interferometer with electronic quadrature phase detection was constructed. The system is very similar to the single-chord system implemented by Spanjers *et al.*[21] in APPT research. A schematic of the experimental layout is shown in Fig. 1.11. The interferometer was used to determine the current sheet speed and canting angle by monitoring the phase variations of two laser beams at different spatial locations within the accelerator and inferring the spatial configuration of the current sheet through a time-of-flight analysis in a completely analogous manner to that used in the analysis of the magnetic field waveforms. The response from two horizontally separated beams (approximately 10 cm axial separation) were used to determine the propagation

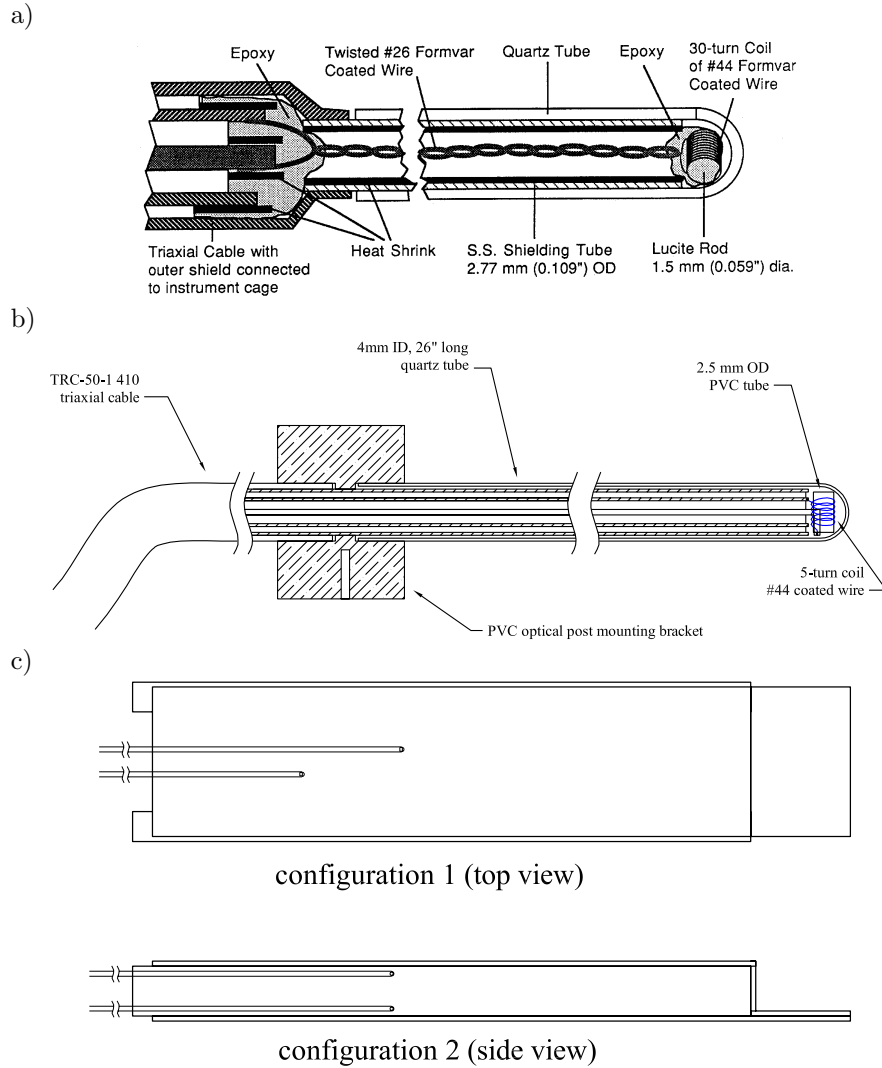


Figure 1.10: Magnetic field probe schematics: a) probe set I construction details (from Hoskins[20]), b) probe set II construction details, c) probe placement for speed (configuration 1) and canting angle (configuration 2) determination.

speed (the orientation of the optics for this experiment is illustrated in Fig. 1.11). The beams were retro-reflected back through the plasma to give twice the phase shift of a single pass. For canting angle determination, two beams at the same axial location but vertically separated by about 3.5 cm were used. Additionally, accurate quantitative measurements of the current sheet electron density were obtained from the measured phase shift in each beam.

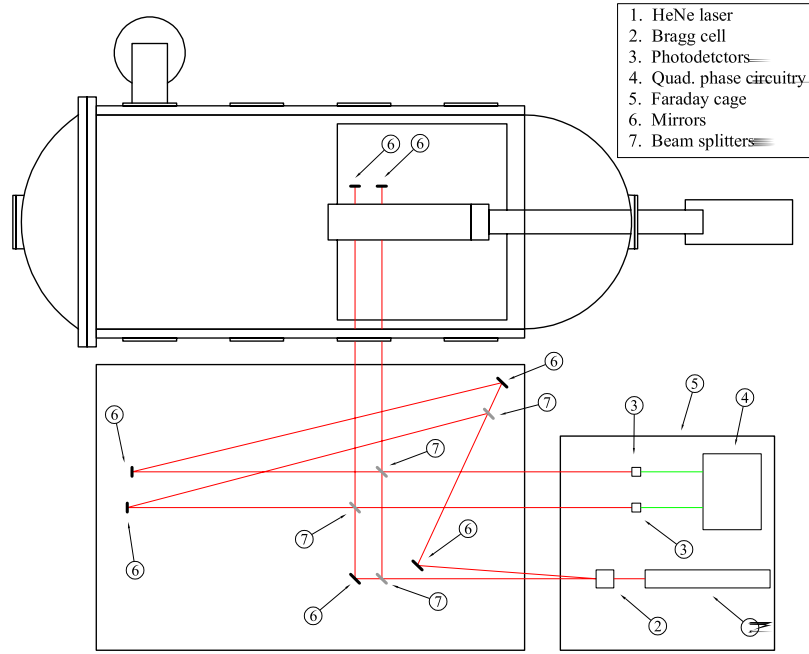


Figure 1.11: Schematic of laser interferometry layout (configuration 1).

The system functionally consists of two interferometers in the Mach-Zehnder configuration. This type of interferometer detects phase differences between the “scene” and “reference” beams. When these two beams are recombined at the detector, any phase mismatches between the beams causes amplitude variations in the detector output due to constructive or destructive interference. In our experiment, phase differences between the two paths arise when the current sheet plasma passes through the scene beam; the plasma index of refraction (\mathcal{N}) is different than that of free space (\mathcal{N}_0) and, hence, the scene beam optical path changes as the current sheet passes by. By measuring the phase change of the scene beam we can determine the change in optical path length and, in turn, the effective index of refraction of the plasma. Finally, through a suitable theoretical model of the interaction of the laser beam’s electromagnetic wave with the plasma, the electron density of the plasma can be determined.

The simplest model of the plasma-EM wave interaction assumes a weak magnetic field and isotropic plasma – the plasma is essentially considered to be a dielectric. Within this framework, analysis (see the appendix of Ref. [1]) leads to an expression for the electron density as a function of the instantaneously measured phase shift which, in our particular implementation reduces to

$$n_e = 2.78 \times 10^{15} \Delta\phi [\text{cm}^{-3}] . \quad (1.2)$$

Two problems arise in the interpretation of data obtained with a conventional

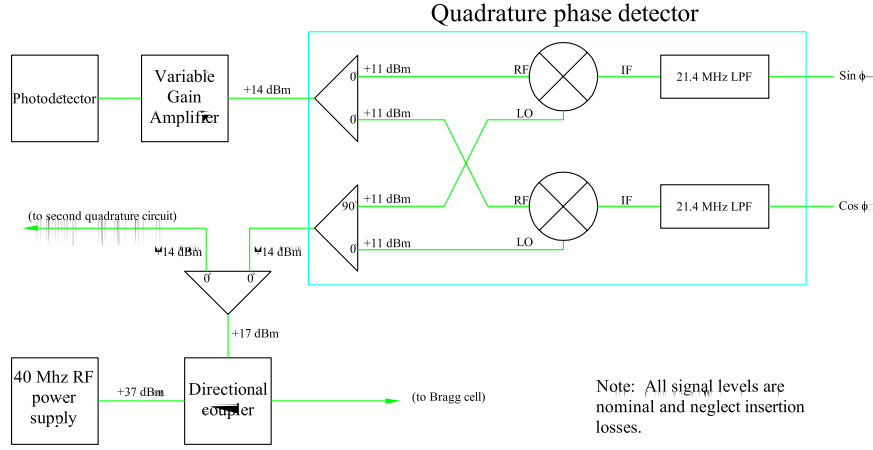


Figure 1.12: Schematic of one channel of the interferometer quadrature phase detection circuitry.

Mach-Zehnder interferometer: amplitude variations in the detected signal which arise from attenuation or refractive bending in the plasma must be distinguished from phase variations, and, in general, it is not possible to determine the direction of the phase change (i.e., positive phase changes cannot be distinguished from negative ones). These problems can be eliminated by using a heterodyne light source and quadrature phase detection. In a heterodyne system, either the scene or reference beam is phase modulated at the source; when the beams are recombined at the detector the amplitude of the detected signal will oscillate at the modulation frequency; the task of detecting the phase changes due to the plasma becomes that of measuring the phase of the oscillation at the detector relative to the driving modulation at the source. The technology for this type of measurement, which is essentially one of homodyne detection, has been well developed by the radio reception community. Drawing on this knowledge, we have developed a two-channel quadrature phase detector. Each channel uses two double balanced mixers to produce output signals proportional to the sine and cosine of the instantaneous phase and, hence, unambiguously determines the quadrant of the phase angle. A schematic of one channel of the phase detection circuitry is shown in Fig. 1.12.

The specific components used in the interferometer were as follows. The light source was a Coherent model 31-2108 17 mW HeNe laser. The beam splitting into the scene and reference beams, along with modulation of the reference beam, was accomplished using an IntraAction model AOM-405 acousto-optic cell driven by a 40 Mhz, 5 W RF power source. Two Thor Labs model PDA155 photo detectors were used. These amplified (1×10^4 V/A) Si detectors have a 50 Mhz bandwidth. It was found that, because of the large amount of electromagnetic noise created by the firing of the accelerator, all electronics, including the laser, had to be housed in a Faraday cage. Standard optical components

(aluminized mirrors, dielectric beam splitters, and anti-reflection windows) were used to steer the beams.

No direct calibration of the instrument was carried out (i.e., the response of the system to a known change in optical path length was not attempted). It is difficult to conceive of how such a procedure could be accomplished. The phase variations measured by the detector due to room vibrations and atmospheric fluctuations alone reduce the useful time scale of the device to experiments which last less than 100 μsec . It is unclear how one would introduce an object of known optical path length into the scene beam on such a short time scale. We have, however, based simply on signal-to-noise ratio considerations, estimated the minimal resolvable variation in electron density in our device to be on the order of $1 \times 10^{14} \text{ cm}^{-3}$. On the high frequency end, the Nyquist criterion limits the frequency response to about 10 MHz. From Eq. 1.2, this implies that the maximum resolvable temporal variation in electron density was about $10^{17} \text{ cm}^{-3} \mu\text{s}^{-1}$. As will be shown later, this limit was exceeded in some measurements near cathode; the complications which resulted are described in the appendix of Ref. [1]. The spatial resolution of the interferometry system, which was limited by the laser beam diameter, was about 3 mm.

1.6.5 Emission spectroscopy

Interpretation of spectral emission lines requires theory to predict both the wavelength and intensity of emitted radiation. The wavelength of the acquired lines is readily correlated with atomic species using standard tables [22]. The intensity of the emitted lines is related to the thermodynamic state of the plasma. This opens up a diagnostic avenue – by measuring the intensity of the radiation emitted by a plasma, we can infer bulk thermodynamic properties, such as temperature.

One such technique uses the ratio of spectral line intensities to yield a measure of the electron temperature. The principle of this technique is as follows. If the electrons in a plasma are in equilibrium (i.e., have a Maxwellian distribution of speeds), then the atomic species with which they are collisionally coupled will be in excitation equilibrium, that is, the bound electrons will be in a Boltzmann energy distribution. The actual distribution of excited states in a plasma is revealed when electrons in excited states relax to lower energy states and radiate light. By measuring the intensity of this light, we can infer the population of a particular upper state. Carrying out this procedure for many different transitions, we can determine the energy distribution of the bound electrons. Knowing this distribution, we can calculate the temperature of the free electrons needed to achieve the measured distribution of excited states.

Emission spectroscopy was used in the present experiment to obtain information about the atomic species present in the current sheets as well as to determine the electron temperature. In this subsection the general layout of the spectroscopy apparatus, calibration techniques, and the underlying principles used to interpret the spectral data are described.

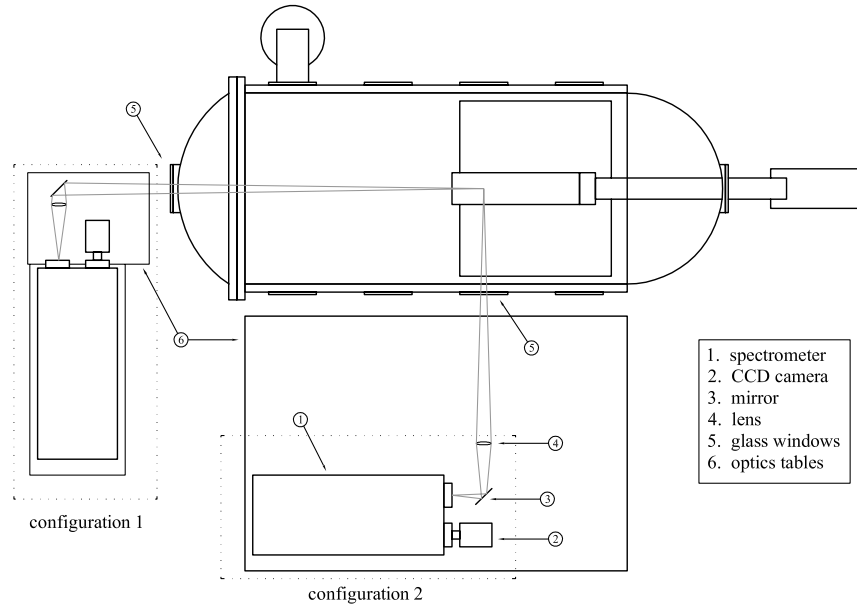


Figure 1.13: Schematic of emission spectroscopy optical layouts.

Apparatus

Spectral data was recorded by imaging the CSSX accelerator plasma in two different orientations (see Fig. 1.13). Configuration 1 was used to construct a time-integrated survey of all of the radiation emitted between 3500-8500 Å. In configuration 2, a few selected lines were interrogated to provide a measurement of the electron temperature. In both cases, a point on the centerline of the accelerator was imaged onto the input slit of the spectrometer. Configuration 2 was used in the quantitative work because it was easier to verify that the current sheet was in the same spatial location from shot to shot. If configuration 1 had been used, differences in the spatial position of the current sheet from shot to shot would have caused the current sheet to be intermittently out of focus and, consequently, these variations would have been indistinguishable from differences in plasma optical emission intensity. In configuration 2, the plasma had no component of velocity perpendicular to the imaging plane and thus decoupled the measured intensity from the propagation of the current sheet.

Light collection optics The light collection optics consisted of a vacuum chamber window, a periscope, and a focusing lens. The window, an 8 inch diameter, 1/2 inch thick soda lime glass disk, allowed the entire front view of the accelerator to be imaged. The periscope, which used two 3 inch diameter first surface mirrors, allowed the vertical position of the accelerator image to be adjusted to the level of the input slit of the spectrometer. Also, the periscope

rotated the image ninety degrees, so that the horizontal plane of the accelerator was aligned with the (vertical) spectrometer slit. The image plane of the spectrometer was aligned with the centerline of the accelerator. The spectral data presented in this study result from the integration of all light emitted by the plasma in this plane.

Spectrometer The spectrometer used in this study was a Spex 1269 grating spectrometer. The slit-to-mirror length is 1 m and the grating has 1200 groove/mm; the grating blaze angle is optimized for optical wavelengths. This configuration results in an exit plane linear dispersion of $D = 9.08 \times 10^{-3} \text{ \AA}/\mu\text{m}$ at 4000 \AA (D varies slightly with wavelength.) The grating angle (wavelength position) of the spectrometer was adjusted using a Spex Compudrive spectrometer controller.

Camera The detector used in this study was a Princeton Instruments ICCD 576 CCD camera. The camera has an array of 576×384 square $22 \mu\text{m}$ pixels. The quantum efficiency of the pixels is optimized for optical wavelengths. The array is both intensified and temporally gated. Photoelectron amplification of up to 1000:1 is continuously adjustable. A microchannel plate allows the CCD array exposure time to be adjusted from 10 ns to continuous exposure. The camera was gated using a Princeton Instruments PG-200 pulse generator. Camera images were acquired using a Princeton Instruments ST-138 controller and downloaded to a computer.

Calibration and data reduction In order to determine plasma species and make quantitative estimates of electron temperature, it was necessary to calibrate the spectroscopic system for wavelength and intensity. The details of the procedure used in the present study are given in the appendix of Ref. [1].

Computer code was written to automate the process of data reduction. The code takes raw CCD intensity information and interprets a curve of intensity versus wavelength – applying both wavelength and intensity calibration.

Plasma Spectroscopy

The primary motivation for implementing the emission spectroscopy diagnostic was to measure the electron temperature of the current sheet plasmas. The methodology for correlating the measured plasma optical emission with electron temperature is well developed[23]. In particular, we plotted the weighted optical emission versus photon energy (for several spectral lines of a given species) and inferred electron temperature from the slope of a straight-line curve fit through these points. A complete description of this technique, as applied to our particular problem, is given in the appendix of Ref. [1].

1.7 Experimental Results

This section presents all of the experimental data that were collected in the CSCX study. The section is organized in subsections which correspond to the diagnostic technique used to acquire the data. The primary goal of the experiments was to accurately measure the canting angle of the current sheet under a variety of initial conditions. Some of the diagnostics gave additional information about the thermodynamic state of the current sheet plasma (e.g., number density, temperature, etc.).

Each diagnostic was applied to eight different working propellants: hydrogen, deuterium, helium, neon, argon, krypton, xenon, and methane; three different initial gas pressures were used: 75, 200, and 400 mTorr. The pressure range was chosen to correspond to that of propulsive interest, that is, pressure levels which give propellant exhaust speeds in range of 10-100 km/s. To allow for direct comparisons between the various diagnostics, all quantitative work was done with PFN II charged to 9 kV.

In this section all measured quantities are plotted as functions of propellant species and pressure only. Undoubtedly, plotting the measurements as a function of other physical quantities would be more likely to expose parametric trends (e.g., plotting the current as a function of propellant atomic mass might give some insight as to how mass loading in the current sheet influences the current). However, such analysis is deferred to Section 1.15: Analysis and Modelling, since such interrogations of the data will be more meaningful if they are guided by trends suggested in the theoretical models. Limiting the scope of the analysis in this section allows it to serve as a more concise database of current sheet canting data. Furthermore, rather than cluttering the presentation with page-after-page of data, this section summarizes the results of each diagnostic in a few figures; support data are accumulated in the appendix of Ref. [1] where it may serve as a useful resource for other current sheet studies.

The uncertainty reported for all quantitative results includes the influence of both systematic and random errors. The confidence level for all graphical error bars and explicitly stated error values is 90%. Details of the procedures used to calculate the uncertainty in the experimental results are presented in the appendix of Ref. [1].

1.8 Circuit Current and Voltage Measurements

Before presenting the current sheet canting measurements, the two sections which follow describe the measured PFN/accelerator electrical circuit behavior.

1.8.1 Circuit Current

General circuit performance

The total current delivered to the accelerator was measured using a current transformer positioned between the accelerator and the last stage of the PFN.

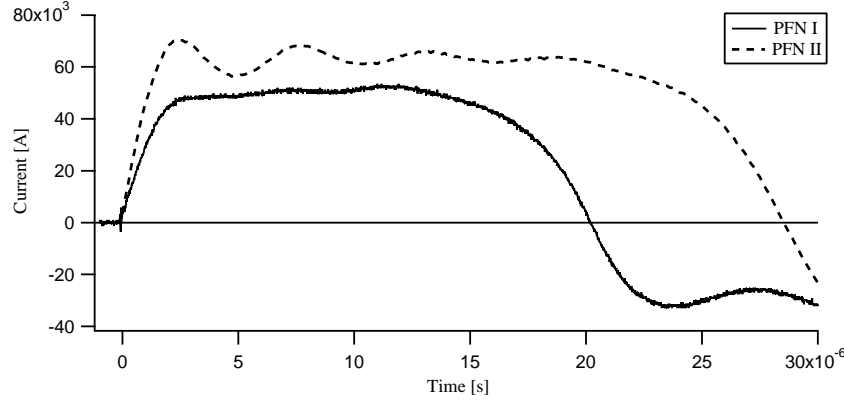


Figure 1.14: Experimental current waveforms (PFN I: 4.5 kV, Argon (100 mTorr), PFN II: 9.0 kV, Argon (200 mTorr).)

Details about the transformer are given in section 1.5. Typical current waveforms are shown in figure 1.14. In both cases the current pulse was followed by about two cycles of damped sinusoidal ringing.

Influence of gas species and pressure

Figure C.1 in the appendix of Ref. [1] shows the peak current, I_{\max} , and average current, \bar{I} (the average is taken over the 15 μsec which follow the peak current), attained for each propellant at initial pressures of approximately 75, 200, and 400 mTorr. The plotted points represent averages over about twenty tests.

Discussion

Comparison of figures 1.14 and A.3 of the appendix of Ref. [1] (the PFN numerical design simulations) indicates that both PFNs gave performance in qualitative agreement with their design (note that the simulations were for maximum design voltage whereas the experimental waveforms were recorded at slightly lower voltages). Differentiating the PFN II waveform yields an initial current rise-rate of approximately 10^{11} A/sec – in agreement with the design estimates.

PFN I's peak current and pulse-width showed closer agreement to its design waveform than did PFN II's. As is evident in figure 1.14, the PFN II current waveform seems to initially "overshoot" the desired "flat-top" current level; this overshoot leads to a damped oscillation that persists for most of the pulse. The overshoot most likely results from the use of a reduced-size initial stage inductor; the first-stage inductor was reduced in size in order to achieve the highest possible dL/dt . In PFN I, all of the inductors were identical. Again, comparing the calculated and experimental waveforms, the peak current attained by PFN II was slightly less than expected and the pulse width was slightly longer

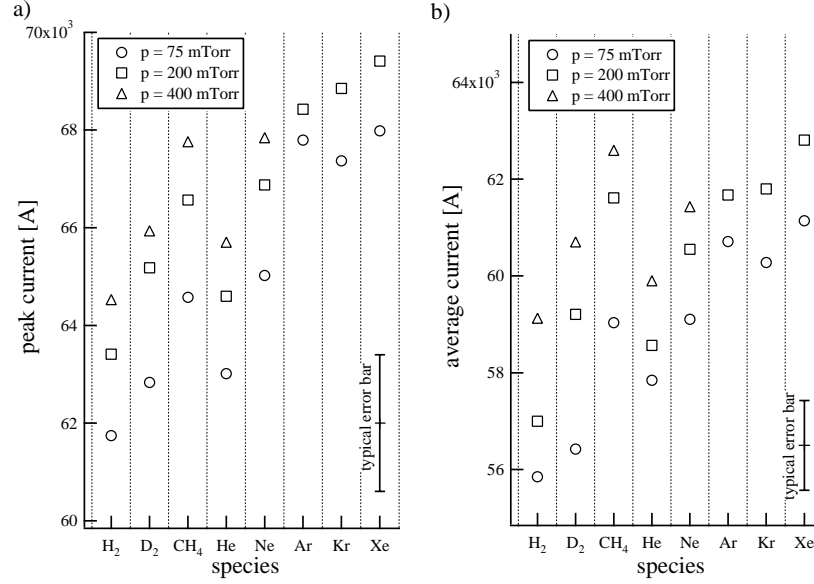


Figure 1.15: Influence of propellant species and pressure on a) peak current and b) average current.

than predicted. These three factors combined suggest that the actual PFN II inter-stage inductance was higher than the design value. Reflecting back on the physical construction (as shown schematically in Figure A.4 of the appendix of Ref. [1]), it is most likely that the extra inductance originates from the capacitor mounting scheme. The analysis called for 100 nH of inter-stage inductance; for the given copper plate width and separation (capacitor height), approximately four inches of inter-stage spacing was required to give 100 nH. PFN II was constructed with four inches of space between the capacitor cases, whereas the capacitor mounting terminals were spaced eight inches apart. The (unaccounted for) volume of the capacitor bodies is most likely the source of the extra inductance. In any event, the actual waveform, while somewhat different from the design, was adequate for the present study. Compared to PFN I, PFN II had a higher rise-rate, peak current, and pulse width – enabling tests to be run at higher pressure levels. The current sheet structures observed using PFN I were the same as those observed using PFN II, indicating that the slight ripple in the PFN II current waveform did not give rise to new phenomena.

The current measurements shown in figure C.1 of the appendix of Ref. [1] show two general trends: both peak and average currents increase with increasing pressure and atomic mass of the accelerated propellant. It should be noted that the molecular propellants experience a rapid increase in pressure (above the initial ambient fill) when they enter the current sheet – due to dissociation. It is more revealing to plot the current as a function of total propellant mass (total

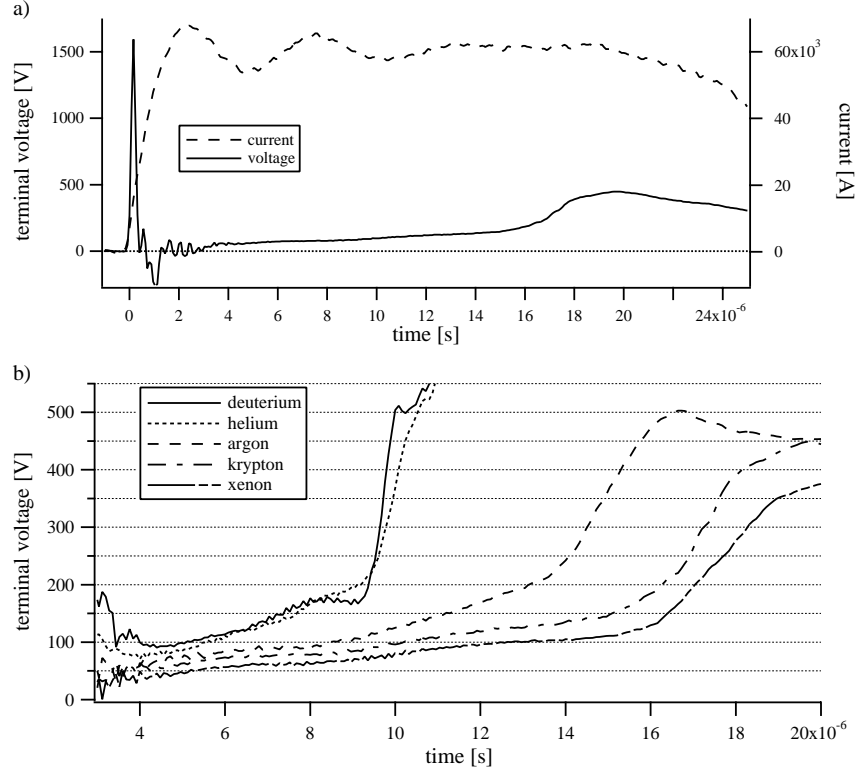


Figure 1.16: Terminal voltage measurements: a) terminal voltage and current from a krypton discharge, b) terminal voltage for several different propellants.

mass of propellant contained within the discharge chamber prior to firing), in which case we find that the current increases monotonically with increasing total propellant mass. This trend is shown in Fig. C.1 and the associated discussion, in the appendix of Ref. [1], concludes that the current variation with propellant mass is due to variation of the dynamic impedance.

1.8.2 Terminal voltage measurements

The terminal (muzzle) voltage was measured using the voltage divider described in section 1.6. The probe was attached at the center of the end of the electrodes (i.e., approximately 24 in. from the breech, and 3 in. from the outer edges of the electrodes). The goal of this experiment was to gain an estimate of the inter-electrode voltage drop associated with the plasma resistivity. Figure 1.16 shows the results from the measurements. The measurements were made with an initial background gas pressure of 75 mTorr. The plots represent the oscilloscope-averaged waveforms from five shots.

In Fig. 1.16a the voltage history for an entire discharge event in krypton is illustrated; the associated current waveform is included for reference. The figure shows that there is, as expected, an initial high voltage spike associated with the gas breakdown process, after which there are somewhat erratic oscillations (for about the first $3 \mu\text{s}$) including an excursion into negative voltage. After this initial transient region, the voltage monotonically increases (fairly linearly) up to about $t = 15 \mu\text{s}$, after which the voltage increases more rapidly, reaches a maximum, and then falls off. Figure 1.16b shows similar plots for other propellants; however, only the post-transient region is plotted so that the scale of the vertical axis could be adjusted to provide greater resolution of the regions of most interest.

Discussion

The voltage waveforms can be divided into three regions: initial transient, current sheet propagation, and blowing regions.

The transient region extends from about $t = 0 - 3 \mu\text{s}$. Any interpretation of this portion of the waveform is dubious because the high dI/dt associated with the initial transient can induce (inductive) voltages in the probe circuitry which are not associated with the plasma resistivity. For example, since the magnetic field extends in front of the current sheet in the present experiment, although the magnetic field itself is expected to be fairly weak ($< 10^{-2} \text{ T}$), dB/dt may be quite large. Since the flux surface defined by the probe, electrode, and current sheet loop is large, it is possible for non-ohmic voltage drops to be induced during times of high dI/dt .

The propagation region is defined by the time it takes for the current sheet to traverse the length of the electrodes, which of course varies from propellant to propellant. The time of arrival of the current sheet to the end of the electrodes is indicated in the figures by the time at which the voltage begins to rapidly increase. At this point in time, the voltage probe not only is exposed to the resistive voltage drop, but also the inductive voltage drop, which is confined behind the current sheet. In the deuterium and helium discharges, this transition is most abrupt – occurring at approximately $9.5 \mu\text{s}$. For argon the transition occurs at approximately $14 \mu\text{s}$ and at approximately $16 \mu\text{s}$ for both krypton and xenon. Within the propagation region the voltage drop is found to vary from about 50-250 V, depending on the propellant. Using the current data from the previous section, the total plasma Ohmic resistance is estimated to be 1-5 m Ω .

There are several interesting features observed in the propagation region. First, a rough estimate of the current sheet propagation speed can be found by dividing the length of the electrodes (60 cm) by the time for the current sheet to reach the propagation-blowing transition. For deuterium and helium this analysis yields a speed of about 6.3 cm/ μs ; similarly, for argon, 4.3 cm/ μs , and 3.8 cm/ μs for both krypton and xenon. These values will be seen to agree well with results obtained using more advanced speed measurement techniques, as presented in subsequent subsections of this section.

Next, it is apparent that the inter-electrode voltage increases, for all of the

propellants, as the current sheet propagates. For example, the terminal voltage in the xenon current sheet increases from about 50 to 100 V during propagation. Recall, again, that the muzzle voltage should have no contribution from the inductive voltage drop associated with the propagation of the current sheet[16]. One possible explanation for the progressively increasing voltage is that the current sheet cools as it propagates, causing the plasma resistivity to increase. Another possible explanation for this trend is acceleration of the current sheet; in other words, the rate at which conduction electrons experience inelastic collisions (e.g. ionization) may be related to the instantaneous speed of the current sheet. As the speed increases, the current sheet must ingest and ionize neutral atoms at a progressively increasing rate; this would be reflected in a requisite increase in the total energy budget (voltage drop).

Along the same line of reasoning, another trend in the data might be explained. It is seen in Fig. 1.16b that the voltage drop at any instant of time increases as the atomic mass of the propellant decreases (note that helium and deuterium have about the same mass). Again, this could be explained by the fact that the current sheet moves faster in the lighter propellants, and thus has a higher internal rate of inelastic collisions. This reasoning is complicated by variations in ionization potential amongst the various propellants. However, this explanation is supported by the helium and D₂. In addition to having the same mass, helium and D₂ require about the same total amount of energy to singly ionize. The plots show that their voltage histories track very closely.

The terminal voltage data also show possible evidence of current sheet canting. With a canted current sheet one of the electrode current sheet attachments would arrive at the end of the accelerator before the other electrode attachment; consequently, we might expect that an uncanted current sheet current sheet would produce a sharp propagation-blowing region transition in the terminal voltage measurement whereas the transition would appear more gradual with a canted current sheet. In this framework, the data in Fig. 1.16b would indicate that the helium and deuterium current sheets are less canted than the heavier propellant current sheets. Alternatively, the differences in the voltage increase rate could be related to differences, from propellant to propellant, in the current pattern transformation from propagation to blowing mode (see Eckbreth[13]).

After the current sheet reaches the end of the electrodes (both the anode and cathode attachments), the arc is expected to go into a "blowing" mode; the arc will balloon out into the chamber with attachments anchored to the ends of the electrodes. As the current begins to fall off, a "crowbar" arc is expected to form at the breech and short-circuit the initial current sheet, leaving its plasma to dissipate.

1.9 High-speed photography

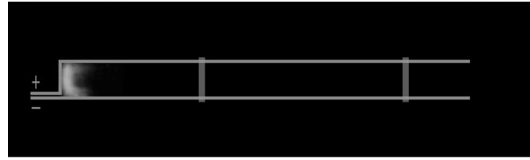
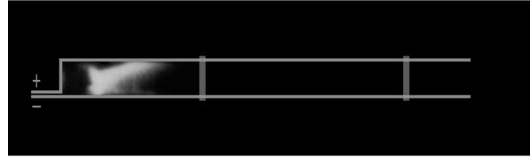
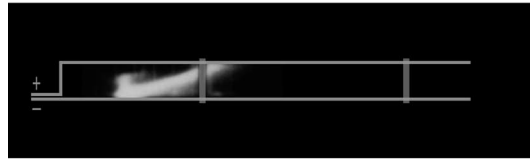
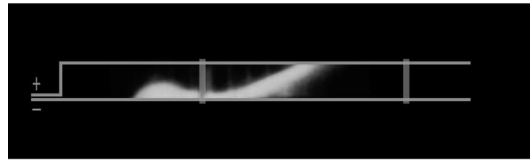
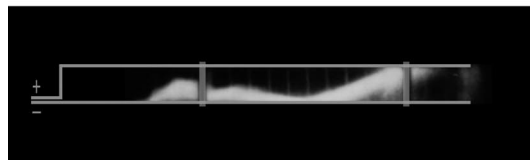
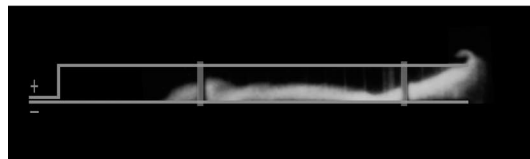
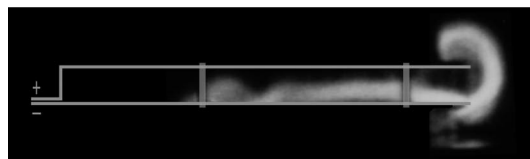
High-speed photography (see section 1.6.1) was initially used to obtain images of the macroscopic evolution of the discharge. This diagnostic was especially important because it established that the accelerator was functioning as a con-

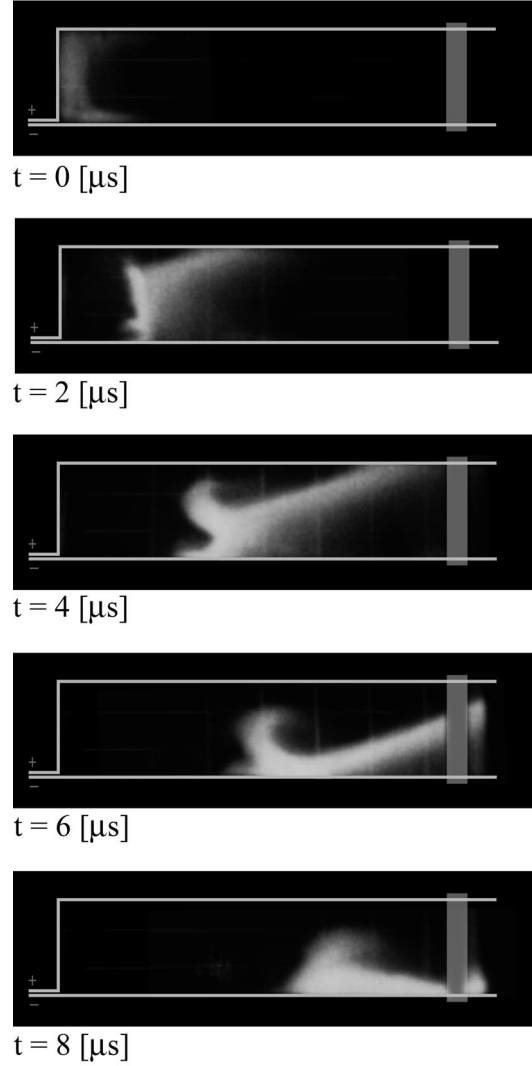
ventional pulsed plasma accelerator – a current sheet was seen to form at the breech and propagate between the plates and eject from the end of the electrodes. Later, the diagnostic was used to provide a first, rough, quantitative estimate of the current sheet propagation speed and canting angle. The two sections which follow present a photographic survey of the discharge evolution and canting. Other pertinent photographs which show, for example, the influence of electrode polarity and contamination, are given in the appendix of Ref. [1].

1.9.1 Evolution of the discharge

The Imacon camera was used to obtain spatially and temporally resolved images of a single discharge event; the interframe delay of the Imacon was set to $2\ \mu\text{s}$ (500 ns exposure). When the camera trigger was offset from the initiation of the discharge by $1\ \mu\text{s}$, the good reproducibility of the discharge structure allowed two separate runs to be interleaved to give a succession of images that show the complete discharge event in $1\ \mu\text{s}$ intervals.

Figure 1.17 (series I) shows photographs of a discharge for several successive times during a single pulse (the times shown correspond to those in the current waveform of Fig. 1.14 (PFN I). The Polaroid images were scanned into a computer and processed with photo-editing software. Lines were drawn to indicate the position of the electrodes. The two vertical rectangles on the electrodes represent bolts that are used to hold the accelerator together; they caused an optical obstruction between the plasma and the camera. The top electrode is the anode. The propellant used was argon at 100 mTorr and the capacitor bank voltage was set to 4 kV. A narrow-pass line filter (488 nm, 10 nm FWHM) was used to allow only the light emitted by argon ions to enter the camera; this was done to exclude the more spatially diffuse glow of the neutrals, and enhance the contrast in the regions where current was flowing. The photographs show that the discharge forms at the breech, accelerates down the electrodes, and is ejected from the exit. Immediately after the current sheet leaves the breech it begins to tilt — with the anode attachment leading that of the cathode. The sheet then stabilizes to a fairly fixed angle, leaving a trail of plasma along the cathode in its wake, while it propagates down the rest of the discharge channel. Since the anode arc attachment reaches the end of the accelerator first, the ejection of the plasma is quite asymmetric; the current sheet is forced to curl back on itself to re-attach at the anode. The discharge propagates 60 cm in approximately $15\ \mu\text{s}$ implying an average sheet speed of about $4\ \text{cm}/\mu\text{s}$.

 $t = 0 \mu\text{s}$  $t = 3 \mu\text{s}$  $t = 6 \mu\text{s}$  $t = 9 \mu\text{s}$  $t = 12 \mu\text{s}$  $t = 15 \mu\text{s}$  $t = 18 \mu\text{s}$ Series I



Series II

Figure 1.17: **Series I:** Series of photographs showing the evolution of the discharge in a single pulse ($p=100$ mTorr (argon), $V = 4$ kV). **Series II:** Series of photographs showing the evolution of the discharge near the breech ($p=100$ mTorr (Argon), $V=5$ kV).

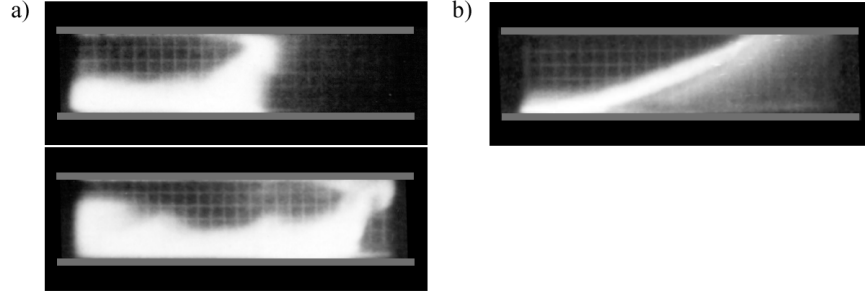


Figure 1.18: High-speed photographs of current sheets at the midsection of the CSCX accelerator: a) example of two successive photographs used in the determination of propagation speed (helium (400 mTorr), $\Delta t = 2 \mu\text{sec}$ between frames), b) example of a photograph used to determine canting angle (xenon (75 mTorr)).

Figure 1.17 (series II) shows a close-up of the breech region of the accelerator. The initial conditions for the accelerator in this set of photographs were the same as those used in series I, with the exception that the bank voltage was 5 kV instead of 4 kV. This figure more clearly shows the transition of the arc from its planar initial state, to the fully canted current sheet. As the current sheet leaves the back of the accelerator, it immediately begins to bifurcate. The initial anode attachment point recedes from the electrode, and a diagonal sheet forms. Within several microseconds the sheet attains the canted structure that it maintains for the remainder of its propagation. The base of the arc (cathode attachment) forms a hook-like structure which has been previously reported in earlier studies (see the review in Ref. [1]).

Additional accelerator breech and midsection photographs (in which different propellants were used) are given in the appendix of Ref. [1].

1.9.2 Speed and canting-angle measurements

Photographs were taken of the mid-section of the accelerator (using PFN II), with the camera in position 2 (see Fig. 1.6). Seven different propellants were tested at up to three pressure levels (75, 200, and 400 mTorr). Higher atomic mass propellants (e.g., xenon) were not photographed at 400 mTorr because the current pulse was not of sufficient duration to drive the discharge into the viewing region at higher propellant mass loadings. The goal of this set of photographic experiments was to get a rough idea of the current sheet propagation speed and canting angle.

Figure 1.18 shows examples of the photographs obtained in the study. For clarity, lines representing the position of the electrodes (anode on top) have been drawn on the images. Also, a gridded background outside of the accelerator is visible (the grid spacing was 1 cm). In the pictures the current sheet is moving from left to right. The right-most visible feature, which spans the entire gap

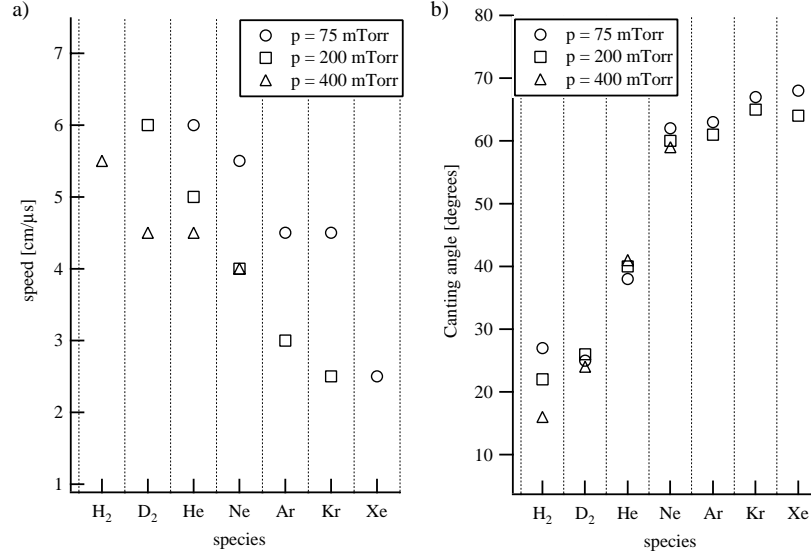


Figure 1.19: Current sheet a) propagation speed and b) canting angle, interpreted from high-speed photographs (no error bar is included because of the inherent subjectivity in the measurement technique).

between the electrodes, is assumed to be the current sheet. Also, a luminous cloud is seen to trail behind the current sheet; we assume that this is not part of the current conduction zone but, rather, gas that has been heated by the current sheet. Figure 1.18a shows two images from a helium discharge, taken 2 μ sec apart. By measuring the change in spatial position of the sheet between the two frames, the propagation speed was estimated. Figure 1.18b shows a single frame from a xenon discharge. By measuring the slope of the luminous front, the canting angle was estimated. Figure 1.19 summarizes the measurements obtained from all of the photographs (additional photographs that were used to create Fig. 1.19 are given in the appendix of Ref. [1]).

1.9.3 Discussion

Each point in Fig. 1.19 was distilled from two photographs. In some cases the images were difficult to interpret (for example, the high speed of the hydrogen current sheets caused the images to be blurred); those cases are not included in the graphs. The diagnostic technique is not well suited for precise measurements because interpretation of the photographs relies on the assumption that the luminosity patterns correspond to the spatial location of the current. This assumption may not be valid if the luminous regions are caused by other phenomena, such as shock waves. No meaningful error analysis can be carried out on the plotted values because of the small number of samples as well as the

inherent subjectivity in the interpretation of the luminosity patterns.

In any event, some qualitative trends can be gleaned from the results. First, the higher atomic weight propellant cases had slower moving current sheets, which is what one would expect from mass loading considerations. Second, it is apparent that the higher atomic mass propellants had a higher degree of current sheet canting – with xenon having almost 40° more tilt than hydrogen. Hydrogen at high pressure exhibited the lowest canting angle; no correlation between canting angle and pressure can be made for the other propellants, since the uncertainty in this measurement technique is large.

The luminous region which trails behind the current sheet, along the cathode, was present in all of the photographs obtained in this study. This observation, along with additional data presented in subsequent subsections of this section, will later be used to support conclusions reached in the CSCX study about current conduction and the effectiveness of current sheets in sweeping up propellant.

1.10 Schlieren imaging

Despite the implementation of several different optical configurations and lasers, only a very limited amount of data was obtained using schlieren imaging. The suspected problem with our systems will be discussed after a brief summary of the results from each optical arrangement.

1.10.1 Schlieren photography configuration

Schlieren photographs were acquired near the breech and center of the accelerator using the apparatus described in section 1.6.2. However, after repeated attempts, the schlieren photography configuration yielded no resolvable features in the discharges.

1.10.2 Shadowgraph configuration

Slightly better results were obtained using the shadowgraph configuration. Figure 1.20a shows an image obtained near the midsection of the accelerator. A faint image of the current sheet is visible along the bottom electrode (cathode). The direction of current sheet motion was from left to right. As was observed in the photographic study, the shadowgraph image indicates that the current sheet is highly canted, and a trailing plasma tail can be seen in the lower left corner. However, this image is too faint and small in spatial extent to provide any useful quantitative information.

1.10.3 Modified shadowgraph configurations

Both modified shadowgraph configurations illustrated in Fig. 1.9 were implemented. Use of the aperture mask yielded an image very similar to the image in

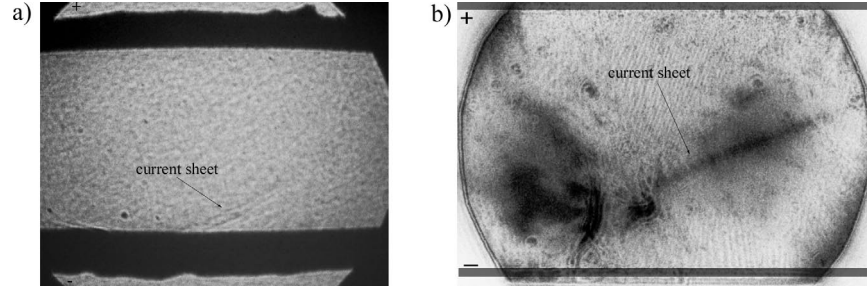


Figure 1.20: a) Shadowgraph image of current sheet near bottom electrode and b) modified shadowgraph image of current sheet near the breech (Argon, 100mTorr, $V = 4\text{kV}$).

Fig. 1.20a but much darker (better contrast). The spatial extent of the image, however, was no greater than that obtained using the standard shadowgraph technique.

Figure 1.20b shows a modified shadowgraph image that was acquired using the dot mask. The contrast of the image has been reversed to better clarify the structure. In this image we begin to see features reminiscent of the photographic survey. In particular, the image was acquired near the same spatial position and at about the same time as the image in Fig. 1.18 (series II) labelled $t = 4\ \mu\text{s}$. In both of these images we see that a sharp, linear structure emanates from a more diffuse, blob-like structure near the cathode. The canting angle in the modified shadowgraph image is severe – approximately sixty degrees. This agrees with the data in Fig. 1.19 from the high-speed photography experiment.

1.10.4 Discussion

It still remains to discuss the reason why schlieren imaging was not fruitful in this experiment. The most likely culprit was the “smearing out” of the images by light emitted from the plasma. In the shadowgraph configuration, maximum contrast is obtained when the imaging screen is placed near the refractive medium[19] (the current sheet, in the present case). However, when the screen was placed near the CSCX accelerator, the optical emission from the plasma was sufficient to saturate the CCD camera. This was quite remarkable considering that the camera lens was covered with a 532 nm laser line filter, and no line radiation was expected to be emitted within the bandpass of the filter. This implies that the camera saturation occurred due to time-integrated (the slow mechanical shutter allowed light to be collected during the entire current pulse) exposure to broadband radiation. When the imaging screen was moved far away from the accelerator, the exposure due to plasma emission was significantly reduced, however, the contrast due to the shadow effect was lost.

On the other hand, the contrast of the conventional schlieren system is actually enhanced when the imaging plane is far from the refractive medium.

Unfortunately, most of the laser light is lost in the preparation of the schlieren image source (see section 1.6.2); also, the optical system is set up to image the discharge chamber and, consequently, the optics efficiently transmit the plasma emission to the imaging plane. These two factors combined to, again, create a situation where the total amount of laser light and plasma radiation collected were comparable.

The most likely solution to the problems detailed above would be to use an electro-optically gated CCD camera. Such a camera could be gated to about 10 ns and, hence, would collect all of the laser light and only a very small fraction of the light emitted by the plasma.

1.11 Magnetic field probes

1.11.1 Database of canting angles

In order to obtain a more accurate measurement of the current sheet speed and canting angle, two magnetic field probes were introduced into the accelerator channel as illustrated in Fig. 1.10c. Probe set I was used and all measurements were obtained near the midpoint (30 cm) of the accelerator. The same propellants and pressure levels that were used in the photographic study were tested.

Figure 1.21 shows a typical set of data with hydrogen as a propellant. A more extensive set of data for all of the propellants is given in the appendix of Ref. [1]. The data plotted in Fig. 1.21a were acquired with the B-dot probes aligned in configuration 1 (see Fig. 1.10); the probes were axially (note: the axial direction is the direction of the thrust axis, or the $+\hat{x}$ direction, as illustrated in Fig. 1.15.2) separated by 21 cm. We see that, as the current sheet approaches a probe, the magnetic field in front of the sheet is gradually detected; then, as the probe enters the current sheet, the magnetic field quickly reverses direction. When the current sheet has passed the probe, the magnetic field reaches its peak value and remains fairly constant (~ 0.35 Tesla) until the current reverses. The peak value of the magnetic field near the mid-section of the accelerator for all of the propellants tested is shown in Fig. 1.21c.

Data, such as that shown in Fig. 1.21a, was used to estimate (using the time-of-flight technique) the current sheet propagation speed by measuring the time delay between a common feature on each waveform (the point at which the magnetic field reached 0.1 T on each waveform was used as the reference point throughout this study). Similarly, Fig. 1.21b shows data from B-dot probes aligned in configuration 2; the probes were vertically separated by 3 cm. By measuring the time delay between the arrival time of the current sheet to each probe and, knowing the propagation speed of the current sheet, the canting angle was estimated. Figure 1.22 summarizes all of the speed and canting angle measurements obtained using the magnetic field probes and time-of-flight analysis. Each datum point represents the average of two experimental measurements. The random error associated with having only two samples is large,

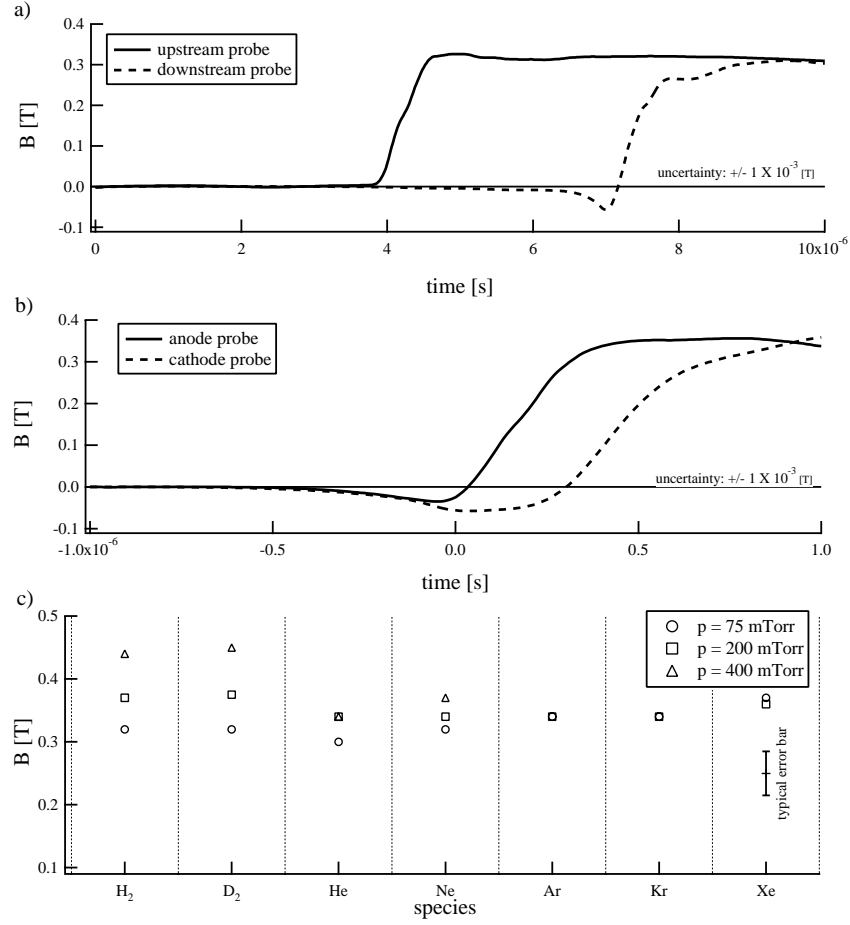


Figure 1.21: Magnetic field measurements using B-dot probes for time-of-flight canting angle analysis in a) configuration 1 and b) configuration 2 (Hydrogen, 75 mTorr.) In c) the peak magnetic field at the accelerator mid-section is plotted.

and is reflected in the large error bars.

1.11.2 Evolution of the canting angle

In addition to quantifying the canting angle at one axial location, a magnetic field probe study was conducted to reveal how the canting angle evolved as the current sheet propagated down the electrodes. Probe set II was used in configuration II with the probes vertically displaced by 4 cm (see Fig. 1.10). Data were acquired at about forty different axial locations. Only argon propellant (75 mTorr) was used in this study.

Figure 1.23a shows the measured current sheet arrival time at each of the

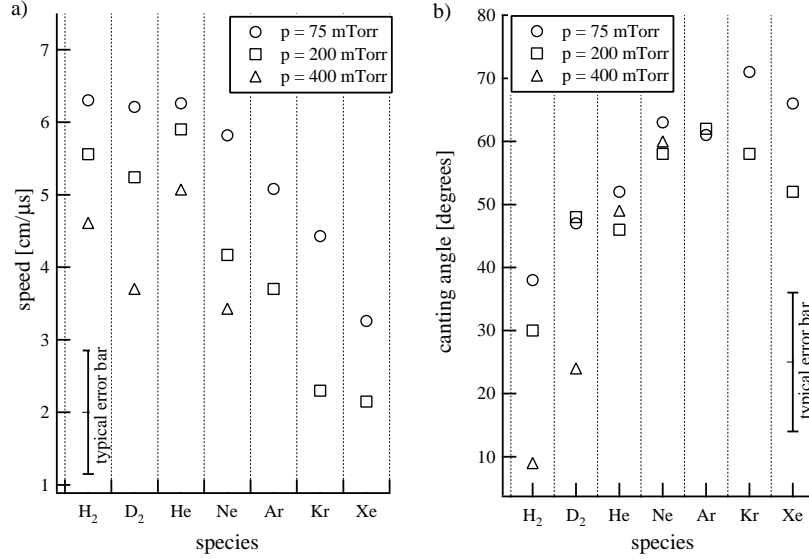


Figure 1.22: Current sheet a) propagation speed and b) canting angle, interpreted from magnetic field probe data.

axial probe locations for both the anode and cathode probes. Each datum point represents the average of four shots. Polynomial curve fits (fifth order) to the datum are also shown. By taking the average of the of the anode and cathode curves, the trajectory of the geometric center of the current sheet can be constructed. Taking the time-derivative of the trajectory yields the current sheet speed profile, as illustrated in Fig. 1.23b. Similarly, the evolution of the canting angle can be constructed by comparing the anode probe position curve with the cathode probe position at fixed times; figure 1.23c shows the results of such an analysis.

Figure 1.24 shows the evolution of the magnetic field at several axial locations, for both the anode and cathode probe. Each waveform is the record from a single shot.

1.11.3 Discussion

The expected peak value of the magnetic field may be estimated using the parallel plate transmission line inductance formulas given in the appendix of Ref. [1]. Since the surface area of the flux loop increases as the current sheet propagates, the magnetic field is expected to decrease with axial distance from the breech. At the center of the accelerator (30 cm), using $L=90$ nH, $I=60$ kA, the dimensions of the accelerator and the definition of inductance, the magnetic field is estimated to be 0.36 T, which is consistent with the data plotted in Fig. 1.21c. The magnetic field in the immediate vicinity of the breech was measured

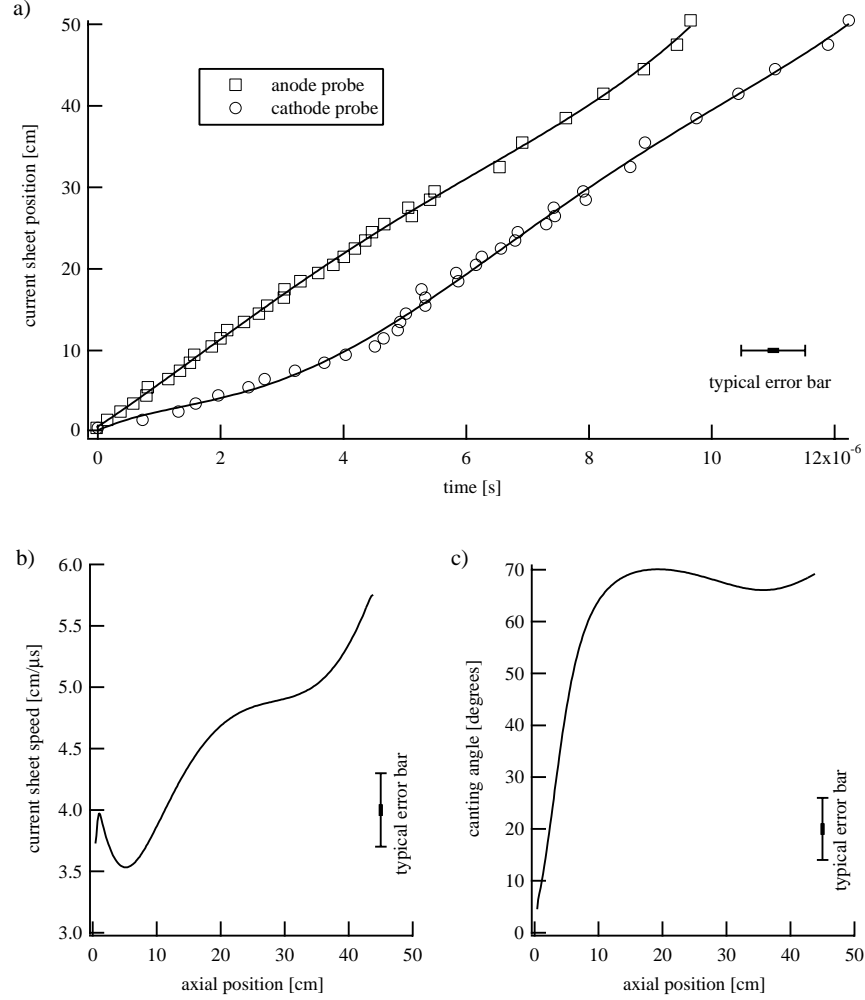


Figure 1.23: Evolution of current sheet canting interpreted from magnetic field probe data (argon, 75 mTorr): a) trajectory of anode and cathode current sheet attachment, b) current sheet speed as a function of axial position, c) current sheet canting angle as a function of axial position.

to be about 0.7 T.

The trends found in the photographic data are also evident in the magnetic field data: the speed of the current sheet decreases with increased mass loading and, in general, the current sheet canting is more severe for the higher atomic mass propellants. Comparison of the numerical values in both plots show sporadic quantitative agreement. The canting angles for hydrogen and deuterium (at 75 and 200 mTorr) and helium were found to be substantially

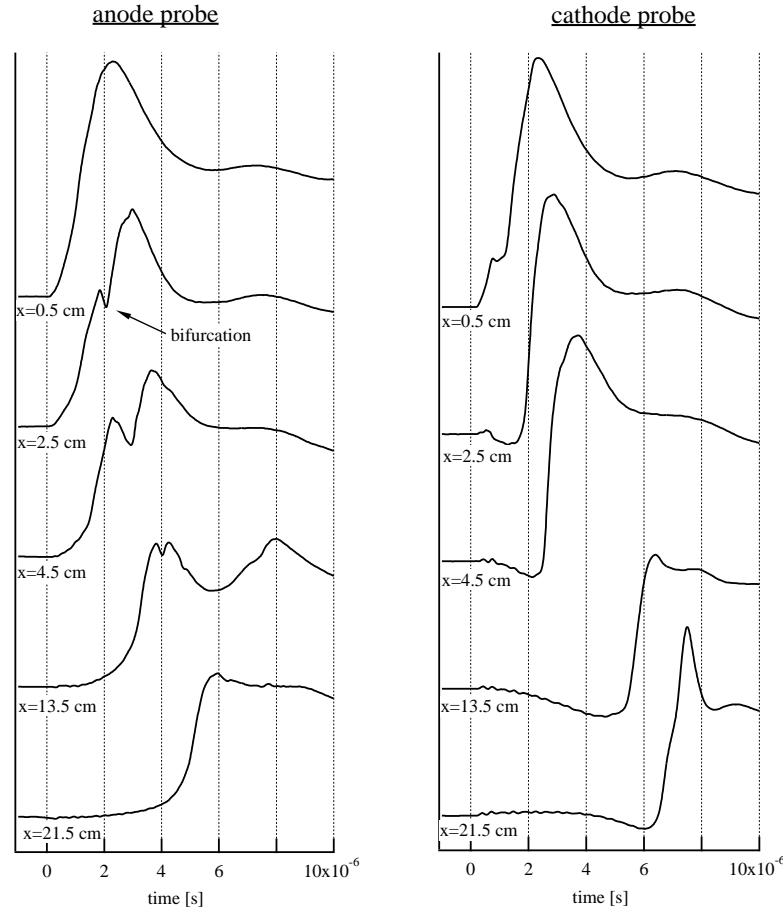


Figure 1.24: Magnetic field histories at selected axial locations (argon, $p=75$ mTorr). For reference, the peak value of the magnetic field for both the anode and cathode probes were measured to be about 0.7 T at the $x=0.5$ cm location.

larger than those measured in the photographic study – which underpins the comments made earlier about the difficulty of interpreting photographic data. The magnetic field data did reinforce, however, that the lowest canting angles are achieved with hydrogen and deuterium at 400 mTorr.

The canting evolution data show that current sheet canting is not a continuously evolving phenomenon but, rather, the degree of canting is set up in about the first ten centimeters, after which the current sheet maintains a fairly constant canting angle. The plot in Fig. 1.23c indicates a canting angle of about 60° - 70° near the midsection of the accelerator (30 cm), which agrees with the data presented in Fig. 1.21b. Also, Fig. 1.23b indicates a current sheet speed of about 4.5-5.0 cm/ μ s at the midsection, in agreement with the data presented

earlier. Figure 1.23b also shows that the current sheet slows during the early stages of the discharge, but then accelerates as it propagates down the electrodes.

The data in Fig. 1.24 provide some insight into the sequence of events which cause the current sheet to cant during the early stages of the discharge. The plots show very different behavior for the anode current conduction as compared to the cathode attachment. The $x=0.5$ cm curves look very similar; however, a double-peaked structure is evident in the $x=2.5$ cm anode waveform which is not present in the corresponding cathode trace. The two peaks in the anode data imply the presence of two current conduction paths – bifurcation of the initial current sheet. In the $x=4.5$ cm data the bifurcation is seen to be more pronounced. As the current sheet continues to propagate, the two current attachments spread apart and the leading sheet becomes the dominant current conduction channel (as illustrated by the $x=13.5$ cm data). By the time the current sheet reaches the 21.5 cm location the trailing (initial) current sheet is seen to have disappeared altogether, and the discharge returns to a single current conduction channel mode of operation. The important point here is that no comparable (bifurcation) features are present in the cathode magnetic field waveforms. An interpretation of this experimental observation will be given in section 1.15.2, where it is proposed that bifurcation is the beginning of a process that leads to a canted current sheet.

1.12 Laser interferometry

The final diagnostic technique implemented to measure the current sheet speed and canting angle was a two-chord laser interferometer (see Fig. 1.11). In addition to the propellants described in the preceding sections, methane was tested. The interferometry experiment was carried out in a manner completely analogous to the magnetic field measurement experiment: two axially separated laser beams (configuration 1) were used to measure the current sheet speed and two vertically separated beams (configuration 2) were used to measure the canting angle.

Figure 1.25 shows examples of electron density measurements acquired with the interferometer using argon propellant. A more extensive set of data for all of the propellants is given in the appendix of Ref. [1]. Figure 1.25a shows a typical result using the interferometer in configuration 1. In this case the laser beams were axially separated by about 11 cm. It is seen that the time delay between the two signals was about $2.5 \mu s$ – indicating a propagation speed of about $4.5 \text{ cm}/\mu s$. Also, this figure indicates that the electron density decreased as the current sheet propagated between the upstream and downstream beams.

Figure 1.25b shows a typical result using the interferometer in configuration 2 (4 cm vertical beam separation), with the same initial propellant loading as in Fig. 1.25a. The anode signal is seen to arrive about $1.5 \mu s$ before the cathode signal, in agreement with our previous observations that the anode current sheet

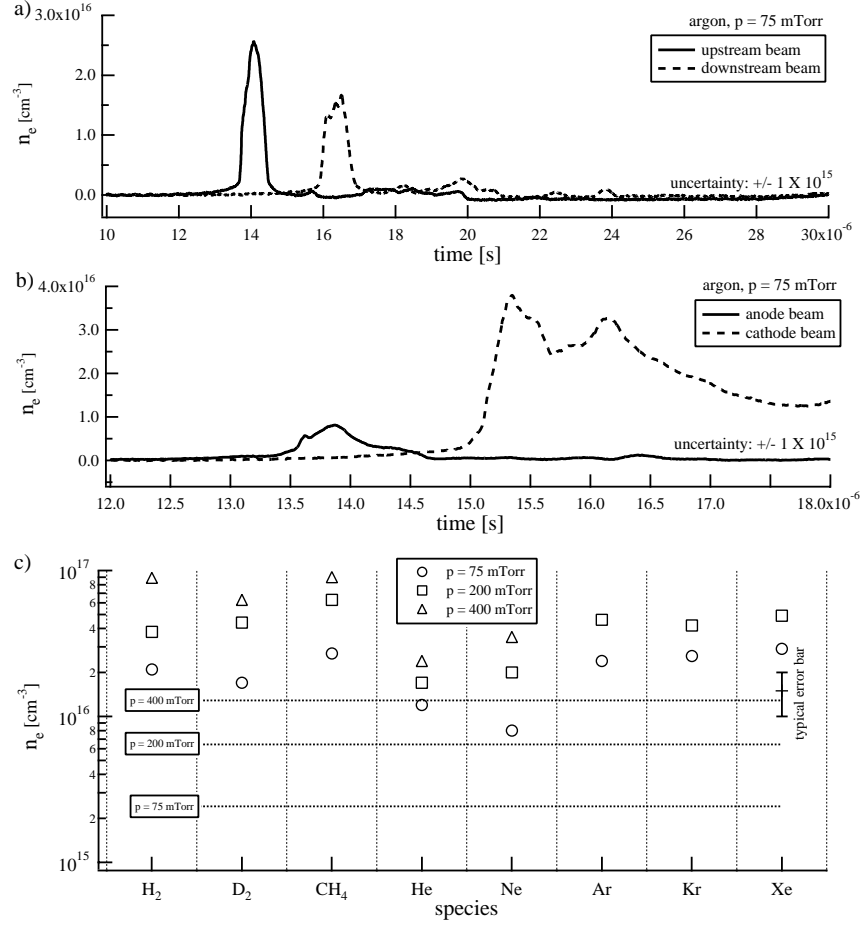


Figure 1.25: Example electron density profiles for laser beams aligned in a) configuration 1 and b) configuration 2 (argon, $p = 75$ mTorr). The peak electron density at the accelerator midsection, for each of the propellants tested, is plotted in c).

attachment leads the cathode attachment. Multiplying the anode-cathode time delay by $11 \text{ cm}/\mu\text{s}$ (the sheet propagation speed), yields an axial anode-cathode arc attachment separation of about 7 cm, so that the canting angle may be estimated to be about 60° . Another readily apparent feature in Fig. 1.25b is the large disparity in electron density near the cathode as compared to near the anode. Also, the cathode trace indicates that a layer of plasma persists along the cathode long after the current sheet has passed by.

Figure 1.25c shows a summary of the peak electron density at the accelerator midsection for all of the propellants tested. The plotted values were compiled

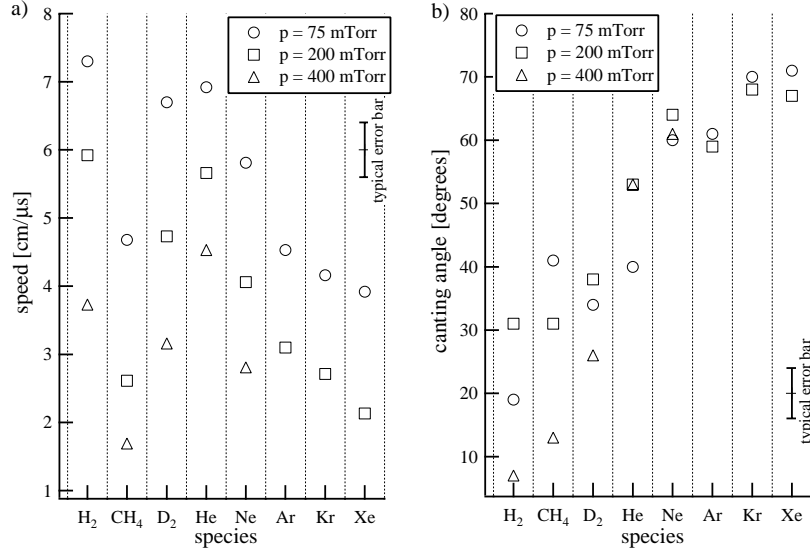


Figure 1.26: Current sheet a) propagation speed and b) canting angle, interpreted from interferometric data.

from data obtained using the upstream probe in configuration 1. For reference, horizontal lines have been added to indicate the initial propellant fill number density for the specified initial pressure levels. Additional data for the current sheet widths and electron density gradients are given in the appendix of Ref. [1]: typical values are 1 cm and $5 \times 10^{16} \text{ cm}^{-4}$, respectively.

Figure 1.26 summarizes the speed and canting angle measurements from the interferometric diagnostic and time-of-flight analysis. Each datum point is the result of ten experimental measurements and, hence, has a smaller error bar than in the magnetic field experiment.

1.12.1 Discussion

The interferometry diagnostic was very successful in providing quantitative measurements of the current sheet electron density, speed and canting angle. The measured electron densities were up to an order of magnitude higher than the initial fill density indicating either local compression of the propellant, entrainment of propellant in the current sheet, or higher level ($Z > 1$) ionization. The latter possibility is excluded in the next section (which presents the spectroscopic results) where it is shown that singly ionized species are the most prevalent ions.

In many cases the high electron density near the cathode caused phase variations which exceeded the frequency response of the interferometric system. While this did not effect the calculation of the current sheet speed and cant-

ing angle, it did make an accurate measurement of the electron density near the cathode impossible in some situations. These cases are more completely discussed in the appendix of Ref. [1].

Comparison of the data in Figs. 1.22 and 1.26 shows, within the bounds of the given error bars, that all of the major trends discussed in the interpretation of the magnetic field data are also borne out by the interferometric data. Also, methane (which is largely composed of hydrogen (CH_4)) exhibits the same peculiar tendency as hydrogen and deuterium – reduced canting at higher pressure. The analysis of the photographic data, however, gave significantly different estimates of the canting angle for the lower molecular mass propellants. Evidently, some of the luminous regions in the photographs are not zones of current flow but originate from other processes.

1.13 Emission spectroscopy

Both time-integrated and time-resolved spectral data were acquired. The time-integrated surveys were intended to determine the species present in the CSCX arc discharges, while the time-resolved data were aimed at providing an estimate of the electron temperature in the current sheet.

1.13.1 Survey of spectral lines

The acquisition of time-integrated data yielded a broad (wavelength) spectral survey of the plasma optical emission in order to identify candidate lines for the more detailed time-resolved experiments. The emission was surveyed by scanning the spectrometer between 350-850 nm (in 10 nm increments) with the spectrometer aligned in configuration 1 (see Fig. 1.13.) The camera was gated for about 1 ms exposure; therefore, emission from the entire duration of each discharge event was recorded. The capacitor bank was charged to 3 kV before each shot; this reduced voltage was used in the survey study in order to reduce, in light of the large number of required shots, the “wear and tear” on PFN II.

The sequences of about fifty frames of spectral data (for each propellant) were “pasted” together and calibrated using the software described in section 1.6.5. An example of a complete data set, using neon propellant, is shown in Fig. 1.27; the concentration of lines around 6000 Å reflects the characteristic red glow of low pressure neon discharges. In addition to plots of data for the other propellants, the appendix of Ref. [1] presents tabular data which identifies the atomic species associated with each emission line. The table shows that the emission spectra from all of the propellants can be characterized as line radiation of neutral and singly ionized species.

Another noteworthy result from the spectral survey was that no copper emission lines were observed (there are many tabulated copper neutral and ion transitions in the region surveyed[22]). This is most evident in the hydrogen survey graph (see Fig. C.18a of the appendix of Ref. [1]), where only the H_α and H_β lines were observed. This implies that there was no appreciable contamination

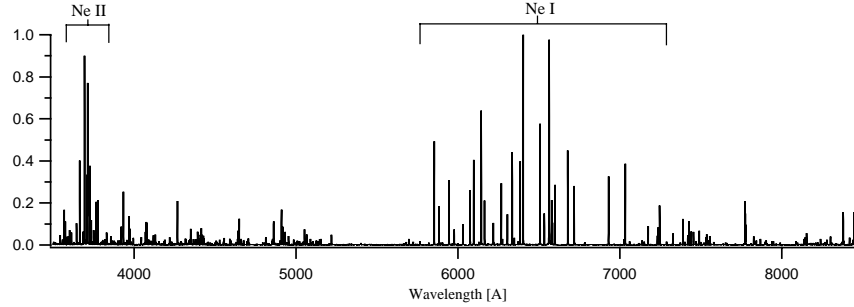


Figure 1.27: Normalized intensity of time-integrated optical emission from a neon arc discharge in the CSCX accelerator ($p=75$ mTorr).

of the propellant (at least in the central region of the accelerator) due to electrode erosion. We make this assertion cautiously, though. Other researchers[24] have observed that significant concentrations of copper electrode material can migrate into arc discharges without producing significant *optical* emission. The low ionization potential of copper allows ablated electrode material to rapidly reach high levels of ionization, where bound-bound electronic transitions result in the production of radiation in the *vacuum ultraviolet*, which cannot be detected with our instrument. Therefore, we cannot completely rule out the presence of electrode material in our discharges.

1.13.2 Time-resolved spectra and temperature determination

Argon was chosen for more detailed, time-resolved analysis. Eight lines were acquired with the spectrometer in configuration 2 (see Fig. 1.13). The camera was gated to 50 ns exposure-time. The spatial position of the light collection was chosen to roughly correspond to the position where the previous magnetic and interferometric data were acquired. Based on the current sheet speed measurements observed in those previous experiments, current sheet motion was expected to be restricted to less than a few millimeters during the CCD array exposure. The PFN II voltage was set to 9 kV and the propellant pressure was 75 mTorr for all shots.

The procedure for determining the electron temperature involved the construction of a “Boltzmann plot” and fitting a straight line to the experimental datum points; this procedure is described in detail in the appendix of Ref. [1]. Figure 1.28a shows the argon emission data and a linear fit through the points; each of the plotted points is the average of data collected from five different shots. It is apparent that the experimental data do indeed follow a linear trend. This is especially important because it implies that the free electrons in the arc plasma were indeed in a Maxwellian distribution of speeds, which is essential if we are to use the relative line ratio technique to infer electron temperature. The

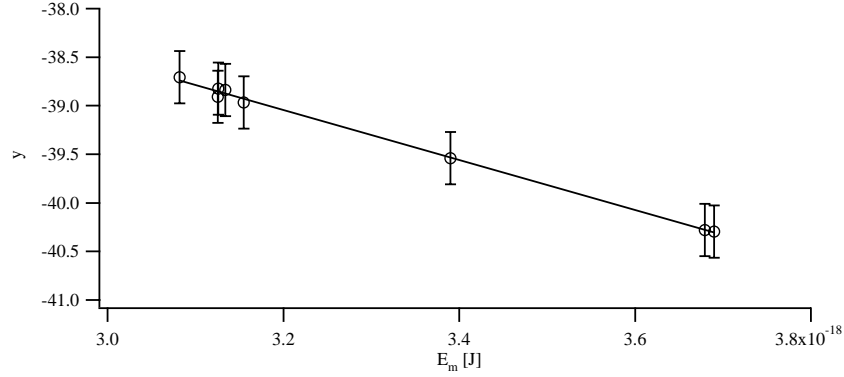


Figure 1.28: Temperature data: weighted dimensionless spectral emission intensity (y) versus energy of upper state (E_m) (argon, $p = 75$ mTorr).

uncertainty indicated by the error bar for each point is primarily due to random uncertainty in the intensity data. In the case illustrated above, the calculated electron temperature was found to be 2.4 ± 0.2 eV.

Time-resolved data for several other propellants were also acquired (hydrogen, helium, krypton, and xenon); however, the results of the analysis of that data is not reported here for the following reasons. In the hydrogen and helium data, too few lines were available to make a statistically meaning linear fit (only two lines were available for hydrogen, and three for helium). On the other hand, many well defined lines were recorded with krypton and xenon. However, we were not able to locate the atomic energy level data necessary for temperature analysis of these plasmas. For analysis purposes in the next section, the electron temperature will be assumed to be the measured argon value of 2.4 eV for all of the propellants. This value of temperature will be used to calculate some characteristic plasma parameters in CSCX plasmas but the main focus of the section, which is to develop an analytical expression for the canting angle dependence on propellant molecular mass, will be shown to independent of temperature.

1.14 Summary of experimental results

The results of this section show that the experimental apparatus performed as designed; current sheets were formed and stably accelerated in a repeatable manner. For the most part, the diagnostics also proved to be well-suited for measuring the canting angle and thermodynamic state of the current sheet plasmas.

The first data presented in this section showed how the accelerator behaved as a circuit element. The data showed that the accelerator very weakly loaded the PFN: the current reversal was large ($\sim 80\%$), indicating small dissipation

in the load. Also, large changes (factors of 3 to 4) in the dynamic impedance (i.e., dL/dt) produce only a small variation ($\sim 10\%$) in the current, providing further evidence that most of the reactance in the circuit resides outside of the accelerator.

The photographic, magnetic and interferometric diagnostics present systematic, quantitative measurements of current sheet canting in a pulsed electromagnetic accelerator. The picture that emerges, from all of the diagnostics, is that, after breakdown, the current sheet bifurcates and evolves into a highly canted, propagating structure.

A few issues regarding the validity of the canting angle measurements at higher pressure levels need to be addressed. The propellant that is overrun at the cathode may form a plasma “bubble” which, in time, stretches across the entire discharge channel and, hence, provides an alternative current path – effectively short circuiting the initial current sheet. The presence of these structures is evident in most of the higher pressure level electron density data shown in the appendix of Ref. [1]. Also, the corresponding magnetic field data in that appendix show fluctuations suggestive of the passing of multiple current conduction zones. The influence of these “re-strikes” on the canting angle of the leading current sheet is uncertain. The phenomenon may possibly be beneficial in pulsed plasma thrusters, as the propellant will experience a multi-stage acceleration of sorts.

The next section, Analysis and Modelling, attempts to develop an explanation for why current sheets cant. The observations reported above, as well as the historical review presented earlier, will be drawn upon heavily to guide this conceptualization of the mechanisms which drive canting.

1.15 Analysis and Modelling

Having reported all of the experimental results in a rather fast-paced manner in the last section, we now turn to trying to better understand what the data as a whole mean. This section aims to explain, through further analysis of the experimental data and phenomenological modelling, why current sheets cant.

The first subsection of this section tabulates some relevant derived physical quantities which are calculated using the measurements from the last section. The next subsection draws on “conspicuous” features, noted in the analysis of the data, to develop a model for current sheet canting. Let us state from the outset that a complete theoretical model of the current sheet accelerator discharge is not something which can be easily grasped. This owes not only to the fact that all facets of the problem are highly unsteady, but also that many of the physical processes which constitute boundary conditions for the problem are poorly understood. Nevertheless, it will be shown that a simplified model of the canting process provides qualitative agreement with the trends in the data and, hence, gives us insight into the physical processes which drive canting. The last subsection looks back to the work of earlier researchers (see the review in Ref. [1]) and evaluates how well the proposed model agrees with

their observations.

1.15.1 Further analysis of the experimental data

Before modelling the canting problem it is useful first to collect in one place, and in a general sense, a description of the plasmas that we are dealing with – that is, to define their physical characteristics. This is especially important because in the absence of a holistic model, such as in the present case, it is often fruitful to identify some of the more conspicuous physical traits of the object under study and then use simple models to check the influence of each of these traits on the phenomenon of interest.

Characteristic plasma parameters

Figure 1.29 shows some calculated fundamental quantities which characterize CSCX current sheet plasmas. These plots were constructed using the magnetic field, electron density, and temperature data from Figs. 1.21, 1.25, and 1.28 (p=200 mTorr data was used in all of the calculations); these values are the peak measured values as the current sheet propagated through the measurement region near the center of the accelerator. The temperature measurement from argon current sheets (i.e., $T_e = 2.4 \pm 0.2$ eV) was used in all calculations. The parameters were calculated using their standard definitions[25]. Some additional characteristic parameter values are tabulated in Table 1.1. Throughout the calculations it was assumed that: $n_i = n_e$, $T_i = T_e$, and $Z = 1$.

Let us consider first some characteristic lengths in the CSCX current sheet plasmas. Figure 1.29a shows that the electron and ion gyroradii are small relative to the device dimensions (~ 5 cm), which shows that particle orbital motion is, for the most part, not interrupted by the proximity of the electrodes. This figure also shows that the mean free path (Coulomb collisions) is small compared to the current sheet dimensions (~ 1 cm), implying that the plasma is collisional for both electrons and ions. Using the approximate dimensions of the current sheet ($1 \text{ cm} \times 10 \text{ cm} \times 5 \text{ cm}$) and the calculated value of the transverse Spitzer resistivity (η_\perp), the Ohmic resistance of the current sheet is estimated to be $5 \text{ m}\Omega$, which is the same order of magnitude as the measured value (see subsection 1.8.2). For the ions, the mean free paths are also seen to be much smaller than the corresponding gyroradii, whereas the electron mean free path and electron gyroradius are seen to be comparable in magnitude. Table 1.29 lists two other characteristic lengths: the Debye length (λ_D), and the electron skin depth (δ_e). The Debye length is seen to be small compared to the device dimensions, so non-quasineutral electrode sheaths are expected to be small. The small value of the skin depth implies that the plasma is well suited for containing magnetic fields via surface currents, that is, forming current sheets.

Figure 1.29b shows some calculated characteristics frequencies in the CSCX plasmas. Of particular interest is the ratio of the gyrofrequency to the collision frequency (Coulomb) – the so-called Hall parameter. Table 1.29 shows that the Hall parameter is expected to be small for both electrons (Ω_e) and ions (Ω_i).

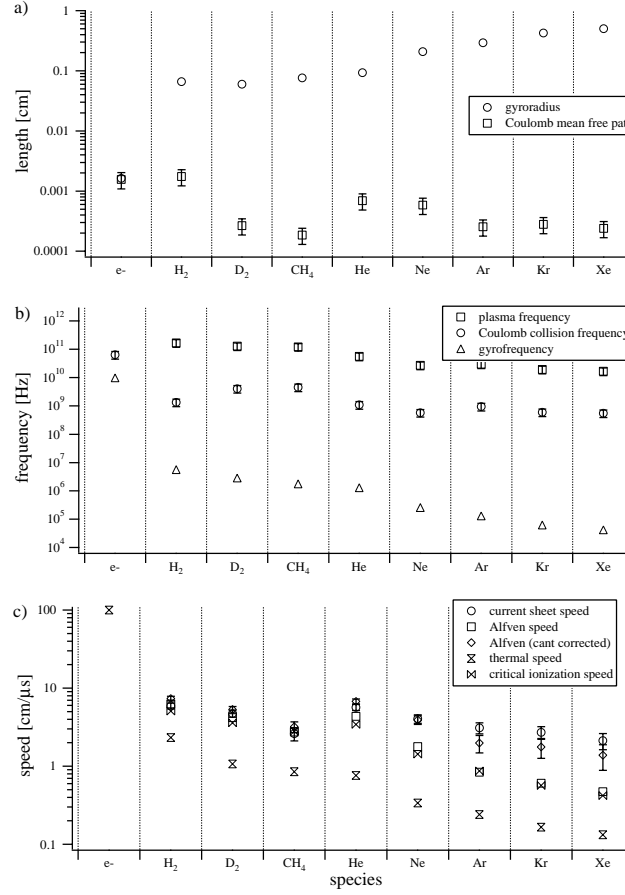


Figure 1.29: Characteristic values of a) length, b) frequency, and c) speed in CSCX current sheets (error bars not illustrated are comparable to marker size).

This implies that minimal Hall Effect-induced transverse (i.e., perpendicular to both the magnetic field and the applied electric field) components of current are expected to arise. It should be emphasized that these statements only apply to the Hall Parameter calculated using the average measured current sheet properties near the midsection of the accelerator – where the canting angle has stabilized. The Hall Effect may, as will be shown later in this section, play a very important role in causing the current sheet to cant, during the early stages of the discharge.

Figure 1.29c shows some characteristics speeds in the CSCX plasmas. The measured current sheet speed is seen to track close to the Alfvén (v_A) and critical ionization (v_{ci}) speeds for the lower atomic mass propellants, but diverges at

Table 1.1: Order of magnitude estimates of characteristic parameter values for CSCX current sheets (representative values used: $T = 2.4$ eV, $n = 3 \times 10^{16}$ cm $^{-3}$, $B = 0.35$ T).

parameter	value	parameter	value
λ_D [cm]	1×10^{-5}	β	1×10^{-1}
δ_e [cm]	1×10^{-3}	Ω_e	1×10^{-1}
η_{\perp} [Ω cm]	1×10^{-2}	Ω_i	1×10^{-3}

higher atomic masses. (Note:

$$v_A = \frac{B}{\sqrt{4\pi n_i m_i}} , \quad (1.3)$$

$$v_{ci} = \sqrt{\frac{2\phi_i}{m_i}} , \quad (1.4)$$

where B is the magnetic inductance, n_i is the ion number density, m_i is the ion atomic mass, and ϕ_i is the first ionization potential of the neutral gas.) This divergence may, in part, be due to the fact that $Z = 1$ was assumed in the calculations, whereas higher levels of ionization may have existed in the heavier propellants; this would lead to a lower calculated Alfvén speed, since n_i would actually be lower than n_e (which was measured and used in the calculations) in the plasma. However, even if $Z = 2$ is used in the calculation, multiplying the plotted Alfvén speeds by the corresponding factor of $\sqrt{2}$ would be insufficient to bring the Alfvén speeds for the heavier propellants into parity with the measured values. Figure 1.29c shows a canting-corrected Alfvén speed, v_A^c , which more closely tracks the measured current sheet speed. The calculation of v_A^c is described in subsection 1.15.2.

1.15.2 Modelling

In this subsection we develop phenomenological models of the current sheet which describe the evolution of its structure into sheet with a canted current front.

Heuristic model of current sheet structure

In preparation for postulating the complete current sheet canting model, it is useful to first set the stage by bringing together the experimental results and the calculated parameters above into a working, heuristic model of the current sheet. Since, as shown in the literature review presented in Ref. [1], there is no unanimity of opinion as to what goes on inside a current sheet, it is important for us to define first the palette from which we will draw and develop ideas.

Figure 1.30 shows a graphical conceptualization of the spatial configuration of the current channel, magnetic field, electron density and electron density gradient in an idealized current sheet. The breech is to the left and the current sheet accelerates to the right under the action of the $\mathbf{J} \times \mathbf{B}$ force. The calculations in the previous subsection show that the CSCX current sheets were collisional and the Hall parameter was calculated to be small; therefore, current conduction is expected to occur in a narrow channel orthogonal to the electrodes, as pictured. The experimental data (given in Fig. C.17 of the appendix of Ref. [1]) indicate that the CSCX current sheet width was on the order of 1 cm.

In theory, the idealized current sheet entrains the neutral gas that it overruns, leaving a vacuum region in its wake. The exact physical mechanism through which the gas entrainment takes place is not completely understood; Rosenbluth[26] described the process as collisionless, specular reflection while Lovberg[27] pointed to an accelerating electric field originating from an inertially-induced separation of electrons from their parent ions. Reflecting on the analysis of the data in the previous subsection, it appears that the entrainment process in CSCX current sheets can be explained more simply. The calculations in the previous subsection showed that in CSCX current sheets both the electron-electron and electron-ion collision frequencies are adequately large to characterize the plasma as a fluid. The current channel accelerates under the influence of the $\mathbf{J} \times \mathbf{B}$ force wherein the current carriers transfer the force to the bulk fluid through their tight collisional coupling. Now, on the front face of the current sheet, each of the incident neutral (test) particles with streaming speed v (relative to the current sheet) undergoes a “slowing down” relaxation process through collisions with the background current sheet (field) particles described by [25]

$$\frac{dv}{dt} = -\nu_{ii}v, \quad (1.5)$$

where ν_{ii} is the ion-ion collision frequency (it is assumed that the incident neutral particle is immediately ionized as it enters the current sheet). The incident particle will become stationary relative to the current sheet in a characteristic slowing time $\tau_s = 1/\nu_{ii}$ and a characteristic slowing distance $\lambda_s = v\tau_s$. From Fig. 1.29 we find typical values for ν_{ii} ($\mathcal{O}(10^9)$ Hz) and v ($\mathcal{O}(10^6)$ cm/s). This implies that λ_s is $\mathcal{O}(10^{-3})$ cm. Since the current sheet thickness is $\mathcal{O}(10^0)$ cm (as can be inferred from Fig. C.17 of the appendix of Ref. [1]), the incident neutral flux is expected to be subsumed into the current sheet plasma before penetrating very deeply. Again, this analysis assumes that the heavy particles enter the current sheet as ions; we have not addressed the ionization process. It may be possible for neutral atoms to pass through the current sheet without being ionized, yet still experience some acceleration through ion neutral collisions. Calculations of the relevant parameters (the ionization length and the ion-neutral collision frequency) are not carried out here, but remain a very relevant research question.

The current sheet propagation speed is theoretically limited to the so-called magnetosonic speed. In magnetized plasmas, the magnetosonic speed is the analogue of the sound, or acoustic speed in ordinary fluids. It is the character-

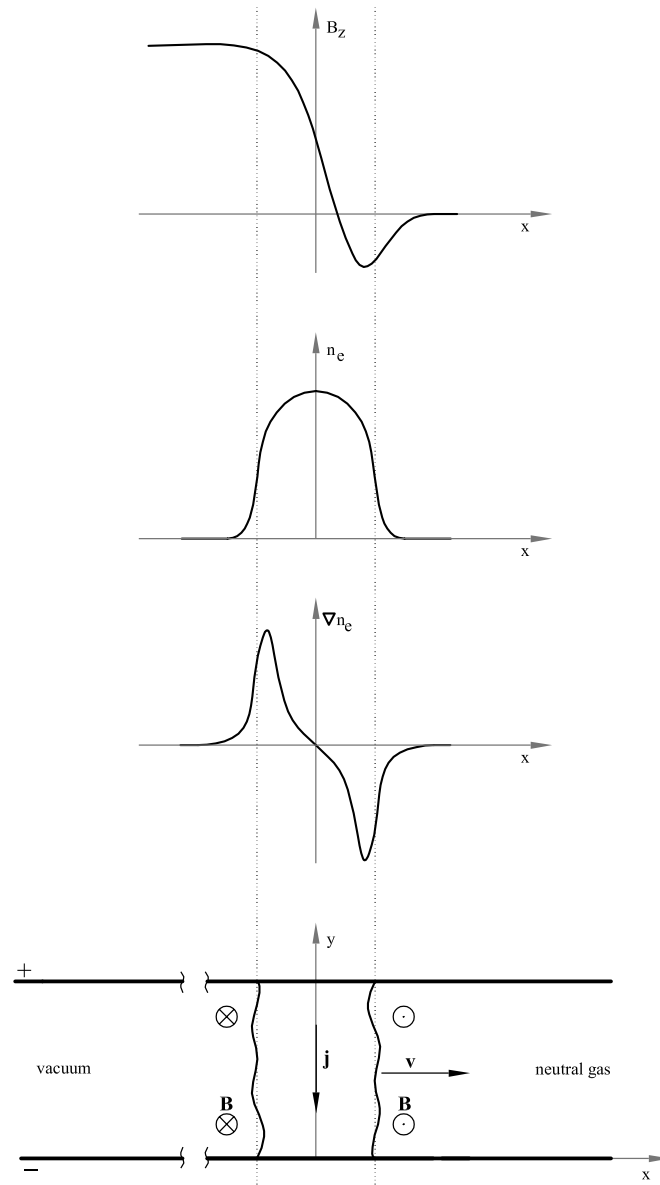


Figure 1.30: Heuristic model of a current sheet.

istic rate at which disturbances are propagated through a plasma, transverse to an imbedded magnetic field. When the magnetic field is one-dimensional (as is approximately the case in the CSCX experiment), the magnetosonic speed can be shown to be numerically equal to the Alfvén speed[28].

The expected distribution of the magnetic field strength in the ideal current sheet shown in Fig. 1.30 is suggested by the experimental data shown in the appendix of Ref. [1]. Because of the solenoidal nature of magnetic fields, the lines of force must wrap around the current sheet, resulting in a field with reversed direction in front of the current sheet. By solving the full boundary value problem with the conductors configured as illustrated, it can be shown that the magnetic field in front of (upstream side) the current sheet is much smaller than inside (downstream side) the current loop[29]. Nevertheless, there will be a region of finite width inside the current sheet where the magnetic field is reversed; this is interesting because it implies that the plasma near the leading edge of the current sheet will be accelerated opposite to the sheet velocity vector, \mathbf{v} . The magnetic field reverses at some point inside the current sheet – eventually reaching its peak value at the back edge of the current sheet. The magnetic field is expected to be constant between the back edge of the current sheet and the breech; figure 1.21 shows that this peak value was measured to be about 0.35 T (at the accelerator midsection) in the present experiment.

The simple electron density distribution sketched in Fig. 1.30 mirrors the general structure seen in many of the experimental profiles (see the appendix of Ref. [1]), where the typical peak electron density was found to be about $5 \times 10^{16} \text{ cm}^{-3}$. Near the edges of the current sheet, the typical electron density gradient was large (typically about $5 \times 10^{16} \text{ cm}^{-4}$, as can be inferred from Fig. C.17 of the appendix of Ref. [1]. The magnitude of this electron density gradient is large enough to characterize it as a “conspicuous” feature; it will be shown below that steep electron density gradients may be a catalyst for initiating the rapid evolution of current sheet canting.

Above we have outlined the expected behavior of an ideal current sheet. Below we propose a model for how current sheets in real accelerators may deviate from this idealized behavior.

Canting model preliminary description

One of the most distinguishing characteristics of the CSCX experiment, as compared to the majority of the earlier studies reviewed in Ref. [1], was the use of a protracted, non-sinusoidal current pulse. As will be shown below, allowing the current to stabilize enables remnants of early, transient processes to be distinguished from the stable propagation phase and provides insight into the cause of current sheet canting. Below, a phenomenological model for the evolution of a canted current sheet is proposed. The model draws on the parametric description of the current sheet plasma given in the previous subsection, as well as qualitative features from data in the previous section and from similar data obtained from the literature review in Ref. [1].

It is instructive to first present a qualitative description of the entire model

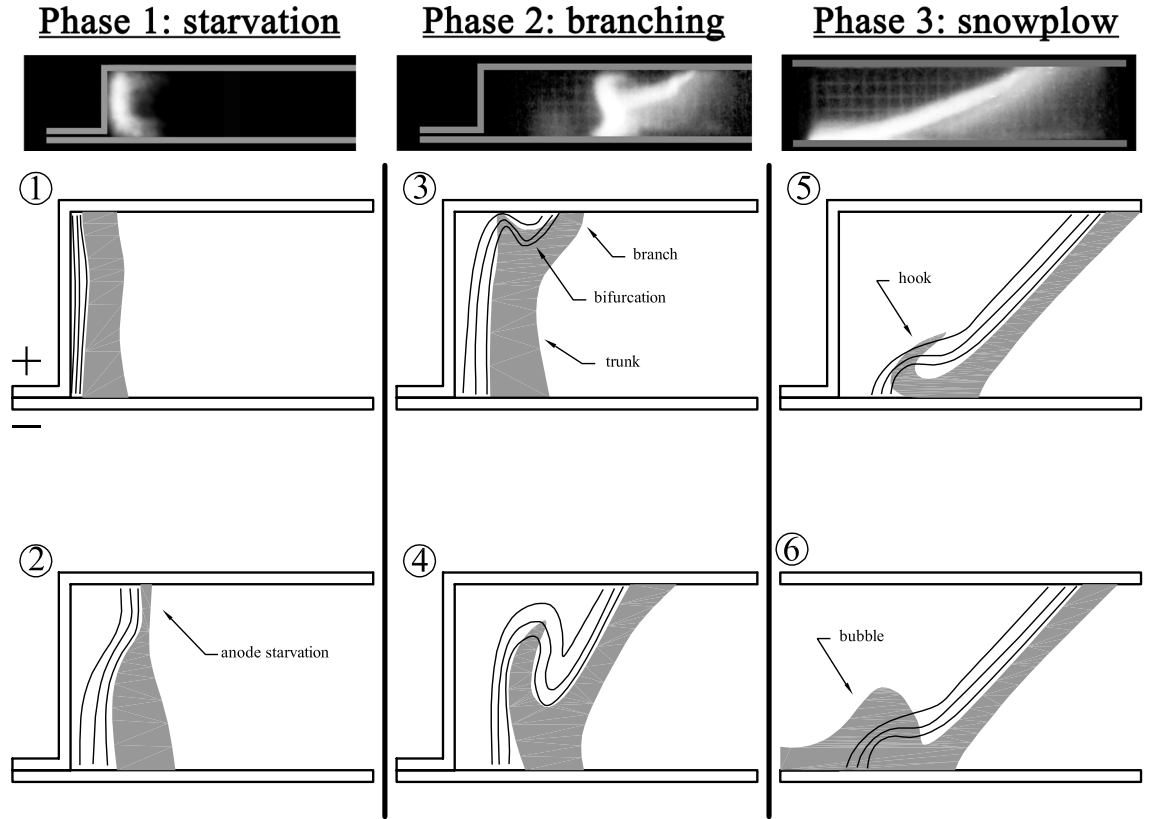


Figure 1.31: Illustration of a phenomenological model showing current conduction phases which may lead to a canted current sheet.

and then analyze the components individually (note: it is most expedient to describe the facets of the model as if they were facts rather than to repetitively state comments such as “this may happen” or “it is probable”, etc.. With this noted caveat in mind, let us consider a potential sequence of events that could lead to current sheet canting).

Figure 1.31 shows a sequence of events which could culminate in a canted current sheet. The grey objects are meant to illustrate the spatial extents of the current sheet plasma. The solid lines behind the current sheet are meant to represent magnetic flux tubes (i.e., the amount of magnetic flux contained between consecutive pairs of lines is constant from frame-to-frame).

The first illustration in Fig. 1.31 shows the initiation of the current sheet at the breach of the accelerator. In illustration 2 the current sheet is shown shortly after initiation. The plasma in the region near the anode becomes severely de-

pleted due to mass motion of the fluid toward the cathode (for reasons to be explained later). This first phase is termed the “starvation phase”, borrowing terminology from a phenomenon observed in MPD thrusters called “anode starvation” [30] (which probably originates from an altogether different physical mechanism).

Between illustrations 2 and 3 the plasma near the anode becomes so tenuous that it can no longer contain the magnetic field behind it. In a sense the current sheet can be thought of as a thin membrane (like a balloon) that contains a high pressure “magnetic fluid”. When the plasma near the the anode becomes sufficiently “thin”, the membrane quickly expands, or ruptures, allowing the contained magnetic flux to rapidly stream through. The initial current channel (henceforth referred to as the “trunk”) becomes bifurcated along the anode, as the streaming magnetic flux (and associated surface current) propagate ahead of the original current attachment point; this interface forms a new conduction path for the current sheet which connects the trunk to the anode (this new conduction path will be referred to as the “branch”). The newly formed branch and trunk form what was referred to by earlier researchers as the “anode foot”. Eventually the trunk becomes magnetically insulated (as the magnetic field wraps around the top of the trunk, transport from the top of the trunk to the anode is impeded by the transverse magnetic field) from the anode whereupon all of the current flows through the branch.

The branch propagates, borrowing from shock-tube parlance, as a contact discontinuity, with the anode as one wall and the trunk as the other. The magnetic pressure drives the contact point down along the branch-trunk interface and forward along the branch-anode interface, resulting in a canted current sheet. Anode starvation occurs to a lesser extent in the branch because it continually propagates into a fresh supply of propellant (the branch-anode interface is replenished with propellant from the *dynamic* pressure associated with its substantial axial speed). On the other hand, the initial current sheet (the trunk), is unable to avoid anode starvation because of its slow initial speed. As a final note on the branching phase, the magnetic pressure between the branch and the trunk causes the trunk to deform into the hook-like structure reported in many studies; the hook is simply a vestige of the initial current sheet.

The branching phase ends when the bottom of the branch reaches the cathode and the final phase (as shown in illustration 5), the snowplow phase, begins. The magnetic pressure is uniformly distributed on the back face of the canted current sheet and the current sheet is sufficiently dense in all areas to prevent further field leakage. The current sheet thus remains at a fairly constant canting angle during the remainder of its propagation. The tilt of the current sheet causes it to exert a cathode-directed component of the $\mathbf{J} \times \mathbf{B}$ force density on all of the propellant which is subsequently swept up. As a result, the propellant is preferentially directed toward cathode, where it accumulates. This “mass-funnelling” to the cathode may cause elevated plasma pressure along the cathode – leading to expansion of the propellant into the region *behind* the current sheet. A structure in the form of a plasma “bubble” behind the current sheet could form and, over time, grow large enough to span the entire gap be-

tween the anode and cathode and cause a “restrike”, which effectively short circuits the initial current sheet.

In the subsections which follow, each of the phases described above are analyzed in more quantitative detail in order to attempt to bridge the chasm between the conjectured model and the experimental facts.

Anode starvation phase

In the phenomenological model proposed above the sequence of events that lead to a canted current sheet is initiated by depletion of the conducting plasma in the vicinity of the anode. It is shown below that, in CSCX current sheets, diamagnetic drift induced fluid motion is of sufficient magnitude to cause the onset of anode starvation in the first few microseconds of the discharge.

Diamagnetic drift In subsection 1.15.2 we noted that one of the most conspicuous physical traits of current sheets are the large gradients in both the field strengths and thermodynamic state variables. It is therefore natural to first check the influence of these abrupt transitions on the phenomenon of interest. In current sheets the gasdynamic pressure and magnetic field gradients are generally quite large. Below we will analyze the influence of these gradients on the macroscopic evolution of the current sheet.

It is generally instructive to consider the trajectory of a single particle under the influence of the prescribed electromagnetic field of interest (the so-called guiding center theory) in order to gain a qualitative feel for how a plasma, which is a collection of particles executing similar trajectories, will behave. This work has been done for us: the presence of a pressure gradient transverse to a magnetic field is said to give rise to “diamagnetic drift” and, similarly, magnetic field gradients cause “grad B” drift[31]. Unfortunately, both of these phenomena have been the subject of widespread confusion and contradiction. The fundamental question is “do all guiding center theory trajectories manifest themselves in real fluids and, the corollary, do all mass motions predicted by fluid theory have an associated guiding center description?” The pursuit of answering to these questions has led to artifices such as “reflecting boundaries”[31] to ameliorate apparent paradoxes. The resolution of these issues has been handled best in the rigorous treatment of Woods[32]; in his own words:

The preference for mathematical formalism over physical mechanism is due in part to the misconception that in a tenuous gas the equations of fluid dynamics and thermodynamics can be *derived* from kinetic theory alone. By leaving the physical nature of pressure obscure, the formal approach fosters two misbeliefs that have afflicted plasma theory, namely that pressure gradients can exist without particle collisions, and that individual particles are not subject to pressure gradient forces. (pg. v)

The collisional force has a systematic, or non-random component that tends to drive the particles down the pressure gradient, and

a random component that scatters the particles. In a neutral gas the pressure and scattering forces are transmitted impulsively by abrupt collisions, whereas in a plasma the range of the Coulomb force results in a continuum of ‘soft’ or grazing collisions. Hence individual particles in a plasma experience a continuous pressure gradient force and are progressively scattered through a sequence of small angles. (pg. vi)

An obvious requirement relating particle and fluid dynamics is as follows: since a fluid motion is merely the average motion of an assembly of particles, then (i) individual particles are subject to *all* the forces acting on the fluid, and (ii) upon summation, forces known to act on the particles, but not on the fluid, must cancel. Despite (i) and (ii) it is widely believed that pressure gradients act on the fluid but not upon the particles, and that the forces responsible for the guiding center motions in magnetic gradients do not vanish on summation. (pg. vi)

So we are led to understand that diamagnetic drift is a real, observable effect whereas grad B drift does not affect fluid motion. Let us look at diamagnetic drift in more detail, from both particle and fluid perspectives.

Figure 1.32a shows a hypothetical situation in which we consider the forces on a single “test” particle immersed in a sea of many “field” particles (both types of particles are non-neutral). A density gradient in the field particles is indicated by progressive “bunching up” of the particles toward the left-hand side of the figure. The test particle is circumscribed by sphere of radius λ_D , the Debye length. Field particles within the Debye sphere undergo Coulomb collisions with the test particle. Since these collisions are not abrupt or impulsive but, rather, the long range nature of the Coulomb force causes an averaging over all of the individual particles forces, which results in a net continuous, averaged force. Since, as shown in the figure, there are more particles in the left hemisphere of the Debye sphere than in the right hemisphere, the net force on the test particle is to the right, and the test particle is expected to drift in that direction. The particle can be thought of as being under the influence of of quasi-continuous “pressure gradient force field”.

Now, if we add a transverse magnetic field, as shown in Fig. 1.32b, the test particles are expected to execute guiding-center trajectories as illustrated (more specifically, the particles execute the illustrated trajectories in the absence of *large-angle* collisions). Ions and electrons move in opposite directions because the sense of their gyro-motions are opposite. Also note that if both the direction of the magnetic field and the density gradient are simultaneously reversed, the particle trajectories remain the same. Upon summation over all particles, a diamagnetic current will arise because of the relative motion of the ions and electrons, and a net mass motion of the plasma will occur in the direction of the ion drift (the plasma moves with the ions because of their predominant inertia).

A more useful description of diamagnetic drift (one from which we can make representative calculations) can be derived from the fluid model. The high

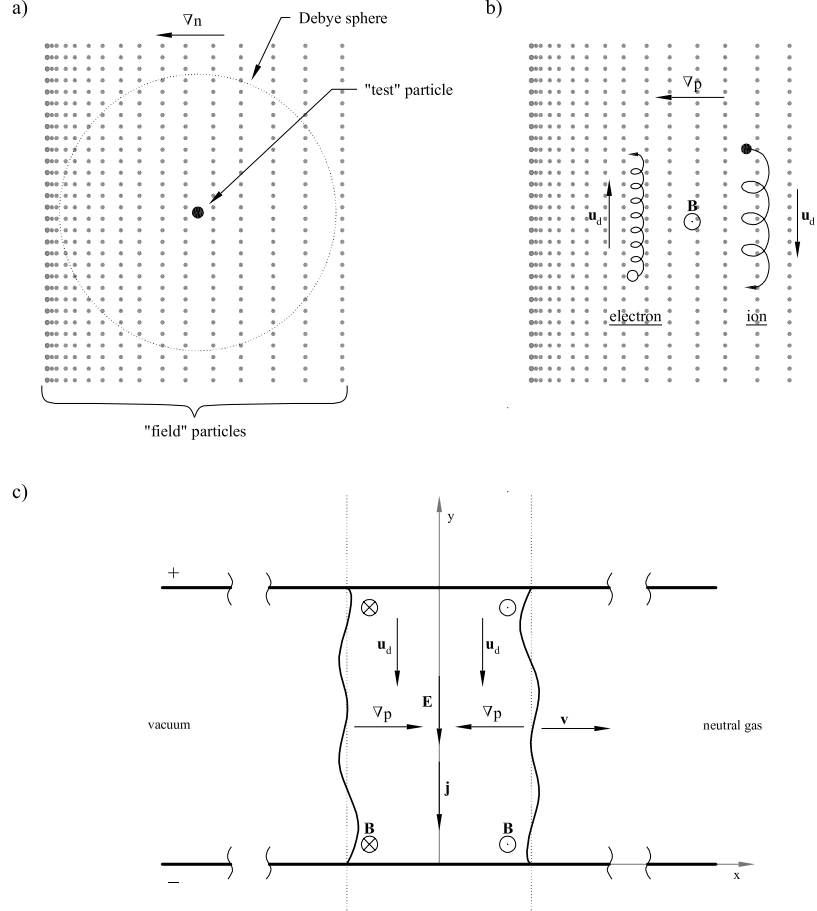


Figure 1.32: Schematics illustrating diamagnetic drift: a) test particle in a pressure gradient field, b) particle orbits in a pressure gradient field with crossed magnetic field, c) schematic of current sheet with vectors related to diamagnetic drift.

electron density and high collisionality of the CSCX current sheet plasmas allow it to be characterized as a fluid. Consider the motion of the current sheet plasma illustrated in Fig. 1.32c. Within the fluid framework the ions and electrons each obey a momentum equation of the form (neglecting viscous interactions with other species)[31]

$$m_j n_j \frac{d\mathbf{u}_j}{dt} = q_j n_j (\mathbf{E} + \mathbf{u}_j \times \mathbf{B}) - \nabla p_j \quad j = i, e \quad , \quad (1.6)$$

where m_j is the mass, n_j is the number density, q_j is the charge, \mathbf{u}_j is the fluid velocity in the laboratory reference frame, \mathbf{E} is the electric field, \mathbf{B} is the magnetic inductance, and p_j is the hydrostatic pressure.

If we consider the constant-speed propagation phase of current sheet motion, and consider only the velocity components transverse to the magnetic field then Eqn. 1.6 becomes

$$\mathbf{u}_{\perp j} \times \mathbf{B} = q_j n_j \mathbf{E} - \nabla p_j . \quad (1.7)$$

Taking the cross product of Eqn. 1.7 with \mathbf{B} yields

$$\mathbf{u}_{\perp j} = \underbrace{\frac{\mathbf{E} \times \mathbf{B}}{B^2}}_{\mathbf{u}_E} - \underbrace{\frac{\nabla p_j \times \mathbf{B}}{q_j n_j B^2}}_{\mathbf{u}_d} . \quad (1.8)$$

The first term in Eqn. 1.8 is the $\mathbf{E} \times \mathbf{B}$ drift (\mathbf{u}_E) and the second term is the diamagnetic drift (\mathbf{u}_d). The direction of \mathbf{u}_E is the same for both ions and electrons but, as in the particle model, the diamagnetic drift direction is seen to be charge dependent. As shown in both Figs. 1.30 and 1.32, \mathbf{E} is directed in the $-\hat{y}$ direction, and \mathbf{B} (for the most part) is directed in $-\hat{z}$ direction so that \mathbf{u}_E is directed in the $+\hat{x}$ direction. Similarly, the figures indicate that, for ions, \mathbf{u}_d is directed in the $-\hat{y}$ direction, or away from the anode throughout the current sheet.

Let us now consider the relative magnitude of each term in Eqn. 1.8. The magnitude of the electric field can be approximated using the measured voltage reported in subsection 1.8.2, typical values of \mathbf{B} are given in subsection 1.11, the temperature measurement is given in subsection 1.13.2, and the measured electron density gradients are given in Fig. C.17 of the appendix of Ref. [1]. Thus (taking $n_i = n_j = n$, $q_j = q_i = e$),

$$|\mathbf{u}_E| = \frac{|\mathbf{E}||\mathbf{B}|}{|\mathbf{B}|^2} \sim \frac{\mathcal{O}(10^3)\mathcal{O}(10^{-1})}{[\mathcal{O}(10^{-1})]^2} = \mathcal{O}(10^4) \text{ m/s} \quad (1.9)$$

and

$$|\mathbf{u}_d| = \frac{kT|\nabla n||\mathbf{B}|}{en|\mathbf{B}|^2} \sim \frac{\mathcal{O}(10^{-23})\mathcal{O}(10^4)\mathcal{O}(10^{24})\mathcal{O}(10^{-1})}{\mathcal{O}(10^{-19})\mathcal{O}(10^{22})[\mathcal{O}(10^{-1})]^2} = \mathcal{O}(10^3) \text{ m/s}. \quad (1.10)$$

The $\mathbf{E} \times \mathbf{B}$ drift speed is of the same order of magnitude as the measured current sheet propagation speeds; this is as it should be since it is in fact the microscopic $\mathbf{E} \times \mathbf{B}$ particle drifts which cause the current sheet to accelerate. What is somewhat surprising is that equation 1.10 shows that the calculated diamagnetic drift in CSCX current sheets is sufficient in magnitude to induce ion fluid motion toward the cathode at appreciable speeds; in fact, the data in Fig. C.17 of the appendix of Ref. [1] indicate that ∇n approaches 10^{25} m^{-4} in some cases, implying that \mathbf{u}_d may be comparable in magnitude to \mathbf{u}_E in some cases.

We can also estimate the amount of current induced by diamagnetic drift. According to Eqn. 1.8 electrons will experience diamagnetic drift in the opposite

directions of ions, so that the net current will be twice that due to the ion drift alone:

$$j_d = |n_i q_i \mathbf{u}_{di} - n_e q_e \mathbf{u}_{de}| = |2ne\mathbf{u}_d| \sim \mathcal{O}(10^{22})\mathcal{O}(10^{-19})\mathcal{O}(10^3) = \mathcal{O}(10^6) \text{ A/m}^2. \quad (1.11)$$

Since the cross sectional area of the current sheet is $A \sim \mathcal{O}(10^{-3})$ (1 cm thick by 10 cm wide), the total diamagnetic current can be estimated as

$$I_d \sim j_d A \sim \mathcal{O}(10^6)\mathcal{O}(10^{-3}) = \mathcal{O}(10^3) \text{ A}. \quad (1.12)$$

Referring back to subsection 1.8.1, we find that the predicted diamagnetic current may contribute on the order of ten percent of the total measured current. This conclusion is potentially related to the assertion put forth (although not in a formal manner) by the earlier researchers (see the review in Ref. [1]) that ion current contributes significantly to the total discharge current.

Since we are considering the potential for diamagnetic drift to cause anode starvation, it is useful to describe the relevant characteristic time and length scales for diamagnetic drift-induced anode starvation. To start, it seems logical to first define what we mean by the term “anode starvation”, that is, how much of the initial plasma must be transported away from the anode before we label it “starved”? This is a relative question which, fortunately, we do not have to answer directly. Instead, our approach will be to obtain the characteristic time for the canting process (τ_c) from the experimental data, and then calculate the plasma displacement (L_d) that diamagnetic drift is capable of inducing on that timescale. This characteristic length will then be used as an input parameter in a phenomenological model for the canting process, and the relevance of diamagnetic drift will be (albeit indirectly) revealed by the model’s ability to follow the trends in the measured current sheet canting angle data.

The characteristic time for the canting process can be gleaned from the experimental data; in particular, the magnetic field data in Fig. 1.23 shows that the time for the current sheet to reach a (fairly) constant canting angle is several microseconds, so we take

$$\tau_c = \mathcal{O}(10^{-6}) \text{ s}. \quad (1.13)$$

Therefore, the characteristic length for diamagnetic drift-induced plasma displacement normal to the anode (on the canting-process timescale) is (using equation 1.10)

$$L_d \sim |\mathbf{u}_d \tau_c| \sim \mathcal{O}(10^3)\mathcal{O}(10^{-6}) = \mathcal{O}(10^{-3}) \text{ m} = \mathcal{O}(1) \text{ mm}. \quad (1.14)$$

The magnitude of this characteristic length is perhaps not surprising, since the experimental measurements yield a comparable estimate for the *axial* (note: the axial direction is the direction of the thrust axis, or the $+\hat{x}$ direction, as illustrated in Fig. 1.15.2) characteristic length, $n/\nabla n$. Using the data from Figs. 1.25 and Fig. C.17 of the appendix of Ref. [1] we find that $n/\nabla n \sim 5 \text{ mm}$ for all cases, which is the same order of magnitude as the *normal* characteristic length value calculated in Eqn. 1.14.

Note that we are not trying to prove here that diamagnetic drift is the only mechanism that can cause anode starvation; there may in fact be alternative processes at play in the CSCX current sheets that lead to anode starvation. Our aim was to show that at least one process has been identified which can cause the current sheet plasma to be pulled away from the anode, on the timescale of the canting evolution. In the next subsection, we describe how anode plasma depletion can lead to current sheet canting, through a sequence of events that we term “branching”.

Branching phase

The argument that is put forth in this study suggests that current sheet canting is caused by rapid penetration of the magnetic field through a narrow region of the current sheet along the anode. This perspective on the problem is adopted based on the experimental data. In particular,

- The photographic data (see, for example, Fig. 1.17) clearly show the projection of a luminous canted structure ahead of the initial current which initiates near the anode.
- The magnetic field data in Fig. 1.23c show that canting occurs rapidly in the early stages of the discharge, after which a fairly constant canting angle propagation phase takes place.
- The magnetic field data in Fig. 1.24 show that the current sheet bifurcates along the anode early in the discharge. No similar phenomenon is seen in the cathode magnetic field traces.

We now turn to explaining how the branching process takes place. We are therefore led to consider theories relevant to the penetration and expulsion of magnetic fields in plasmas. A recent series of seminal articles by Fruchtman[33, 34, 35] appears to have direct relevance to the present study and, as such, will be drawn upon heavily. Fruchtman’s major contribution in this area has been to formalize the description of the role that the Hall effect plays in accelerating the penetration of magnetic fields through plasmas. The Hall effect may be relevant to the current sheet canting problem because the anode starvation process described in the previous subsection may create a region in the current sheet where the Hall parameter becomes appreciable in magnitude.

In the next subsection the process of rapid magnetic field penetration is discussed. The results of the analysis are used in the succeeding subsection to calculate predicted canting angles in the CSCX accelerator.

Rapid penetration of magnetic fields into plasmas We are concerned here with understanding the penetration of magnetic fields into plasmas that are being pushed by those selfsame fields. Classically, two extreme cases can be distinguished. If the plasma is highly conductive, the penetration of the fields is confined to a thin layer of thickness on the order of the electron skin

depth and the plasma is pushed by the magnetic pressure (snowplowed) with a characteristic speed (the Alfvén speed)[36]

$$v_A \equiv \frac{B}{\sqrt{4\pi n_i m_i}} , \quad (1.15)$$

where B is the magnetic inductance, n_i is the ion density, and m_i is the atomic mass of the ions. If, on the other hand, the plasma is highly resistive, the magnetic field simply diffuses through the plasma (without imparting significant momentum to the plasma) with characteristic speed[36]

$$v_D \equiv \frac{c^2 \eta}{4\pi L_D} , \quad (1.16)$$

where c is the speed of light in vacuum, η is the plasma resistivity, and L_D is the characteristic diffusion length.

Fruchtman *et al*[33, 34, 35] describes a mechanism for fast magnetic field penetration into a plasma which is *independent* of the resistivity, which he calls the “convective skin effect” (the relevant results are reported here, the interested reader is directed to the references where the detailed derivations are shown). The mechanism results from the Hall electric field, which allows the magnetic field to penetrate the plasma with characteristic speed

$$v_C \equiv \frac{c^2(B/n_e e c)}{4\pi L_C} , \quad (1.17)$$

where $-e$ is the electron charge and L_C is the characteristic length of a density gradient in the plasma. The term $\eta_H = B/n_e e c$ can be thought of as a “Hall resistivity”. As with conventional plasma resistivity, the Hall resistivity allows the magnetic field to rapidly propagate through a plasma without imparting significant momentum to the ions (the Hall resistivity is, however, non-dissipative).

In the course of his derivations Fruchtman defines the circumstances under which the convective skin effect is “activated”. He shows that Hall effect-enhanced magnetic field penetration will occur when a density gradient occurs in the (pushed) plasma with characteristic dimension of the order of the ion skin depth,

$$\delta_i \equiv \sqrt{\frac{m_i c^2}{4\pi n_i e^2}} . \quad (1.18)$$

Also, a parameter equivalent to the magnetic Reynolds number can be defined, which is the ratio of the plasma pushing speed (v_A) to the field penetration speed (v_C):

$$R_C \equiv \frac{v_A}{v_C} = \frac{\frac{B}{\sqrt{4\pi n_i m_i}}}{\frac{c^2(B/n_e e c)}{4\pi L}} = \frac{L_C}{\delta_i} . \quad (1.19)$$

Equation 1.19 shows us that when L_C is less than the ion skin depth, field penetration dominates over pushing.

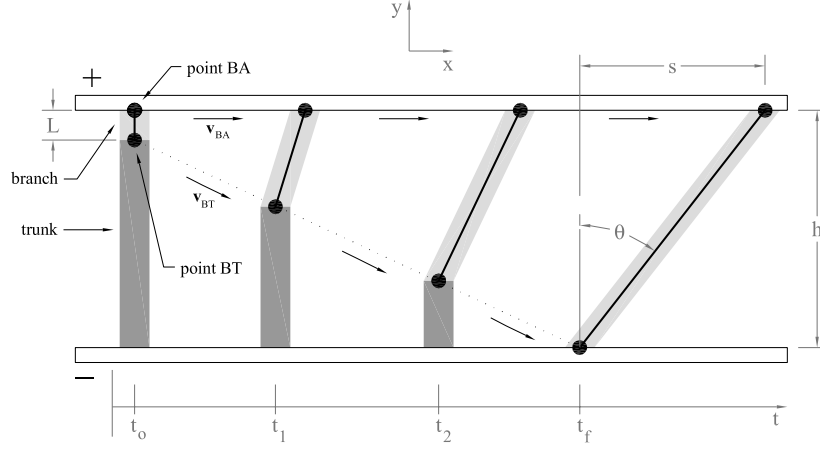


Figure 1.33: Schematic of current sheet canting angle calculation elements.

Let us consider some typical CSCX current sheet parameter values to demonstrate the relevance of the Hall effect on the current sheet canting problem. From Fig. 1.29 we see that the ion plasma frequency (ω_{pi}) is $\mathcal{O}(10^{11})$ rad/s so that

$$|\delta_i| = \left| \frac{c}{\omega_{pi}} \right| \sim \frac{\mathcal{O}(10^8)}{\mathcal{O}(10^{11})} = 1 \text{ mm} . \quad (1.20)$$

Now, in subsection 1.15.2 we found that, on the timescale of the canting process, the diamagnetic drift in CSCX current sheets was capable of inducing a density gradient of characteristic length $L_d = 1\text{mm}$. The influence of the convective Hall effect is found by considering the effect of such a gradient within the framework of Fruchtmann’s model, that is, setting $L_C = L_d$. From equation 1.19 we find that $R_c \sim 1$, indicating that Hall effect-induced magnetic field penetration may significantly affect the evolution of CSCX current sheets, near the anode, during the early stages of the discharge.

Predicted terminal canting angle We now attempt to calculate the canting angles that will result from the competing processes of plasma pushing and Hall effect-induced magnetic field penetration, in the CSCX accelerator. The model is simply an attempt quantify the statements given in subsection 1.15.2, where the evolution of the canting angle was described in a general sense.

The approach will be to track the trajectories of two points on the branch: the branch-trunk interface point (point BT) and the branch-anode interface point (point BA). The elements of the model are schematically illustrated in Fig. 1.33. The figure shows “snapshots” of the current sheet at several different times. The branch comes into existence at some time t_0 ; the points BA and BT

are assumed to initially be separated by the distance L_C – the characteristic length of the anode density gradient. The motion of the point BA is assumed to be governed by the convective skin effect; the point BA is assumed to propagate with constant velocity $\mathbf{v}_{BA} = v_C \hat{x}$. The motion of the trunk and the point BT is assumed to be governed by plasma pushing; thus, the point BT is assumed to propagate both forward and downward at the Alfvén speed: $\mathbf{v}_{BT} = v_A \hat{x} + v_A \hat{y}$. The point BT has two speed components because the flux tubes that wrap around this point (see frame 3 and 4 of Fig. 1.31) exert both axial and transverse components of magnetic pressure, driving the point both forward and downward. The branching phase is assumed to terminate when the point BT reaches the cathode (indicated by time t_f in the figure). The predicted terminal canting angle (θ) is calculated using the axial separation of the points BA and BT (s in the figure) at time t_f .

Using the definitions of the speeds given above and Eqn. 1.19 it is easy to show that the predicted final canting angle is

$$\theta = \tan^{-1} \left[\left(\frac{h - L_C}{h} \right) \left(\frac{1 - R_C}{R_C} \right) \right], \quad (1.21)$$

$$R_C = \frac{L_C}{\delta_i} = \sqrt{\frac{4\pi n_i e^2}{m_i c^2}} L_C. \quad (1.22)$$

Equation 1.21 tells us that the canting angle dependence on propellant mass enters through the parameter R_C , which in turn depends on the ion skin depth, which is proportional to the square root of the ion mass. It should be noted that, at least in our analysis, the mass dependence only comes through δ_i , since L_C is related to the diamagnetic drift speed, which is mass-independent. This is important because it allows us to assume a constant value of L_C when plotting the functional dependence θ on m_i ; there are no free parameters in the model.

Using the diamagnetic drift-induced characteristic density gradient L_C (1 mm, from Eqn. 1.14), the typical measured number density ($5 \times 10^{16} \text{ cm}^{-3}$, from Fig. 1.25), we can plot the predicted canting angle as a function of the propellant atomic mass. This curve, along with all of the experimental datum points from Fig. 1.26, are shown in Fig. 1.34. The figure shows that the model captures the general trend of the experimental data; the model predicts that the canting angle will initially rapidly increase with propellant atomic mass and then taper off toward a more asymptotic trend for higher atomic mass propellants. These are the same trends that are seen in the experimental data.

It is not surprising that the model does not give precise quantitative agreement with the data for the higher atomic mass propellants. The model predicts the “worst case scenario”, or *maximum* expected canting angle, because the simplification in the model that allows the point BA to propagate with velocity \mathbf{v}_C along its entire trajectory is probably not the type of behavior realized in the experiment. In the real accelerator the branch anode attachment is likely to transition continuously from the Hall-convective behavior back to plasma pushing – as it picks up speed and the incoming propellant obliterates the anode

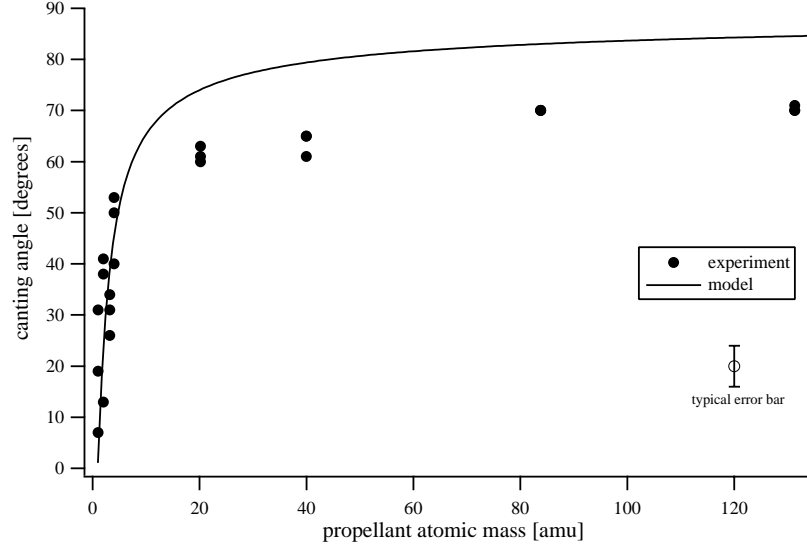


Figure 1.34: Comparison of model and measured current sheet canting angle versus propellant atomic mass.

density gradient. If we were to modify the model to divide the branch trajectory into, say, two parts (half Hall-convective and half plasma pushing), the effect would be to cause the model curve to bend-over more rapidly and come into closer agreement with the data. But, in light of the rather crude order of magnitude estimates used throughout this analysis, further refinement of the model is not warranted. The important point is that the simplest model, which embodies the essence of the proposed physical processes, accurately picks up the trends in the experimental data and gives fairly close quantitative agreement. We shall henceforth refer to the model described above as the “fast field penetration canting model”.

Let us summarize what has been proposed here. Physically, Fruchtmann’s model shows that the Hall effect can lead to an effective mechanism for magnetic field transport when a non-uniformity (i.e., a density gradient) appears in a plasma that is being pushed by the field. This argument is formally derived through the fluid equations. In particular, inclusion of the Hall term in the generalized Ohm’s law leads to a term in the equation for the time-evolution of the magnetic field that allows for the rapid convection of magnetic field through the plasma, without displacement of the ions, with characteristic speed v_C . This competes with the convection of the magnetic field where the ions are displaced, that is plasma pushing, which has characteristic speed v_A . Consideration of the relative magnitude of each effect reveals that the Hall-convective penetration becomes comparable in magnitude to plasma pushing when a density gradient of scale length comparable to the ion skin depth appears. In our fast field

penetration canting model we propose that such a density gradient does arise along the anode in the CSCX accelerator. The variations in the ion skin depths among the different propellants (the ion skin depth is proportional to $\sqrt{m_i}$) leads to different Hall-convective field penetration speeds, and hence different final canting angles, as illustrated in Fig. 1.34.

Snowplow phase

The experimental data show (see Fig. 1.23c) that the canting angle evolves during the first few microseconds of the the discharge, after which the current sheet propagates at a fairly constant angle. During this latter quasi-steady state, plasma pushing, or snowplowing, is expected to be the primary mode of operation.

Figure 1.29c shows that, for higher atomic mass propellants, the measured current sheet speed is substantially higher than the Alfvén speed, which was calculated from measured parameters. The values can be brought into closer agreement if a canting-corrected Alfvén speed is defined:

$$v_A^c = \frac{v_A}{\cos \theta} . \quad (1.23)$$

Physically Eqn. 1.23 is a statement that says since the magnetic pressure force acts normal to the current sheet, it is the *normal* component of the current sheet speed that propagates at the Alfvén speed. Figure 1.29c shows that introducing this correction factor brings the measured speed and calculated Alfvén speed into closer agreement.

An immediate question is “what effect does canting have on the ability of the current sheet to sweep up and accelerate propellant”? Referring to the electron density data in Fig. 1.25b, we see that the electron density on the anode side is much lower than that on the cathode side (note: both beams were about 5 mm away from each electrode – well outside the electrode Debye sheath regions). This density imbalance may suggest that the effect of canting is to force the plasma entrained by the current sheet toward the cathode (clearly, the force density vector $\mathbf{J} \times \mathbf{B}$ is largely directed toward the cathode) where it stagnates and is then left behind. This picture is supported by the cathode laser beam electron density traces, which show a significant plasma density that persists after the current sheet has passed. Also, the photographs in Fig. 1.17 show a long luminous layer of plasma behind the current sheet. This information indicates that, in addition to causing an off-axis component of thrust, current sheet canting may undermine the effective sweeping up of propellant as the current sheet propagates. Indeed, canted current sheets may act, undesirably, like *real* snowplows – never accumulating but, rather, throwing their load to the side (in our case, underneath) as they pass by.

We can make this assertion a bit more quantitative by considering what the expected electron density at the sampling location should be, and then comparing this value with our measurements. If the current sheet was a perfect propellant sweeper, we would expect the total number of electrons in the current sheet at the sample location to be about the same as the total number

of propellant particles that initially filled the volume between the breech and sampling location (this, of course, assumes single ionization). Helium is a good candidate for this analysis, since its high second ionization potential precludes the presence of a significant population of double ions. The interferometric data taken with the upstream probe in configuration 1 should give an adequate representation of the average properties of the current sheet since it was traversed by the plasma midway between the anode and cathode. Let us consider the tests with helium propellant at 75 mTorr ambient fill. Using the current sheet width data in Fig. C.17b of the appendix of Ref. [1]b, the electron density data in Fig. 1.25, and the dimensions of the discharge chamber (see Fig. 1.4), the total number of electrons in the current sheet can be estimated:

$$N_e = n_e V_{sheet} \approx (1 \times 10^{16} \text{ cm}^{-3})(1\text{cm})(5\text{cm})(10\text{cm}) = 5 \times 10^{17} \text{ electrons} . \quad (1.24)$$

On the other hand, the total number of neutral propellant particles encountered by the current sheet as it propagated to the sampling location (35 cm downstream of the breech) was

$$N = \frac{pV_{chamber}}{kT} \approx \frac{(10\text{Pa})(0.05\text{m})(0.1\text{m})(0.35\text{m})}{(1.38 \times 10^{-23}\text{J/KgK})(300\text{K})} = 4 \times 10^{18} \text{ neutrals} . \quad (1.25)$$

Comparing the two figures implies that only about 10% of the propellant was entrained into the current sheet. The rest was presumably convected to the cathode, where it was overrun and left to trail behind the propagating front. This does not mean that the propellant utilization efficiency was only 10%, as the current sheet may have imparted a significant amount of axial momentum to the propellant as it transported it to the cathode; the exact amount of momentum transferred in this process remains an open research question. Although this is an important issue from a propellant utilization efficiency perspective, no attempt is made here to model the process since, as the data indicate (again, see Fig. 1.23c), the process does not drastically alter the canting angle that is established early in the discharge.

The propellant entrainment calculation above neglects the possibility that the current sheet entrains and accelerates a large amount of neutral atoms – atoms that are never ionized yet are convected along with the current sheet. If this was in fact the case, the analysis above would be invalid, since the interferometer is insensitive to the presence of neutrals. Such a scenario could arise if, for example, the ions in the current sheet are tightly collisionally coupled to the neutrals. Theoretically, the presence a prodigious amount of neutral gas in the current sheet is unlikely, since the high measured temperature (~ 2 eV, see subsection 1.13.2) and low gas density should result in a completely ionized gas[3]. However, complete analysis of the potential for entrainment of neutrals into the current sheet would involve making an estimate of the ionization length and ion-neutral mean free path. These type of calculations are beyond the scope of what we are trying to accomplish here, but should be part of a more comprehensive study on the propellant sweeping characteristics of current sheets. Our purpose here was to show that the electron density data cannot account

for all of the propellant, suggesting the possibility that canting is causing it to be driven toward the cathode where it is overrun by the current sheet.

1.15.3 Correlations with earlier research

It is interesting, in light of the analysis presented in this section, to reflect back on the results from earlier researchers, as reviewed in Ref. [1]. It is clear that several of the researchers were trying to draw conclusions from data that were taken while their accelerators were in the branching phase; they did not have the benefit of a protracted current pulse, which exposes the transient nature of the canting process.

Since Johansson[37] was the only prior researcher to publish a theory for current sheet canting (which we termed the ion conduction current canting model), it is fitting that we should return to consider his conclusions, and compare them with the fast field penetration canting model put forth in the present study. Johansson proposed that a portion of the current sheet (of height h_o) will cant in order to direct ions toward the cathode. This type of partitioning of the current sheet into a canted and uncanted section was observed in the CSCX study as well (see, for example, the top-center photograph in Fig. 1.31); however, in the present study, the presence of two distinct regions of the current sheet was found to be the manifestation of a *transient* phenomenon, which we termed branching. In all cases, the structure of the current sheet was found to eventually evolve into a continuous, straight, canted front. It seems clear that Johansson attempted to draw conclusions from data which showed the presence of both the branch and trunk; evidently he assumed that the features were stable structures. Johansson's theoretical formula for h_o cannot be compared with the CSCX experimental data since h_o is observed to continuously increase, until the canted portion of the current sheet spans the entire inter-electrode gap. The two models share in common the notion that the current sheet cants near the anode. Beyond this the two models diverge. The ion conduction current canting model suggests that the canting of the current sheet near the anode will maintain its general shape as the current sheet propagates whereas the fast field penetration canting model proposes that the distortion of the current sheet near the anode leads to a "runaway" effect wherein the magnetic field propagates ahead of the initial current sheet and forms a straight, canted, current sheet that spans the entire discharge chamber.

The data from the Princeton Z-pinch experiments appear to indicate that the current sheets reached the centerline of the accelerator before the branch-trunk interface completed its migration to the cathode. Additionally, the images from Lovberg's rectangular-geometry accelerator study clearly show the bifurcation of the current sheet; however, the electrodes were not long enough for the current sheet to transition into its stable, constant-angle phase. Similarly, MacLelland's images also show current sheets in various stages of branching. His schlieren photograph bears a strong resemblance to some of the intermediate schematics of the current sheet canting model proposed above (see Fig. 1.33).

Lovberg's coaxial geometry accelerator research is insightful because it may

indicate a path toward inhibiting current sheet canting. In Lovberg's initial coaxial accelerator work (solid electrodes), polarity-dependent current sheet canting was observed. On the other hand, he did not observe the same effect when he reversed the polarity in his coaxial-geometry, slotted-outer-electrode accelerator. The reason for the different results between the two experiments may be due to the second experiment's slotted outer electrode and the use of a uniform backfill of propellant surrounding the second accelerator. It is possible that as the formation of a radial density gradient, near the anode, was inhibited by the replenishment of propellant from outside the accelerator – through the slotted outer electrode. The influx of propellant into the depleted region may have suppressed anode starvation and the associated accelerated magnetic field penetration near the anode. This is a revealing, albeit inadvertent, example of how propellant feeding might be used to suppress current sheet canting. When Lovberg's accelerator was operated with the center electrode as the anode, we see the expected behavior (that is, a bullet shaped current sheet). The feature that Lovberg considered anomalous, the planar, non-conducting plasma sheet behind the main front is probably the initiation trunk; as expected near a solid electrode, anode starvation allowed the magnetic field to propagate around the initiation trunk to form the leading branch current sheet. It should be emphasized again that Lovberg's experiments used two different propellant loading techniques (ambient fill and injection), which may in fact have played a role in producing the different results. However, without knowing the details of the initial propellant distribution in each accelerator, it would be difficult to make conclusions regarding the influence of each loading method.

1.15.4 Concluding remarks on the analysis

This section has attempted to characterize the plasma environment in the CSCX accelerator, identify physical mechanisms which could potentially cause current sheet canting and, finally, to implement those mechanisms into a simple canting model, which draws on available experimental data, for comparison with experimental canting-angle data. Before leaving this section, a few comments are in order regarding some issues that were not discussed in the analysis, yet may be relevant.

First, no mention has been made of the experimentally measured variation in canting angle with pressure. The data shows (see Fig. 1.26), for the most part, that the lowest canting angles were attained at the highest pressure levels. Since the canting angle is a function of δ_i and L_C (see equation 1.21), which are in turn related to n_i and ∇n_e , we might consider using the experimental data to investigate the influence of pressure; however, the size of the error bars in the measurements (see, for example, Fig. C.17 of the appendix of Ref. [1]) precludes a meaningful analysis, and reinforces our rationale for keeping the calculations used in the phenomenological modelling to order-of-magnitude estimates.

Still, some qualitative statements regarding pressure dependence can be made. The lower atomic mass propellants show a wide scatter in canting angle at different pressures. This may be related to contamination. Figure 1.34

shows that, at the low atomic mass limit, the canting angle rapidly increases for small incremental increases in atomic mass. Therefore, we might expect that small amounts of contaminants in the propellant (which might originate from adsorbed gas in the electrodes, or electrode erosion) could slightly increase the effective, or average, atomic mass of the propellant, and lead to large increases in the canting angle. The lower pressure experiments would be more sensitive to contamination (given a constant amount of contaminant material), since the net concentration of contaminants, and hence the effective atomic mass, would be higher than in the higher pressure experiments. This assertion is given credence by the fact that the data show that the highest pressure experiments gave the smallest measured canting angles.

Another factor that has not been discussed is the influence of the rapid current rise (see Fig. 1.14) that occurs during the initiation of the discharge. Indeed, the rise-rate is $\mathcal{O}(10^{11})$ A/s, which qualifies it as a “conspicuous feature” in our problem. We have attempted to model the influence of dI/dt on anode starvation, using the unsteady fluid equations, but have yet to find a correlation. Nonetheless, it is a topic that merits further investigation.

The purpose of this section has been to present a *plausible* explanation for why current sheets cant. The scant amount of data available from the breech region of the accelerator, where the transient canting process takes place, makes it difficult to ascertain that the proposed physical mechanisms are actually at play. It has been tacitly assumed that the measurements taken downstream are representative of the current sheet properties near the breech. Accordingly, emphasis has been put on order-of-magnitude analysis and trends in the data. Furthermore, deeper issues related to the proposed physical canting mechanisms have not been addressed. For example, direct application of Fruchtman’s results to the present problem requires detailed knowledge of, among other factors, the local collisionality, the penetration of the magnetic field into the bounding conductors, and an analytical expression for the density gradient. Clearly, measurements were not made in the CSCX study to quantify these parameters near the breech, in the vicinity of the anode; in actuality, given additional time and resources, it would still be difficult to conceive of measuring these quantities (e.g., measuring density gradients on a sub-millimeter scale). The reader that may be unconvinced by our attempt to make a case for the proposed canting mechanism, using available data, is invited to consider the inverse of what we have done here. That is, to assume that the convective skin effect allows fast magnetic field penetration, and then ask what conditions near the anode must exist to allow the field to rapidly penetrate. First, one must choose a representative estimate for the number density, perhaps based on the initial fill density; having done so, the ion skin depth can be calculated. For the convective skin effect to be activated, a density gradient of scale length comparable to the ion skin depth, by some unspecified mechanism, must somehow form. Carrying out this procedure leads to values of δ_i (and, hence, L_C) that are reasonable, that is, length scales that are much smaller than the accelerator dimensions, and much larger than sheath dimensions, the electron skin depth, etc.. The point is as follows: there is no *a priori* reason to exclude the convective skin effect as a

candidate mechanism for causing current sheet canting.

Furthermore, since the available data from the CSCX study and other researchers do not contradict the proposed phenomenological model, it should be considered a strong candidate, even in the absence of detailed experimental data in the anode region. Prior to developing the fast field penetration canting model, we made many attempts to find revealing trends in the canting data by plotting the datum points as a function of individual and products of characteristic parameters. None of these attempts were successful in capturing the relatively sharp “knee” in the relationship between canting angle and propellant atomic mass. However, the relatively complex relationship predicted by the fast field penetration canting model is able to capture this trend.

1.16 Conclusions

The CSCX study has provided measurements which quantify the degree of current sheet canting under a variety of experimental conditions. Further analysis of the data lead to the conclusion that current sheet canting appears to be a natural consequence of the manner in which current is conducted in pulsed electromagnetic accelerators. It is proposed that depletion of plasma along the anode can lead to a sequence of events that result in a canted current sheet. In the subsections which follow, we summarize our major findings, suggest future experiments to address deficiencies in the study, and finally make suggestions for how the insight gained can be practically implemented to improve the performance of pulsed plasma thrusters.

1.16.1 Summary of findings

The major experimental findings and theoretical conclusions reached in the CSCX study were:

- Current sheet canting was observed in all propellants and pressure levels tested.
- The canting angle was found to depend on the atomic mass of the propellant; lighter atoms were observed to yield less canting (the measured angles ranged from approximately 10° for hydrogen to 70° for xenon). Molecular propellants which contain hydrogen (hydrogen, deuterium, and methane were tested) showed a pronounced reduction in canting at the highest pressure levels.
- Calculations (which make use of measured CSCX current sheet thermodynamic properties) reveal that the diamagnetic drift induced fluid motion may be appreciable in the CSCX accelerator. It is proposed that diamagnetic drift may contribute to plasma depletion in the anode region.

- It is proposed that Hall effect-enhanced penetration of the magnetic field through the tenuous anode plasma causes the current sheet to bifurcate and, ultimately form a canted current sheet.
- A simple model which includes the Hall effect (based on theoretical results from Fruchtman[34]) yields qualitative agreement with the measured dependence of canting angle versus propellant atomic mass.
- Current sheet canting may negatively impact the ability of current sheets to sweep up propellant. A rough calculation that made use of the measured electron density of a helium current sheet indicated that only about 10% of the propellant was entrained within the sheet.
- It is proposed that the life of a current sheet has three main phases:
 1. **Initiation phase** – thinning of the current sheet near the anode, possibly due to diamagnetic drift, causes anode starvation and allows the magnetic field (through Hall effect-enhanced field transport) to rapidly propagate along the anode, faster than the rest of the current sheet.
 2. **Branching phase** – a canted current front (branch) emerges from the top of the initiation trunk; the branch-trunk interface recedes down the trunk at the Alfvén speed (v_A), while the branch-anode interface propagates ahead at the (faster) Hall-convective speed (v_C), until the branch contacts the cathode.
 3. **Snowplow phase** – After the transient branching phase, a single, canted, planar current sheet propagates at a fairly constant angle (θ), pushing plasma with an axial speed approximately equal to $v_A / \cos \theta$. The $\mathbf{J} \times \mathbf{B}$ force density pumps propellant preferentially toward the cathode where it may stagnate and accumulate, and ultimately get left behind the propagating current sheet.

1.16.2 Directions for Future Work

The present study made detailed measurements to quantify the degree of current sheet canting under a variety of experimental conditions; however, some questions still remain. The following course of action is proposed to build upon the experimental work presented here and to prove some of the theoretical assertions made in the previous section.

Since the onset of canting has been proposed to occur at the breech, detailed mapping of the current, magnetic field, and electron density in that region should be revealing. Ideally, a 2-d interferometric imaging system, in conjunction with an array of magnetic field probes, would be used to obtain a highly resolved set of data for the evolution of the current sheet plasma and magnetic fields, near the breech of the accelerator.

Since current sheet canting appears to negatively affect the current sheet's ability to entrain propellant, a study which makes an accurate accounting of the

total amount of propellant contained in the current sheet, as well as quantifying the amount of leakage, would be beneficial. The desired measurement could be accomplished using an interferometer aligned in configuration 2 (see Fig. 1.11) but with perhaps four or more beams, to determine the spatial distribution of electron density in the current sheet. The device could be positioned at several different axial locations to gain an understanding of the rate at which plasma “leaks” from the current sheet near the cathode. The use of pressure probes could also provide valuable data in mapping the distribution of the propellant both before and after the current sheet has passed.

A performance related experiment should be conducted in order to determine if current sheet canting actually impacts the performance of a pulsed plasma thruster. A simple experiment would involve measuring the impulse bit of a coaxial gas-fed pulsed plasma thruster operated in both positive and negative polarities.

Chapter 2

Current Sheet Photo-Initiation

1

2.1 Introduction

The idea of using photons to initiate pulsed plasma thruster (PPT) discharges was introduced by Berkery and Choueiri.[38] The motivation is to explore a possible replacement for spark plugs as a method of discharge initiation. Spark plugs have high erosion rates which limit their lifetime[39] and produce azimuthally non-uniform current sheets which hinder thruster efficiency.[40]

The original idea involved using an ultraviolet laser pulse to create a pulse of electrons from the backplate of a PPT through the photoelectric effect. That electron pulse would alter the space charge characteristics of the discharge gap, thus lowering the breakdown voltage. If the discharge gap was initially placed at an undervoltage, a voltage slightly less than that required for breakdown without the electron pulse, and that undervoltage was greater than the breakdown voltage necessary with the electron pulse, then the electron pulse would have successfully initiated the discharge.

Berkery and Choueiri attempted to achieve a breakdown by shining ultraviolet laser pulses on a magnesium backplate fixed to the cathode of an undervoltaged GFPPT in an argon atmosphere, but they failed to initiate a discharge in this manner due to difficulties in properly conditioning the surface . They were, however, able to achieve a breakdown with a laser operating at an infrared wavelength. Since infrared photons do not possess enough energy to photoelectrically remove electrons from a magnesium surface, the mechanism behind this discharge was unclear.

The goal of the research described in this chapter of the report was to identify

¹The study in this section was conducted by J. Cooley and E. Choueiri

the mechanism by which infrared laser pulses were able to induce breakdowns and explore its dependencies with the ultimate practical goal of determining whether or not this mechanism would be a viable method of thruster discharge initiation.

We considered several possible candidates for the breakdown mechanism. It was thought that an infrared laser pulse may heat the surface to the point that significant thermionic emission of electrons might occur. This electron pulse then might be enough to achieve a breakdown in the same manner as the photoelectric pulse initially considered. We also considered the possibility that each laser pulse might vaporize a small portion of the backplate material. The resulting magnesium vapor would be easier to ionize than the background argon and thus the breakdown would be achieved at the undervoltage. Similarly, we hypothesized that the heat from the laser pulse might release water vapor or other gases that had been absorbed into the bulk of the backplate.

We begin by describing the setup, methodology, and results of a series of experiments designed to illuminate the discharge mechanism. We then present a theoretical investigation of the interaction of the laser pulse with the backplate surface. It includes calculations of threshold energies below which thermionic emission and vaporization will not occur. In addition, we devise a functional relationship between the laser pulse energy and the flux of outgassed materials with the goal of explaining our experimental results. Finally, we present our conclusions on how the infrared-induced discharge works and how one might use this information to design a new initiation system for PPTs.

2.2 Experimental Setup

Experiments were carried out in a bell jar vacuum facility outfitted with a mechanical pump, diffusion pump, and refrigerated baffles. The facility is capable of reaching pressures as low as 2×10^{-4} Torr.

We used a Continuum Nd:YAG laser with fundamental of 1064nm in the infrared. The spot size of the laser is 1 cm and pulses with energies varying from 10 mJ to 500 mJ were used. The laser's flashlamps were pulsed at 10 Hz and the Q-switched laser pulse width was 8ns.

The pulsed plasma thruster used in these experiments is called PT4 and was developed in collaboration with Science Research Labs[41]. It has a coaxial geometry with the center electrode acting as the cathode and the outer electrode as the anode (Figure 2.1). The magnesium backplate is fixed to the cathode and held at cathode potential. We did not use the thruster's gas feed system or capacitor bank in any experiments; the thruster was strictly employed as a discharge gap with the appropriate geometry. This thruster was outfitted with a ceramic disc heater. Originally intended as part of a photocathode cleaning procedure, this heater was used as part of the control of the experiment described in Section 2.3.1.

Diagnostics included a UTI 100C Precision Mass Analyzer and a Scientech 362 laser power meter.

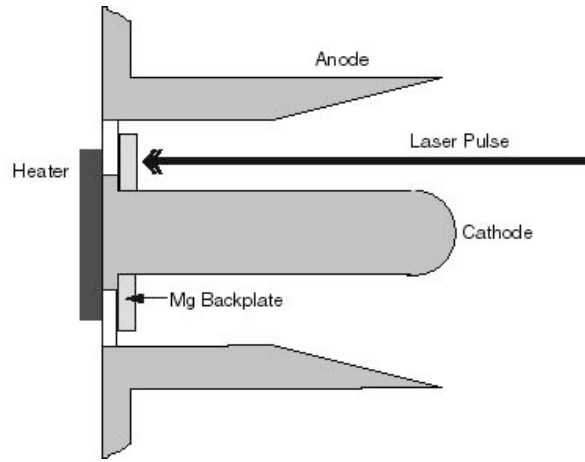


Figure 2.1: Schematic of the thruster used in experiments.

2.3 Experimental Methods and Results

Laser-induced discharges were produced in the following manner: the thruster was placed in the vacuum vessel which we then pumped down to 2×10^{-4} Torr, flushed three times with argon, and filled to the desired pressure. The voltage on the thruster was then gradually increased until a breakdown occurred. This was repeated several times and the results averaged to calculate the breakdown voltage. The voltage was then decreased to the desired undervoltage, determined in terms of a percentage of the breakdown voltage. Single laser pulses were then directed onto the backplate and pulse energy was increased until a breakdown repeatably occurred. The laser was then set into a repeating pulsed mode and the average power was measured with the laser power meter.

Initial experiments achieved breakdowns with pulse energies as low as 10 mJ for a 3% undervoltage at a pressure of 500 mTorr. Since the model we present in Sections 2.4.2 and 2.4.2 predicts no thermionic current or surface vaporization at these power levels, we proceeded with the hypothesis that the effect was attributed to surface desorption.

2.3.1 Effect of Outgassing on Laser Pulse Energy Requirement

In order to measure the effect of outgassing on the laser pulse energy required for breakdown, we performed the following experiment. The thruster was placed in the vacuum vessel which was then pumped to its minimum pressure of 2×10^{-4} Torr. The heater was then turned on to raise the backplate temperature to 150°C . The minimum laser pulse energy at which a breakdown could be repeatably achieved was then measured, and this was repeated at various times throughout the experiment. The results of that experiment are presented in

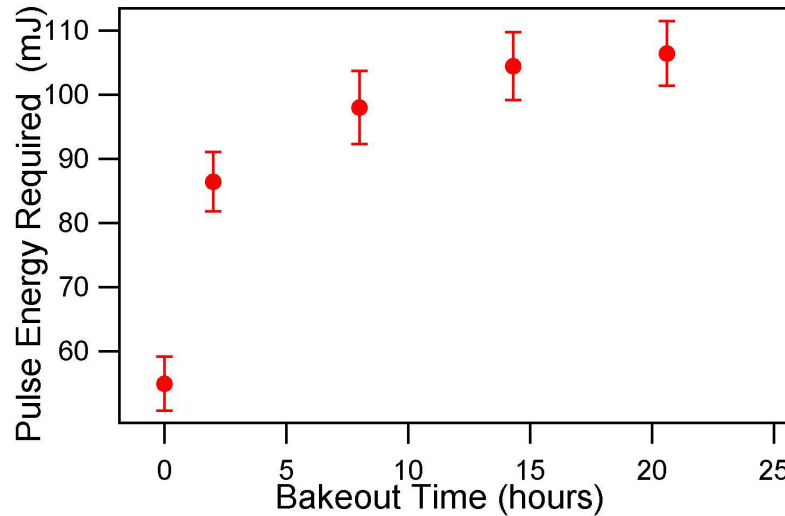


Figure 2.2: Measured minimum laser pulse energy required for breakdown as a function of bakeout time.

Figure 2.2.

2.3.2 Mass Spectrometry

In order to determine the composition of desorbed gases, we performed mass spectrometry using a residual gas analyzer (RGA). The thruster was placed in the vacuum vessel which was pumped down to its minimum pressure. Its heater was then turned on to raise the backplate temperature to approximately 150°C and the RGA was used to measure the molecular mass spectrum ranging from 1 to 100 amu. The bakeout period lasted approximately 6 hours. Figure 2.3 shows the relative heights of mass peaks that have been attributed to various species as a function of bakeout time. Each peak height is normalized to the height of the peak associated with diatomic nitrogen to give a relative partial pressure. Included species are water, diatomic oxygen, argon, and several hydrocarbons that are commonly found dissociative products of diffusion pump oil, mechanical pump oil, or vacuum grease, all of which are employed in the vacuum facility. All species presented were chosen because they exhibited interesting behavior and no significantly relevant peaks were left out.

Most of the species that outgassed did so completely within the first hour of baking. The notable exception is water, which dominated the outgassed mixture during the entire experiment. After approximately 90 minutes, water remained as the only species that outgassed significantly and continued to do so until the heater was turned off at approximately 6 hours.

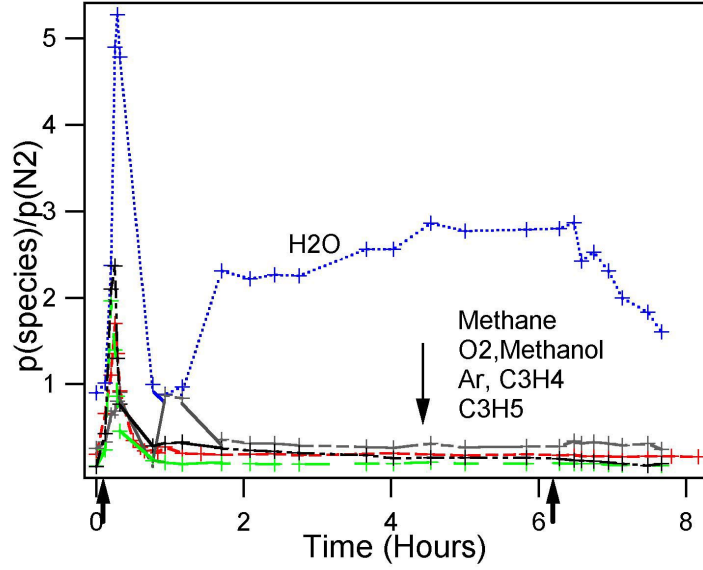


Figure 2.3: Relative partial pressures of various species as a function of bakeout time. The arrows indicate when the heater was switched on and off.

2.4 Theory

2.4.1 Discharge Initiation Mechanisms

The current in gas-filled region between biased electrodes is given by [42]

$$i = \frac{i_0 e^{\alpha d}}{1 - \gamma(e^{\alpha d} - 1)}, \quad (2.1)$$

where α , called the Townsend ionization coefficient, is the number of ionizing collisions per unit length, d the width of the gap and γ the secondary electron emission coefficient from the cathode. The initial current, i_0 , could be a photoelectric current from the walls or might be the result of cosmic rays or other ionizing phenomena. If we define a breakdown parameter,

$$\mu = \gamma[\exp(\alpha d) - 1], \quad (2.2)$$

we see that as $\mu \rightarrow 1$, the discharge current becomes infinite. This is the Townsend breakdown criterion and marks the point at which the creation of electrons by ionization and secondary emission becomes self-sustaining. We hope to manipulate the breakdown by changing the initial current, which does not appear explicitly in the breakdown criterion. However, Berkery and Choueiri[38] describe a numerical model[38] that shows that a pulse of electrons introduced into an undervolted discharge gap will introduce a space charge in the gap and change the likelihood of ionization. Thus the initial current dependence

	A [1/cmTorr]	B [V/cmTorr]	ε_I [eV]
A	12	180	15.8
H ₂ O	13	290	12.6[44]
Mg	-	-	7.65[22]

Table 2.1: Townsend ionization constants for argon and water and first ionization energies for argon, water and magnesium. All values are from von Engel [45] except where noted.

is implicit in the Townsend ionization coefficient α . While this model was intended to treat pulses of electrons released photoelectrically, it does not specify any requirements on the source of the electron pulses. It is therefore clear that current emitted thermionically should be able to initiate a breakdown. We will also see, however, that all of the discharge mechanisms under consideration involve introducing electron pulses in some way. Thus, Berkery's and Choueiri's model remains appropriate.

The proposed mechanism by which released gases, be they magnesium vapor or desorbed gases, might initiate a breakdown relies on a requirement that the released gases are more likely ionized than the argon background. Free electrons in the undervoltaged gap are always accelerated by the applied field, but they do not reach the energy required to sustain an amplifying avalanche. When a new gas with a higher α is introduced, however, ionization becomes more likely and the avalanche can propagate among that species. This "mini-avalanche" performs the same function as the electron current pulse considered in the model.

The Townsend ionization coefficient, α , is a function of pressure and electric field as given by [43]

$$\alpha = Ape^{-Bp/E}. \quad (2.3)$$

The constants A and B are determined by the gas and are presented in Table 2.1 for argon and water. Raising the ionization constants will lower the breakdown voltage. Constants A and B are not known for magnesium vapor, but the first ionization energy is presented along with those for argon and water. Based on the ionization energy, it seems likely that magnesium vapor would ionize more frequently than argon. As a result, we expect that the introduction of water into an appropriately undervoltaged argon discharge gap should initiate a breakdown, and it seems reasonable to suggest that the introduction of magnesium would do the same.

2.4.2 Effects of Laser Radiation on the Surface

The laser used for this experiment was a Q-switched Nd:Yag laser operating at 1064 nm with a pulse width of 8 ns. The spot size of the laser is 1 cm and pulses with energies varying from 10 mJ to 500 mJ were used.

Because of their short duration, Q-switched laser pulses have a high irradiance, or power per unit area, but do not heat the surface as effectively as a

longer pulse with a lower irradiance.

Temperature Distribution

We begin by calculating the temperature in the metal as a function of depth during the laser pulse. We assume that the heat flow is one dimensional, which is will later be justified on the basis that the dimension of heat penetration is much smaller than the width of the beam. We also assume that the pulse energy is fully absorbed into the metal.

The differential equation for heat flow in a semi-infinite rod with a heat addition function $A(x, t)$ is[46]

$$\frac{\partial^2}{\partial x^2}T(x, t) - \frac{1}{\kappa} \frac{\partial}{\partial t}T(x, t) = -\frac{A(x, t)}{K}, \quad (2.4)$$

where T is the temperature, κ the thermal diffusivity, and K the thermal conductivity. If the surface is at $x = 0$, the initial and boundary conditions are

$$\begin{aligned} T(x, 0) &= 0 \\ T(\infty, t) &= 0 \end{aligned} \quad (2.5)$$

We write our heating function as:

$$A(x, t) = F(t)(1/\delta)e^{-x/\delta}, \quad (2.6)$$

where $F(t)$ is the absorbed laser irradiance in W/cm^2 and δ the skin depth of the metal.

Equation (2.4) is solved using Duhamel's principle, which involves finding the solution for which the temporal pulse shape is a flat step function at $t = 0$. For metals, which have high optical absorption, we get a solution:[46]

$$T(x, t) = \frac{\kappa^{1/2}}{K\pi^{1/2}} \int_0^t \frac{F(t - \tau) \exp(-x^2/4\kappa\tau)}{\tau^{1/2}} d\tau. \quad (2.7)$$

We assume that the laser pulse has the shape:

$$F(t) = I_{\text{peak}} \left(\frac{t}{T_{\text{width}}} \right)^2 \exp \left(-\frac{2t}{T_{\text{width}}} \right). \quad (2.8)$$

Using this laser pulse shape, we numerically integrate Equation (2.7) to find the temperature distribution in the magnesium surface. Figure 2.4 is a plot of temperature versus depth with time as a parameter for an 8 ns pulse of energy 170 mJ.

Note that no significant heating occurs beyond 10^{-3} cm. Since the laser spot size is 1 cm, our assumption of one-dimensionality is valid.

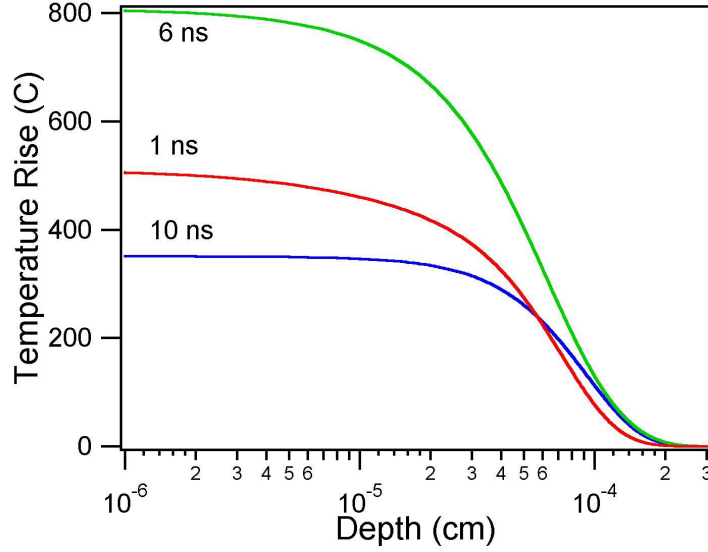


Figure 2.4: Temperature distribution in the metal at various times for a laser pulse with $T_{width} = 8ns$ and a pulse energy of 170 mJ.

Thermionic Electron Emission

Thermionic electron current density is a function of surface temperature as given by Richardson's equation [47]:

$$j = AT^2 \exp(-\phi/kT), \quad (2.9)$$

where j is the current density in A/cm^2 , ϕ is the work function of the metal, and A is a constant equal to $60.2A/(cm^2C^2)$. Magnesium has an electron work function of 3.7 eV.

From this calculation and equation (2.9) we calculate the maximum thermionic electron current as a function of laser pulse energy; these results are presented in Figure 2.5.

From Figure 2.5 we see that there is essentially no thermionic electron emission until the pulse energy gets above 300 mJ.

Vaporization

Figure 2.6 is a plot of maximum surface temperature rise versus pulse energy. The boiling point of magnesium is $1100^\circ C$. We can see from this plot that the magnesium surface does not pass the boiling point for pulse energies below 250 mJ.

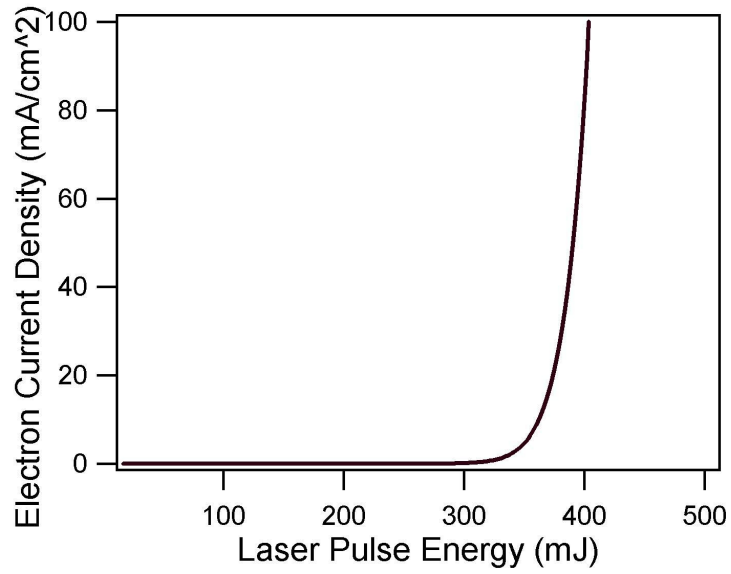


Figure 2.5: Maximum electron current density as a function of laser pulse energy.

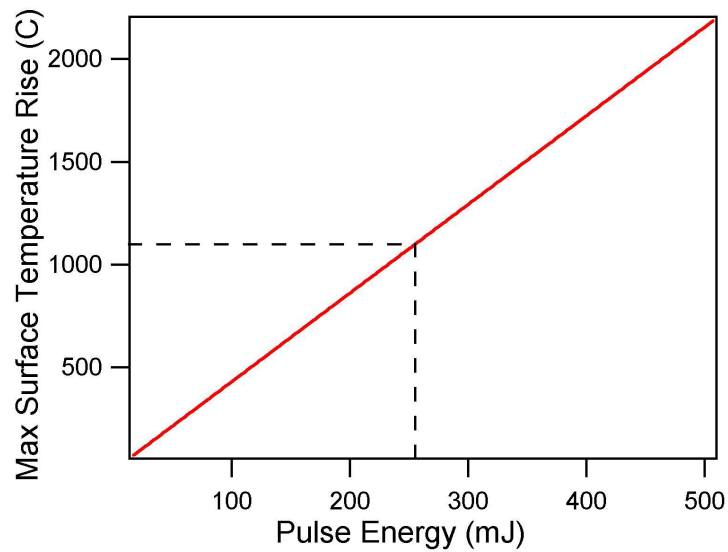


Figure 2.6: Maximum surface temperature as a function of pulse energy. The dotted line represents the boiling point of magnesium.

Desorption

As the laser heats the backplate surface, gas molecules trapped in adsorption sites on the surface will be released. We will begin by deriving a relationship between laser pulse energy and flux of desorbed gas with the surface concentration of that gas as a parameter. We will then use diffusion theory to understand how the surface concentration will change over a long outgassing period. This theoretical analysis is presented as an effort to assemble a model that describes the results of the outgassing experiment we describe in Section 2.3.1.

We assume that the desorption process is simple molecular desorption of the type described by the first order reaction:



Desorption of water from the magnesium surface is an example of this reaction. The rate of desorption is then described by [48]

$$R = -\frac{dN}{dt} = kN, \quad (2.11)$$

where N is the surface concentration of the adsorbed species and k is the reaction rate constant given by [48]

$$k = ne^{-\varepsilon_{\text{des}}/RT}. \quad (2.12)$$

Here ε_{des} is the activation energy for desorption and n is the “attempt frequency” of overcoming the desorption barrier. This can be taken as the frequency of vibration between the molecule and the substrate; each stretching of the bond can be considered an attempt at overcoming the potential barrier. This frequency is usually on the order of 10^{13} s^{-1} . [48] The activation energy for desorption for water in MgO is 55 kJ/mol [49].

Combining Equations (2.11) and (2.12) gives the desorption flux as a function of temperature and surface concentration:

$$\Gamma_{\text{des}} = nNe^{-\varepsilon_{\text{des}}/RT}. \quad (2.13)$$

We now wish to find the surface concentration as a function of time during a long outgassing period. We assume that the metal initially contains a uniformly distributed concentration of gas C_0 which we leave as a free parameter. We also continue to treat the problem as a semi-infinite solid in one dimension. The process by which gas reaches the surface is diffusion, which is described by Fick’s law [50]

$$\frac{\partial}{\partial x} \left(D \frac{\partial C}{\partial x} \right) = \frac{\partial C}{\partial t}. \quad (2.14)$$

C is the concentration in molecules/cm³ and D is the diffusion constant. If x is the depth coordinate and we set the surface at $x = 0$, we can solve this equation to get the concentration as a function of depth and time.

$$C(x, t) = C_0 \text{erf}[x/2(Dt)^{1/2}]. \quad (2.15)$$

We also note that the flux of molecules to the surface as a function of time is given by

$$\Gamma(t) = D \left(\frac{\partial C(x, t)}{\partial x} \right)_{x=0}, \quad (2.16)$$

where Γ is in molecules/s cm⁻². Using Equation (2.15), we get the diffusive flux to the surface as a function of time:

$$\Gamma(t) = C_0 \left(\frac{D}{\pi t} \right)^{1/2}. \quad (2.17)$$

The surface concentration will be determined by a balance between diffusive flux to the surface and desorptive flux from the surface:

$$\left(\frac{dN}{dt} \right)_{\text{net}} = \left(\frac{dN}{dt} \right)_{\text{diffusive}} - \left(\frac{dN}{dt} \right)_{\text{desorptive}}. \quad (2.18)$$

There are three relevant timescales in our problem. It is assumed that the time in which the laser removes the desorptive flux from the surface is much faster than the timescale on which a steady-state surface concentration is reached. That timescale is then assumed to be much faster than the time scale on which the diffusive flux changes. Thus, during the time it takes to reach a steady-state surface concentration, the magnitude of the diffusive flux doesn't change. We therefore treat the value of diffusive flux as constant after a given period of outgassing. Combining Equations (2.13), (2.17), and (2.18) gives a differential equation of the form

$$\frac{dN}{dt} = \alpha - \beta N. \quad (2.19)$$

The substitutions $\alpha = C_0(D/\pi t)^{1/2}$ and $\beta = ne^{-\varepsilon_{\text{des}}/RT}$ have been employed. This gives a solution:

$$N(t) = \alpha/\beta + N_0 e^{-\beta t}, \quad (2.20)$$

which gives the steady state surface concentration as:

$$N(t_{\text{og}}) = \alpha/\beta = \frac{C_0(D/\pi t)^{1/2}}{ne^{-\varepsilon_{\text{des}}/RT_{ss}}}. \quad (2.21)$$

T_{ss} is the steady-state bulk temperature of the metal and t_{og} is the total outgassing time. We can now calculate the normalized surface concentration as a function of outgassing time. We assume that the diffusion constant will be on the order of 10⁻⁷cm²/s and use a temperature of 150°C as in the experiment. This calculation is presented in Figure 2.7.

Our timescale assumptions tell us that the steady-state bulk temperature doesn't change on the timescale of the laser pulse. By combining Equations (2.13) and (2.7) we get the desorbed flux as a function of temperature associated with the laser pulse and outgassing time:

$$\Gamma = C_0 \left(\frac{D}{\pi t} \right)^{1/2} \exp \left[-\frac{\varepsilon_{\text{des}}}{R} (T_{\text{laser}}^{-1} - T_{ss}^{-1}) \right]. \quad (2.22)$$

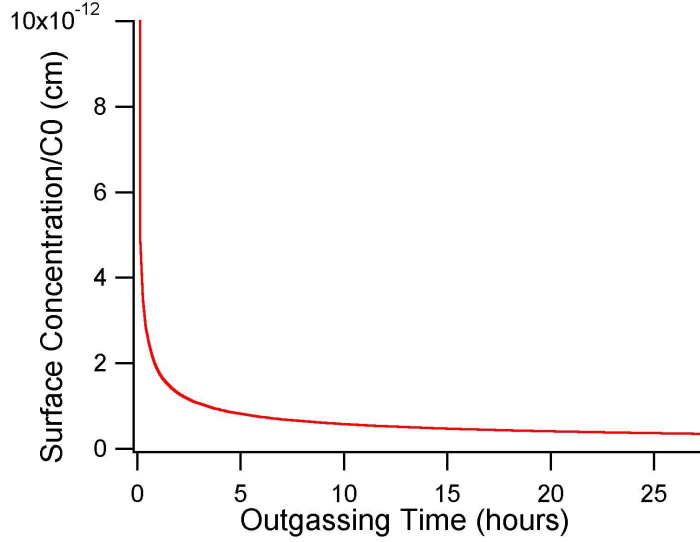


Figure 2.7: Surface Concentration / C_0 as a function of outgassing time for a bakeout temperature of 150°C .

It is our assertion that in order to initiate a discharge, the laser pulse must induce some critical flux Γ^* of desorbed material. As the thruster is allowed to outgas for a long time, the surface concentration of absorbed gas decreases, and a laser pulse must become more energetic to attain that same critical flux level. From Equation (2.22) we calculate that the temperature rise necessary to achieve a given Γ^*/C_0 varies in time according to:

$$T_{laser} = \left\{ -\frac{R}{\varepsilon_{des}} \log \left[\frac{\Gamma^*/C_0}{\left(\frac{D}{\pi t}\right)^{1/2}} \right] + \frac{1}{T_{ss}} \right\}^{-1}. \quad (2.23)$$

The required laser pulse energy to achieve a Γ^*/C_0 chosen as 10^{-6} cm/s is plotted in Figure 2.8. Data from the experiment described in Section 2.3.1 is superimposed to show functional agreement.

2.5 Discussion

The results of our theoretical analysis indicate that laser-induced desorption is the most likely mechanism behind the observed discharges. In terms of functional form and timescale, the results of the outgassing experiment agree fairly well with theoretical predictions. This fact further strengthens the argument that desorption is the relevant mechanism. Based on the RGA experiment, we concluded that the gas desorbed by the laser pulse is water. As a result, we have concluded that the infrared-induced breakdowns are likely caused by desorption of water into the discharge gap.

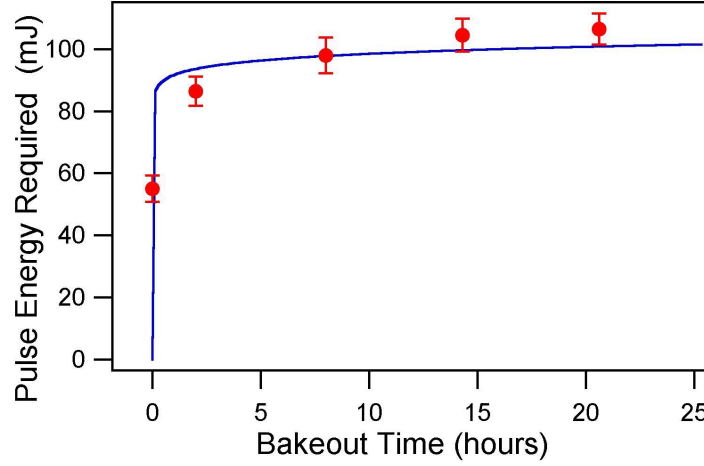


Figure 2.8: Required laser pulse energy to achieve a Γ^*/C_0 of 10^{-6} cm/s as a function of outgassing time for a bakeout temperature of 150°C . The experimental data from Section 2.3.1 is also plotted.

More conclusions on photo-initiation and insights on how it relates to the design of a better thruster are given at the end of the next chapter.

2.6 Conclusions

We have observed the phenomenon of IR-assisted breakdown in an undervoltaged PPT discharge gap and investigated three candidate mechanisms: thermionic emission, surface vaporization, and desorption.

- We have theoretically predicted that neither thermionic emission nor surface vaporization should occur at the pulse energies for which breakdowns were observed.
- We have determined through experiment and theory that desorption of water is the most likely cause of the IR-assisted PPT discharges observed thus far.
- We have also concluded that it is theoretically feasible to construct a practical discharge initiator that works on the principle of thermionic emission (see the end of the following chapter).

Chapter 3

How to build a Better Thruster

It is fitting to conclude this study by returning to the primary role of the work, as stated in the Introduction of Chapter 1 – to provide insight on how to build better electromagnetic pulsed plasma thrusters.

3.1 Insight from the current sheet canting study

The data collected in this study show that the most direct way to inhibit current sheet canting is to use low atomic mass propellants at high pressure. In this study hydrogen, deuterium, and methane showed markedly lower canting at higher pressures. However, hydrogen is not an ideal PPT propellant, due to the difficulty of handling cryogenic propellants on a spacecraft. To practically exploit the benefits of low current sheet canting which results from the use of hydrogen at high pressure, we sought alternative propellants which contain a significant amount of hydrogen in their molecular structure. Alkanes, with their $C_N H_{2N+2}$ structure, seemed like a natural choice. Methane was tested as part of the interferometric study and was found to have the same reduced canting behavior (at higher pressures) as hydrogen. Further tests are needed on longer-chain hydrocarbons. If butane, for example, is found to exhibit similar behavior, it will be an appealing GFPPT propellant on two levels. In addition to the aforementioned canting benefits, butane can be stored as a liquid under relatively low pressure, at room temperature; therefore, a butane propellant system will have a much smaller specific volume (smaller fuel tank and feed system) than a high pressure gas system.

Thruster designs should also strive to prevent diamagnetic drift-induced anode starvation. The most obvious way to accomplish this would be to somehow load the propellant preferentially along the anode. This might be accomplished by having an array of propellant injectors distributed axially along the anode, rather than the typical back-plate injection scheme. Alternatively, a segmented

electrode (anode), such as the one used in Lovberg's study, could be used. Gas could be injected into a shroud that encloses the electrodes, approximating the ambient fill technique used in Lovberg's device.

In coaxial accelerators a simple design rule can immediately be stated: the outer electrode should always be the anode. In the coaxial geometry, the $1/r^2$ variation in magnetic pressure predisposes the current sheet to run faster along the inner electrode; by making the inner electrode the anode, this undesirable situation would only be amplified because of the natural tendency of the current sheet to move faster along the anode. But, if the outer electrode is made to be the anode, some antagonism between the two effects might be established wherein the non-uniform magnetic pressure effect could be counteracted by the tendency of the current sheet to move faster along the anode – leading to a non-canted current sheet. The current measurements of Keck clearly display this type of behavior.

3.2 Insight from the photo-initiation study

As can be concluded from the study presented in Chapter 2, the amount of water absorbed in the backplate is not likely to be large enough to sustain significant surface concentrations for the entire lifetime of a thruster. Consequently, we do not believe that the current method of obtaining discharges (initiation through IR-induced desorption) is a viable technique for propulsion applications. However, it may still be possible to utilize the phenomenon of desorption to initiate GFPPT discharges. A feed system could be designed that supplies a small amount of some easily ionizable fluid to a surface in the discharge gap. This fluid could then be flash heated, either optically or with a short, high-power electrical pulse to a resistive heater, and the resulting desorption would trigger a discharge.

Thermionic emission is another alternative for controlled discharge initiation and our model suggests that it should be more practical.

Magnesium's temperature threshold for thermionic emission is higher than its boiling point as indicated in Figure 3.1. It is therefore not possible to extract significant thermionic currents from a magnesium surface without damaging that surface. Thermionic emission from magnesium would thus not be a viable initiation mechanism for propulsion. However, the same is not true for all materials. For example if the backplate were made out of tungsten, which has a much higher melting point than magnesium but comparable work function, it should be possible to extract significant amounts of thermionic current without damaging the surface. In addition, tungsten has a lower thermal conductivity than magnesium and thus requires less laser energy to achieve the same temperature.

In Figure 3.2 we plot the maximum surface temperature and thermionic electron emission in a tungsten surface versus laser pulse energy. The dashed lines indicate the melting point of tungsten. Thus, it is quite reasonable to consider a tungsten thermionic discharge initiator that would work in a fashion very

similar to the current setup. This is presently being explored at our laboratory.

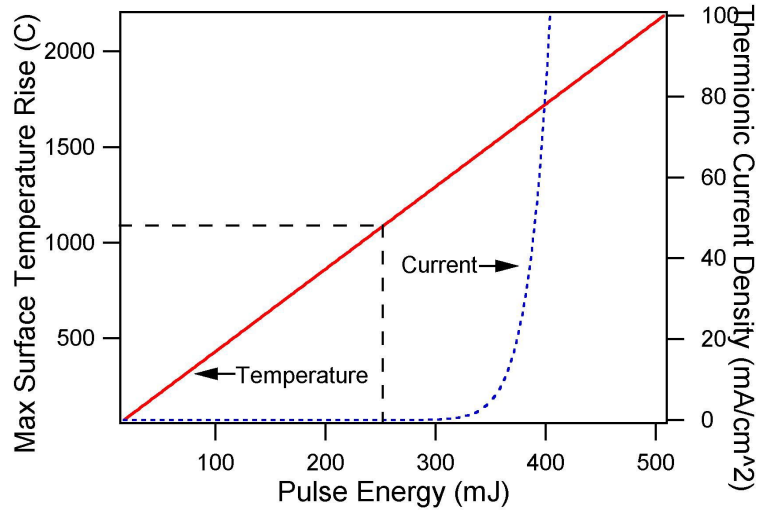


Figure 3.1: Maximum surface temperature and thermionic electron emission as a function of laser pulse energy for a magnesium surface. The dashed line represents the boiling point of magnesium.

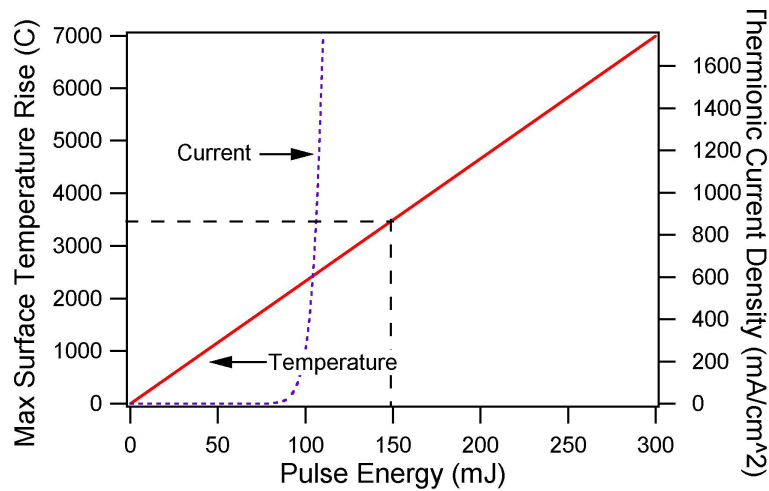


Figure 3.2: Maximum surface temperature and thermionic electron emission as a function of laser pulse energy for a tungsten surface. The dashed line represents the melting point of tungsten.

Bibliography

- [1] T. E. Markusic. *Current Sheet Canting in Pulsed Electromagnetic Accelerators*. PhD thesis, Princeton University, Princeton, NJ, 2002.
- [2] J. Marshal. Performance of a hydromagnetic plasma gun. *The Physics of Fluids*, 3(1):134–135, January-February 1960.
- [3] R.G. Jahn. *Physics of Electric Propulsion*. McGraw-Hill Book Company, 1968.
- [4] D.R. Keefer and B. Rhodes. Electromagnetic acceleration in pulsed plasma thrusters. In *25th International Electric Propulsion Conference*, Cleveland, OH, August 1997. IEPC 97-035.
- [5] K.A. Polzin, E.Y. Choueiri, P. Gurfil, and N.J. Kasdin. Multiple plasma propulsion options for multiple terrestrial planet finder architectures. *Submitted for publication: Journal of Spacecraft and Rockets*, 2002.
- [6] R.G. Jahn K.E. Clark. Quasi-steady plasma acceleration. In *AIAA 7th Electric Propulsion Conference*, Williamsburg, Virginia, March 3-5 1969. AIAA 69-267.
- [7] P.J. Turchi and R.L. Burton. Pulsed plasma thruster. *J. Propulsion and Power*, 14(5):716–735, Sept.-Oct. 1998.
- [8] J.K. Ziemer, E.A. Cubbin, E.Y. Choueiri, and D. Bix. Performance characterization of a high efficiency gas-fed pulsed plasma thruster. In *33rd Joint Propulsion Conference*, Seattle, Washington, July 6-9 1997. AIAA 97-2925.
- [9] J.K. Ziemer, E.Y. Choueiri, and D. Bix. Is the gas-fed ppt an electromagnetic accelerator? an investigation using measured performance. In *35th AIAA Joint Propulsion Conference*, Los Angeles, CA, June 20-23 1999. AIAA-99-2289.
- [10] J.K. Ziemer and E.Y. Choueiri. Scaling laws for electromagnetic pulsed plasma thrusters. *Plasma Sources Science and Technology*, 10(3):395–405, August 2001.

- [11] J.K. Ziemer. A review of gas-fed pulsed plasma thruster research over the last half-century. EPPDyL internal report, Princeton University, 2000.
- [12] T.E. Markusic and E.Y. Choueiri. Visualization of current sheet canting in a pulsed plasma accelerator. In *26th International Electric Propulsion Conference*, Kitakyushu, Japan, October 17-21 1999. IEPC 99-206.
- [13] A.C. Eckbreth. *Current Pattern and Gas Flow Stabilization in Pulsed Plasma Accelerators*. PhD thesis, Princeton University, 1968.
- [14] R.J. Vondra and K.I. Thomassen. Flight qualified pulsed electric thruster for satellite control. *Journal of Spacecraft and Rockets*, 11(9):613–617, September 1974.
- [15] R.G. Jahn and K.E. Clark. A large dielectric vacuum facility. *AIAA Journal*, 1966.
- [16] L.C. Burkhardt and R.H. Lovberg. Current sheet in a coaxial plasma gun. *The Physics of Fluids*, 5(3):341–347, March 1962.
- [17] R.H. Lovberg. The measurement of plasma density in a rail accelerator by means of schlieren photography. *IEEE Transactions on Nuclear Science*, pages 187–198, January 1964.
- [18] J.R. MacLelland, A.S.V. MacKenzie, and J. Irving. Schlieren photography of rail-tube plasmas. *Research Notes*, pages 1613–1615, April 1966.
- [19] H.W. Liepmann and A. Roshko. *Elements of Gasdynamics*. John Wiley and Sons, Inc., 1967.
- [20] W.A. Hoskins. Asymmetric discharge patterns in the mpd thruster. Master's thesis, Princeton University, 1990.
- [21] G. Spanjers. Propellant inefficiencies in pulsed plasma thrusters. In *6th Aerospace Sciences Meeting*, New York, New York, January 22-24 1998. AIAA 68-85.
- [22] D.R. Lide. *CRC Handbook of Chemistry and Physics, 77th Edition*. CRC Press, 1997.
- [23] H.R. Griem. *Principles of Plasma Spectroscopy*. Cambridge University Press, 1997.
- [24] 2002. Personal correspondence with Prof. Dennis Keefer.
- [25] J.D. Huba. *NRL Plasma Formulary*. Naval Research Laboratory, 1994.
- [26] M. Rosenbluth. Infinite conductivity theory of the pinch. In C.L. Longmire, J.L. Tuck, and W.B. Thompson, editors, *Plasma Physics and Thermonuclear Research*, page 217. Pergamon, 1963.

- [27] R.H. Lovberg. Investigation of current-sheet microstructure. *AIAA Journal*, 4(7), 1966.
- [28] F.F. Chen. *Plasma physics and controlled fusion*. Plenum Press, 1984.
- [29] I. Kohlberg and W.O. Coburn. A solution for the three dimensional rail gun current distribution and electromagnetic fields of a rail launcher. *IEEE Transactions on Magnetics*, 31(1), 1995.
- [30] K.D. Diamant. *The anode fall in a high power pulsed MPD thruster*. PhD thesis, Princeton University, 1996.
- [31] L. Spitzer. *Physics of fully ionized gases*. Interscience Publishers, 1962.
- [32] L.C. Woods. *Principles of Magnetoplasma Dynamics*. Oxford University Press, 1987.
- [33] A. Fruchtman. Penetration and expulsion of magnetic fields in plasmas due to the hall field. *Phys. Fluids B*, 3(8), 1991.
- [34] A. Fruchtman. The snowplow in plasmas of nonuniform density. *Phys. Fluids B*, 4(4), 1992.
- [35] A. Fruchtman and K. Gomberoff. Magnetic field penetration due to the hall field in (almost) collisionless plasmas. *Phys. Fluids B*, 5(7), 1993.
- [36] N.A. Krall and A.W. Trivelpiece. *Principles of Plasma Physics*. San Francisco Press, 1986.
- [37] R.B. Johansson. Current sheet tilt in a radial magnetic shock tube. *The Physics of Fluids*, 8(5):866–871, 1964.
- [38] J.W. Berkery and E.Y. Choueiri. “Laser discharge initiation for gas-fed pulsed plasma thrusters”. In *37th Joint Propulsion Conference*, Salt Lake City, UT, 2001. AIAA-2001-3897.
- [39] J. Blandino, D. Birx, J.K. Ziemer, and E.Y. Choueiri. “Performance and erosion measurements of the PT8 gas-fed pulsed plasma thruster”. Technical Report EPPDyL-JPL99b,, NASA Jet Propulsion Laboratory,, August 1999.
- [40] J.K. Ziemer. *Scaling Laws in Gas-fed Pulsed Plasma Thrusters*. PhD thesis, Princeton University, 2000.
- [41] J.K. Ziemer, E.A. Cubbin, and E.Y. Choueiri. “Performance characterization of a high efficiency gas-fed pulsed plasma thruster”. In *33rd Joint Propulsion Conference*, Seattle, Washington, January 6-9, 1997. AIAA 97-2925.
- [42] Yu.P. Raizer. *Gas Discharge Physics*. Springer-Verlag, 1997.

- [43] S. Cohen. *Laboratory in Plasma Physics*. Princeton Plasma Physics Laboratory, 1996.
- [44] S.C. Brown. *Introduction to Electrical Discharges in Gases*. John Wiley & Sons, 1966.
- [45] A. von Engel. *Ionized Gases*. Oxford at the Clarendon Press, 1965.
- [46] J.F. Ready. *Effects of High-Power Laser Radiation*. Academic Press, 1971.
- [47] J. D. Cobine. *Gaseous Conductors: Theory and Engineering Applications*. Dover Publications, 1958.
- [48] Roger Nix. “An introduction to surface chemistry”. www.chem.qmw.ac.uk/surfaces/scc.
- [49] Ola Enquist and Anthony Stone. “Adsorption of water on MgO”. *Surface Science*, **437**:239–248, 1999.
- [50] Benjamin B. Dayton. Outgassing of materials. In Dorothy M. Hoffman, Bawa Singh, and III John H. Thomas, editors, “*Handbook of Vacuum Science and Technology*”. Academic Press, 1998.